Understanding the electrochemistry of highly concentrated aqueous solutions forming biphasic systems

Damien Dégoulange

To cite this version:

Damien Dégoulange. Understanding the electrochemistry of highly concentrated aqueous solutions forming biphasic systems. Material chemistry. Sorbonne Université, 2023. English. NNT : 2023SORUS757 . tel-04749870

HAL Id: tel-04749870
https://theses.hal.science/tel-04749870v1

Submitted on 23 Oct 2024

Sorbonne Université

Ecole doctorale 397 – Physique et Chimie des Matériaux

Chimie du Solide et Energie, Collège de France, UMR 8260

Understanding the electrochemistry of highly concentrated aqueous solutions forming biphasic systems

By Damien Dégoulange

Ph.D. thesis of Physics and Chemistry of Materials

Supervised by Alexis Grimaud

Presented and defended publicly on October 27th, 2023

In front of the jury:

Dr. Lydéric Bocquet	Research Director, ENS, Paris, France	Jury President
Dr. Isabelle Billard	Research Director, LEPMI, Grenoble, France	Referee
Prof. Micheál D. Scanlon	Associate Professor, UL, Limerick, Ireland	Referee
Dr. Frédéric Kanoufi	Research Director, ITODYS, Paris, France	Examiner
Prof. Hubert Girault	Emeritus Professor, EPFL, Sion, Switzerland	Examiner
Prof. Alexis Grimaud	Associate Professor, BC, Boston, United States	Ph.D. Director
Prof. Jean-Marie Tarascon	Professor, CSE, Paris, France	Invited Member

Sorbonne Université

Ecole doctorale 397 – Physique et Chimie des Matériaux

Chimie du Solide et Energie, Collège de France, UMR 8260

Étude de l'électrochimie des solutions aqueuses fortement concentrées formant des systèmes biphasiques

Par Damien Dégoulange

Thèse de doctorat de Physique et Chimie des Matériaux

Dirigée par Alexis Grimaud

Présentée et soutenue publiquement le 27 octobre 2023

Devant un jury composé de :

Dr. Lydéric Bocquet	Directeur de recherche, ENS, Paris, France	Président du jury
Dr. Isabelle Billard	Directrice de recherche, LEPMI, Grenoble, France	Rapportrice
Prof. Micheál D. Scanlon	Professeur associé, UL, Limerick, Irlande	Rapporteur
Dr. Frédéric Kanoufi	Directeur de recherche, ITODYS, Paris, France	Examinateur
Prof. Hubert Girault	Professeur émérite, EPFL, Sion, Suisse	Examinateur
Prof. Alexis Grimaud	Professeur associé, BC, Boston, Etats-Unis	Directeur de thèse
Prof. Jean-Marie Tarascon	Professeur, CSE, Paris, France	Membre invité

“On ne connaît que les choses que l’on apprivoise”

Antoine de Saint-Exupéry, Le petit Prince – Chapitre XXI

Acknowledgments

A three years Ph.D. is a journey that one does not undertake alone. First and foremost, I am truly thankful to Alexis Grimaud, who provided me with the opportunity to carry out my Ph.D. under his supervision. Over the past three years, your passion for science and dedication to students have been really impressive and inspiring! Thank you for the time spent discussing results, providing feedbacks on papers, talks, and more. I am also grateful for the opportunity to finish my Ph.D. by working with you for a few months at Boston College. I wish you all the best for this new chapter of yours in Boston.

I would like to express my gratitude to Jean-Marie Tarascon, who welcomed me to the CSE lab at College de France. The dynamism, passion and efficiency of the CSE lab along with the network of expert you have built is really impressive and I have no doubt that the outcomes of this thesis would have been very different without this environment. Moreover, you gave me your trust to freely work on a topic outside your comfort zone, I thank you for this opportunity.

I was fortunate to collaborate with many experts who, through their diverse viewpoints and scientific backgrounds, brought diversity and valuable insights to this thesis. I thank Michael Deschamps who warmly welcomed me to CEMTHI (Orléans, France), introduced me to NMR and with whom I had inspiring discussion. I am grateful to people from LKB at ENS (Paris, France), particularly Raj Pandya and Hilton B. de Aguiar, who were enthusiastic about the challenge of studying aqueous liquid-liquid interfaces with Raman imaging. Best of luck to you, Raj, for starting your own lab at Warwick University! I also thank Dhyllan A. Skiba and Betar M. Gallant at MIT (Cambridge, United States) with whom we collaborated for microcalorimetry measurements. Cédric Boissiere and Marco Faustini at LCMCP (Paris, France) are acknowledged for performing early ellipsometry trials. I thank Lihao Feng and Andrew Lonero from Boston College for their help with laser ablation. Of course, scientific exchange also took place within the CSE lab and Gwenaëlle Rousse is deeply acknowledged for her expertise in XRD and performing Rietveld refinement. I also thank Léa Droguet and John Brown for their collaboration in attempting to reproduce jellified WiSE and coatings.

Finally, Romain Dugas is deeply thanked for his help in improving the home-made OEMS setup and designing the liquid-liquid electrochemical cell.

Outside of collaborations, the CSE lab has been a great place to learn, work and then share knowledge. Thank you to the old CSE members who welcomed me first as an intern and then as a PhD student, Thomas, Nicolas, Lea, Fanny, Pierre, Biao, Jiaqiang, Paul, Florencia, Laura, Tuncay, to mention only a few of them. It was also a great pleasure to work and exchange views with Elisa, Jacques, Ronan, Ezzoubair, Parth, Zhenying and Ivette during these three years. Thank you to Jessica for her crucial help with paperwork, which is essential for the smooth operation of the lab; she saves us a lot of time and energy! Of course, a special thanks to my office mates, Benjamin and Romain with whom I had great laughs! Thank you to all the new CSE members who kept a friendly atmosphere in the lab, Florian, Simon, Elisa, John, Cedric, and others. Beyond the lab, I have truly enjoyed spending time with all of you around drinks, board games or doing sports! I also thanks the people from Boston for their warm welcome and advices on the Bostonian life and of course, Valentin, with whom I shared this enriching experience in the US.

I would like to acknowledge Isabelle Billard and Micheál Scanlon for accepting to review this thesis. I am also grateful to Frederic Kanoufi, Hubert Girault and Lydéric Bocquet for agreeing to be part of the jury.

Enfin, mes plus chaleureux remerciements vont évidemment à ma famille et mes amis qui m’ont toujours accompagné, soutenu et encouragé durant ces trois années de thèse et toutes les années précédentes. Merci !

Contents

General Introduction and Outline

General Introduction

Starting from 1850, the cheap and abundant energy provided by fossil fuels has been the driving force to reach the current industry-based society ensuring access to health, food, goods, transportation, communication and more. Unfortunately, the consequences of this fossil fuels consumption are now clearly stated by the Intergovernmental Panel on Climate Change (IPCC): the massive use of fossil fuels has increased the concentration of greenhouse gases (CO_2, CH_4, N_2O, …) in the atmosphere to abnormal levels, nowadays reaching their highest concentrations in the last million years (**Introductory Fig. 1a**).[1] These human-induced concentration increases are responsible for a global temperature rise of more than 1°C during the 1900-2019 period (**Introductory Fig. 1b**), *i.e.* responsible for climate change.[2]

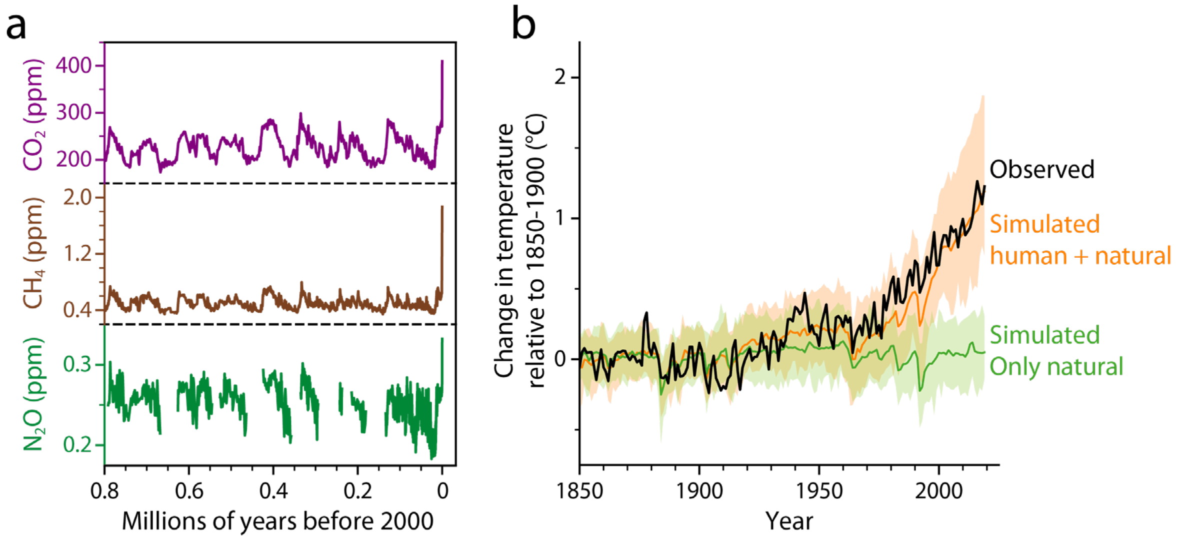

Introductory Fig. 1. Impact of the human activity on the concentration of greenhouse gases and temperature increase. a, Evolution of the concentrations of the three main greenhouse gases (top: CO_2, middle: CH_4, bottom: N_2O) from about a million year ago to now. From 1900, all three greenhouse gases show abnormal increase reaching their maximums in the last million years. Adapted from an IPCC report[1]. **b**, Changes in global surface temperature over the past 170 years (black line) relative to 1850–1900 and annually averaged compared to IPCC simulations and error bars of the temperature response to both human and natural drivers (orange) and to only natural drivers (solar and volcanic activity, green). Adapted from an IPCC report[2].

Further greenhouse gas emission and rise in temperature will lead to catastrophic climate events (hot extremes, heavy precipitation events, rise in sea level, tropical cyclones, wildfires, …) with cascading consequences (food and water insecurity, high disease risks, population displacement, …) that would result in dramatic socio-economic and security risks.[3] Thus, mitigating climate change, by moving away from a society based on the utilization of fossil fuels is one of the biggest objective of the 21st century, involving global challenges at the social, political, economic and scientific levels.

With the aim of moving away from fossil fuels, other "greener" energy sources are needed to meet the global growing energy demand. For this, renewable electricity produced via wind turbines and solar photovoltaics will ramp up in the global energy mix from 5% in 2021 up to 17% in 2030 for a net zero emission scenario by 2050 (**Introductory Fig. 2**).[4]

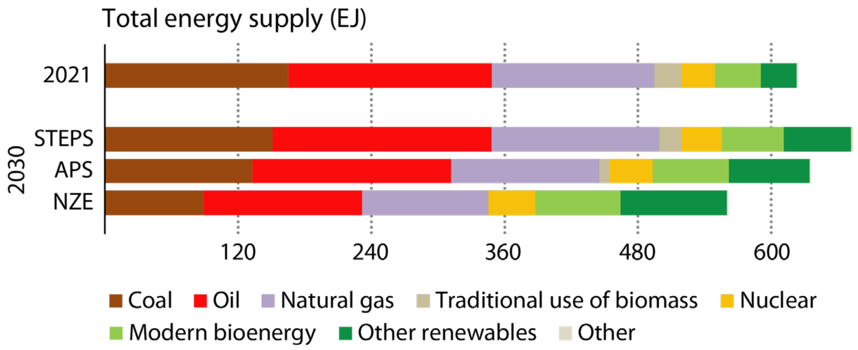

Introductory Fig. 2. Comparison of the global energy supply by fuel between 2021 and 2030 with different scenario. Three scenario are presented for 2030. The stated policies scenario (STEPS) shows the trajectory implied by today's policy settings. The announced pledges scenario (APS) assumes that governments met on time and in full the announced targets. The scenario for net zero emissions by 2050 (NZE) aims at a 1.5 °C stabilization in the rise of global average temperatures, while ensuring universal access to modern energy by 2030. Adapted from an IEA report[4].

Unfortunately, by relying on wind and sunlight, respectively, wind turbines and solar photovoltaics are subject to daily, weekly and seasonally production variations. Thus to align the energy demand with the intermittent production of renewable sources, energy storage technologies are mandatory.[4] Pumped-storage hydroelectricity is the currently dominant electricity storage technology, but rechargeable batteries as well as "green" hydrogen produced via electrolysis are envisioned as the future of electricity storage.[4] On the one hand, "green" hydrogen can be converted back to electricity in fuel cells to power heavy duty vehicles (trucks, boats, trains …). But more interestingly, "green" hydrogen is envisioned as a chemical reagent in the production of *e.g.* ammonia, methanol and steel, thus decarbonizing industries usually relying on "grey" hydrogen produced from fossil fuels.[4,5] On the other hand, rechargeable batteries have very good charge/discharge efficiencies and thus are foreseen to be used in personal cars as well as for the electrical grid regulation.[4] However, to match the scale necessary for grid regulation, batteries have to be produced at a scale of hundreds of MW with capacities of hundreds of MWh (such as the 100 MW ; 400 MWh Dalian Flow Battery Energy Storage Peak-shaving Power Station, in Dalian, China).[6] By reaching such a scale, intrinsic safety is needed along with cost minimization and extended lifespan, thus encouraging innovative new aqueous battery chemistries.

Outline of the Thesis

The purpose of this thesis is to promote innovative electrochemical devices relying on the use of novel aqueous biphasic electrolytes, by bringing a better understanding of the opportunities provided by the presence of a liquid-liquid interface. A special emphasis is made on the use of aqueous biphasic systems for batteries and to reach this goal, electrochemical measurements, physico-chemical characterization and spectroscopy studies were carried out. The outcomes of this thesis are presented in five chapters as follow:

Chapter I introduces the current developments carried out to reach safer aqueous Li-ion battery without sacrificing the energy density. An emphasis is made on one recent innovation[7] where two novelties were introduced: i) the intercalation of halogens into graphite positive electrodes and ii) the use of a liquid-liquid interface formed by an aqueous biphasic system (ABS) in intercalation type batteries. To put this work in context, the state of the art knowledge regarding liquid-liquid interfaces and their applications in batteries is given, starting with the electrochemistry of aqueous-organic interfaces before to present the different types of aqueous biphasic systems (ABS) forming aqueous-aqueous interfaces.

As ABS used in Li-ion batteries require extremely high lithium salt concentration, the **Chapter II** investigates the peculiar electrochemistry of highly concentrated aqueous solutions with a focus on their thermodynamics. Measured shifts in electrode potential when increasing the salt concentration are discussed in regard to the change in activity coefficient of salt ions as well as liquid junction potential (LJP) induced at the reference electrode. The LJP, usually neglected in electrochemical measurements, is revealed to be significant for highly concentrated electrolytes. While taking into account the LJP, we found a slight acidification of the electrolytes when increasing the salt concentrations.

Chapter III investigates the role of liquid-liquid interfaces formed when mixing highly concentrated aqueous solutions, and their role in dual ion batteries, with the aim of understanding how salt-salt ABS can promote the intercalation of halogens into graphite. Through a thorough electrochemical study coupled with the use of spectroscopic techniques, ABS are found to enable a two-step mechanism for halogen intercalation into graphite while preventing shuttling of soluble species which is key in reaching good efficiencies for aqueous dual-ion batteries.

Since ABS properties are cornerstone for electrochemical devices, the goal of **Chapter IV** is to bring further knowledge on the chemistry of ABS by investigating the ions partition and the temperature behavior of ABS as well as the surface tension and structure of the aqueous-aqueous interface. Surprisingly, salt-salt ABS interfaces are found to be micrometer thick, compared to nanometer thick water-oil interfaces. The influence of ions and concentrations on the uncommonly large interfacial thickness of ABS is discussed in light of the surface tension measurement and activities of ions.

Finally, in **Chapter V**, we focus on the electrochemistry at liquid-liquid interfaces and describe the design of a micro-holes cell developed during this thesis to perform electrochemical measurements at liquid-liquid interfaces. A comparison between results reported in the literature and results gathered using our cell for water-oil interfaces enables us to confirm the validity of our micro-holes cell design. Using this cell, preliminary results on ion transfer at ABS interface have been obtained and directions to further study ion transfer at ABS interface are discussed.

Overall, this thesis shows the way for a more common use of ABS in electrochemical devices and calls for the investigation of all types of ABS under the light of Raman imaging and liquid-liquid electrochemistry.

Chapter I - State of the Art

I.A. Li-ion batteries

Commercial Li-ion batteries

Commercial Li-ion battery cells are composed of a graphite negative electrode combined with a positive electrode material, often a layered lithium transition metal oxide ($LiMO_2$) with M commonly being nickel, manganese and cobalt. The electrolyte, typically 1 mol.L^{-1} $LiPF_6$ in a mix of ethylene carbonate (EC) and dimethyl carbonate (DMC) or in a mix of EC and ethyl methyl carbonate (EMC) (molar ratio: 1/1 and 3:7, respectively), enables lithium cations to shuttle between electrodes. This technology is described as an intercalation-type rocking chair Li-ion battery as during the charge, Li^+ is de-intercalated from the positive electrode while being intercalated at the negative electrode, and vice-versa during discharge. These reactions are illustrated in **Fig. I-1** and described by the following equations according to the notation commonly accepted in the battery field[8]:

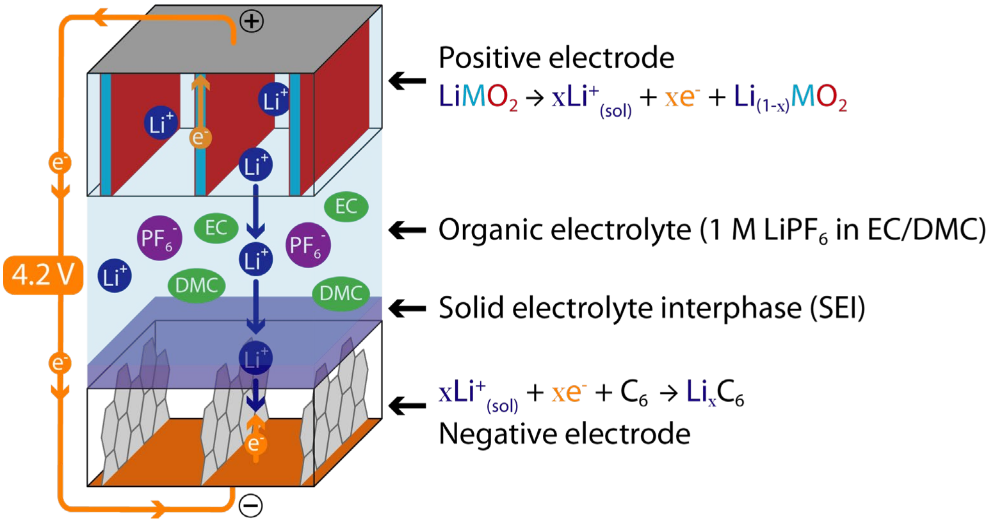

Fig. I-1. Schematic of a commercial rocking chair Li-ion batteries during charge. The Li-ion battery is illustrated with a positive electrode composed of a layered lithium transition metal oxide, an organic 1 M $LiPF_6$ in EC/DMC and an SEI protected graphite negative electrode. Li^+ shuttles from the positive electrode to the negative electrode during charge and *vice versa* during discharge.

$$\text{Positive electrode:}\quad LiMO_{2(s)} \underset{discharge}{\overset{charge}{\rightleftarrows}} xLi^{+}{}_{(sol)} + xe^{-} + Li_{(1-x)}MO_{2(s)} \qquad \text{eq. I} - 1$$

$$\text{Negative electrode:}\quad xLi^{+}{}_{(sol)} + xe^{-} + C_{6(s)} \underset{discharge}{\overset{charge}{\rightleftarrows}} Li_{x}C_{6(s)} \qquad \text{eq. I} - 2$$

$$\text{Full cell:}\quad LiMO_{2(s)} + C_{6(s)} \underset{discharge}{\overset{charge}{\rightleftarrows}} Li_{(1-x)}MO_{2(s)} + Li_{x}C_{6(s)} \qquad \text{eq. I} - 3$$

The graphite negative electrode (C_6/Li_xC_6) (de)intercalates Li^+ at potentials as low as 80 mV vs Li^+/Li where the redox is linked to lithium and graphite depending on the intercalation stage[9] but overall reaching a reversible capacity of 360 mAh.g^{-1} (**eq. I-2**).[10] At such low potentials, the graphite electrode operates below the thermodynamic stability window of the electrolyte, leading to the reduction of solvents and the degradation of salts below 1.7 V vs Li^+/Li for the carbonate-based electrolytes described above. Upon electrolyte reduction, a so-called solid electrolyte interphase (SEI) is formed, *i.e.* a passivating layer which is composed of a dense inorganic inner-layer made of salts components such as lithium fluoride (LiF), lithium oxide (Li_2O) and lithium carbonate (Li_2CO_3), on top of which a porous organic outer-layer deposits. Classically, the SEI forms during the first charge/discharge cycles and, owing to its insoluble nature, remains stable upon further cycling and prevents subsequent reduction of the electrolyte while allowing a high Li^+ conductivity, thus enabling Li^+ intercalation in graphite.[11]

On the other side, positive electrodes such as lithium nickel manganese cobalt oxides (*e.g.* NMC-811: $Li_{(1-x)}[Ni_{0.8}Mn_{0.1}Co_{0.1}]O_2$/$Li[Ni_{0.8}Mn_{0.1}Co_{0.1}]O_2$) (de)intercalate Li^+ in the voltage range of 3.6-4.3 V vs Li^+/Li relying on the metal redox reactions with a reversible capacity of around 200 mAh.g^{-1},[12] providing high energy densities when assembled in full cells with graphite (≈300 Wh.kg^{-1})[13] (**eq. I-1**). However, NMC-based materials suffer from irreversible chemical and mechanical degradations at voltages above 4.2 V vs Li^+/Li, limiting their practical capacity. Furthermore, the quickly growing demand for batteries requires to find new chemistries free from the use of scarce metals, including nickel and cobalt. Hence, positive electrode materials using abundant and inexpensive materials operating at lower potential, such as lithium iron phosphate (LFP: $FePO_4$/$LiFePO_4$) with a reversible capacity of 150 mAh.g^{-1} and a potential of 3.45 V vs Li^+/Li providing energy densities when assembled in full cells with graphite of ≈190 Wh.kg^{-1},[13] are nowadays envisioned as viable materials for replacing or complementing NMC-type materials.[14] Moreover, electrolytes for Li-ion batteries are both a safety issue as they are toxic and flammable and a cost issue as they react with water, forcing the use of expensive dry rooms to manufacture batteries.[15] Thus, to embrace green chemistry principles and reduce costs, extensive research efforts are nowadays placed in developing Li-ion intercalation-type chemistry, which benefits from high voltage and high gravimetric capacities, but using cheap and safe aqueous electrolytes.

Aqueous electrolytes for intercalation type batteries

Using aqueous electrolyte for high-voltage batteries is challenging because the electrochemical stability window of water is only of 1.23 V (**Fig. I-2a**).[16] Indeed, at potential below the stability window, water is reduced to hydrogen through the hydrogen evolution reaction (HER) while at potentials above the stability window, water is oxidized to oxygen through the oxygen evolution reaction (OER), according to the following equations in basic and acidic conditions respectively:

$$\text{Hydrogen evolution reaction (HER):}\quad 2H_2O_{(l)} + 2e^- \xrightarrow{reduction} H_{2(g)} + 2HO^-{}_{(aq)} \qquad \text{eq. I} - 4$$

$$\text{Oxygen evolution reaction (OER):}\quad 2H_2O_{(l)} \xrightarrow{oxidation} O_{2(g)} + 4H^+{}_{(aq)} + 4e^- \qquad \text{eq. I} - 5$$

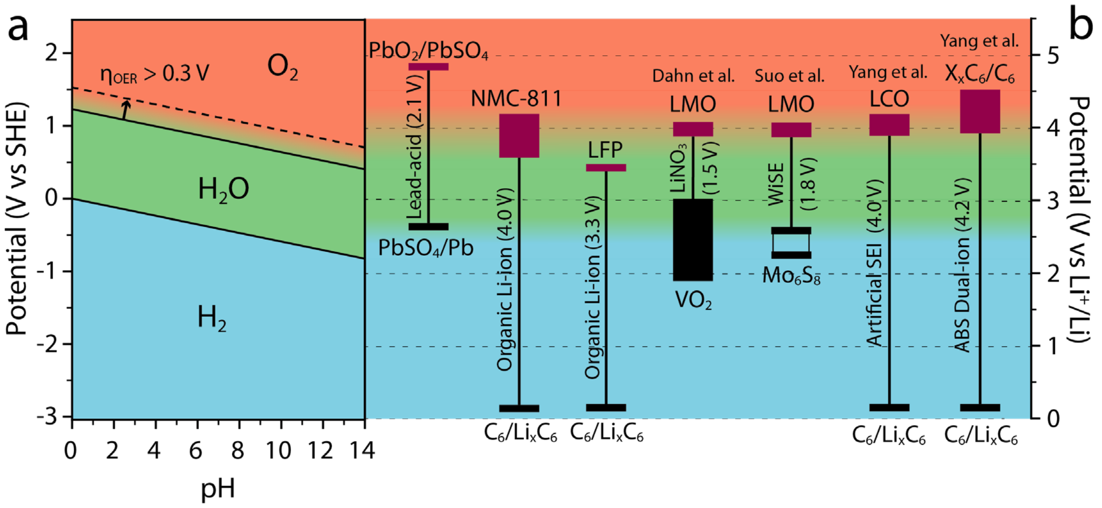

Fig. I-2. Electrochemical stability window of water compared to the potentials of given battery materials. a, Pourbaix diagram of water (solid line) and overpotential for the OER (dotted line). HER takes place at potentials in the blue region. Water is stable at potentials in the green region and OER takes place at potentials in the red region. **b**, Working potentials of negative (in black) and positive (in purple) battery materials for the lead-acid conversion-type battery and Li-ion or dual-ions intercalation-type batteries.

Hence to design efficient high voltage aqueous batteries, the challenge is to prevent water splitting, *i.e.* the electrolyte decomposition, by inducing large HER and OER overpotentials (η_{HER} and η_{OER}) to enable the use of both a low voltage negative electrode without HER parasitic reaction and a high voltage positive electrode without OER parasitic reaction. In comparison, the OER overpotential is often found much greater than the HER one. Indeed, the OER is a four electrons and four protons reaction which is characterized by sluggish kinetics and large overpotential of, at least, 300 mV.[17] As a consequence, positive intercalation battery materials (**Fig. I-2b** in purple) such as NMC-811, lithium cobalt oxide (LCO: $Li_{(1-x)}CoO_2/LiCoO_2$), lithium manganese oxide (LMO: $Li_{(1-x)}Mn_2O_4/LiMn_2O_4$) or LFP can be used in aqueous electrolytes.[18,19] On the contrary, the HER is a two electrons and two protons reaction with a much faster kinetics and a reduced overpotential (for instance, the HER shows nearly no overpotential on platinum electrodes in acidic conditions).[20] Therefore, depending on pH, HER onset potential lies between 2 and 3 V vs Li^+/Li, preventing the use of low voltage negative electrodes (**Fig. I-2b** in black) such as graphite, lithium titanate oxide (LTO; $Li_4Ti_5O_{12}/Li_7Ti_5O_{12}$) or Mo_6S_8 chevrel phase ($Mo_6S_8/LiMo_6S_8$ and $LiMo_6S_8/Li_4Mo_6S_8$).[18,19] Thus, the major challenge in developing high energy density aqueous batteries relies on pushing the HER to lower potential to use low voltage negative battery materials and increase the energy density of aqueous batteries.

Historically, the first aqueous battery successfully commercialized was the conversion-type lead-acid battery which uses electrode materials with high overpotential toward the HER and OER, *e.g.* lead (Pb) and lead oxide (PbO_2) respectively, thus reaching voltage of 2.1 V (**Fig. I-2b**) with acceptable oxygen and hydrogen release and nearly no self-discharge. All these attributes make it a reliable battery widely used even though the high molecular weight of lead and the rather low voltage result in a low energy density (≈40 $Wh.kg^{-1}$)[21–23], compared to 4 V organic Li-ion battery. Hence, in 1994, in an attempt to increase the energy density of aqueous batteries, Dahn J. *et al.*[24] assembled Li-ion batteries using saturated $LiNO_3$ aqueous electrolytes. However, the absence of SEI formation in this electrolyte forced the authors to use a negative electrode within the thermodynamic stability of water, vanadium dioxide (VO_2/Li_XVO_2), thus resulting again in low voltage ≈1.5 V (**Fig. I-2b**) and low energy density of ≈55 $Wh.kg^{-1}$ for a LMO/VO_2 battery that, as a consequence, was never commercialized.

Indeed, nickel-metal hydride batteries developed at the same period showed better performances (≈80 $Wh.kg^{-1}$)[21].

Following these pioneering works, in 2015 Suo *et al.*[25] reported the formation of an SEI in aqueous electrolytes when transitioning from saturated $LiNO_3$ to a so-called water-in-salt electrolytes (WiSE), *i.e.* highly concentrated aqueous electrolytes composed of organic lithium salts (mainly lithium bis(trifluoromethanesulfonyl)imide (LiTFSI), lithium bis(pentafluoro ethanesulfonyl)imide (LiBETI) and lithium trifluoromethane sulfonate (LiOTf)) and in which all water molecules are involved in the Li^+ solvation sheath[26], with concentrations often reported in molalities (m: $mol.kg^{-1}$) instead of molarities (M: $mol.L^{-1}$). The use of organic fluorinated salts, similarly to organic Li-ion battery, results in the decomposition of WiSE during the first cycles forming an SEI composed mainly of an inorganic layer of LiF. Pioneering the development of WiSE-based aqueous Li-ion batteries, Suo *et al.*[25] demonstrated that the use of a 21m LiTFSI electrolyte postponed the HER by 0.5 V following the formation of a LiF-containing SEI, and thus demonstrated a reversible Li-ion battery with LMO as positive electrode and the low potential Mo_6S_8 phase as negative electrode, reaching 2.3 V (**Fig. I-2b**). Following this work, mixed salts were used to reach higher concentration, with for instance a 20m LiTFSI + 8m LiBETI electrolyte enabling the use of lower potential LTO negative electrode.[27,28] Eventually, polymer such as polyethylene glycol (PEG) where mixed with LiTFSI and water to obtained jellified electrolytes, also enabling the use of LTO negative electrode.[29] Despite forming a LiF-containing SEI, this was later on demonstrated not to be sufficient to maintain good performance. Indeed, subsequent studies showed that under slow cycling or resting period, the LiF-based SEI partially dissolves, despite lowering the LiF solubility through common-ion effect and lowering the activity of water[30], and thus does not prevent self-discharge via the reactivity of water at the negative electrode, thus hampering the long term cycling of such batteries.[30,31] Following this realization, artificial-organic SEI were investigated by applying a coating to the negative electrode materials in order to form a passivating layer that can prevent the HER. Using 0.5 $mol.L^{-1}$ LiTFSI in 1,1,2,2-Tetrafluoroethyl-2’,2’,2’-trifluoroethyl ether as artificial passivating SEI layer, Yang *et al.*[32] showed that graphite can be reversibly intercalated in aqueous electrolytes, thus assembling a 4V “aqueous” Li-ion batteries (**Fig. I-2b**).

Subsequent efforts to improve aqueous batteries were then turned to the positive electrode, with the aim to reach higher capacities, long term cycling while being free from transition metal. In this context, Yang *et al.*[7] published in 2019 a new battery concept relying on two novelties, illustrated in **Fig. I-3**. First, Yang *et al.*[7] stepped aside from Li-ion rocking chair batteries and designed a so-called dual-ion battery (see **I.B.**) by coupling the Li^+ intercalation in graphite negative electrode (protected by an artificial SEI) with halogens intercalation into a graphite positive electrode. The report of halogens intercalation into graphite positive electrodes at high voltage (4.0-4.2 V vs Li^+/Li) and with a large capacity (≈240 $mAh.g^{-1}$) is a first. In terms of potential and capacity of the halogen intercalation, this battery can match the state-of-the-art NMC-811 positive electrode, while being safer. Indeed, this new technology uses an aqueous electrolyte and is free from transition metal. However, to implement such as promising battery, Yang *et al.*[7] used a graphite positive electrode mixed with LiBr and LiCl, which, when exposed to a Water-in-bisalt (WiBS) jellified electrolyte, forms a “hydrated LiBr/LiCl layer”. This “hydrated layer” at the positive electrode was proposed to be a non-miscible liquid phase, thus forming a liquid-liquid interface between the WiBS jellified electrolyte and the “hydrated layer”. Thus, and also described simultaneously in our lab by Dubouis *et al.*[33] with the intercalation of Li^+ and Cl^- in Mo_6S_8 and polypyrrole, respectively, the second novelty is the use of a liquid-liquid interface (see **I.C.**) that separates the chemistries of the two electrodes, which is uncommon for intercalation-type batteries.

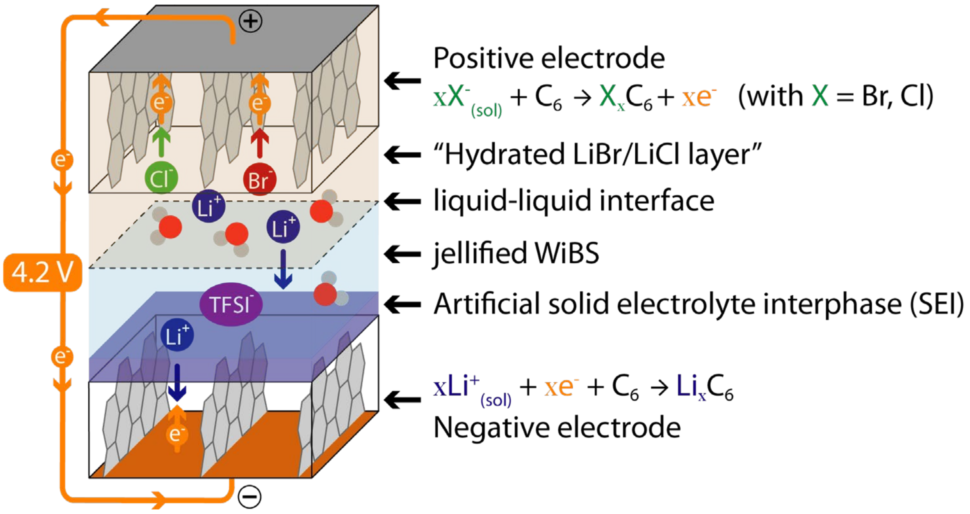

Fig. I-3. Schematic of the aqueous battery proposed by Yang *et al.*[7]. The battery is illustrated with a graphite positive electrode where bromide and chloride are intercalated from the “hydrated LiBr/LiCl layer”. The jellified WiBS forms a liquid-liquid interface with the “hydrated LiBr/LiCl layer” and enables the stability of the artificial SEI at the graphite negative electrode where Li^+ is intercalated.

I.B. Dual-ion battery

Dual-ions battery

Dual-ion batteries are intercalation-type batteries relying on the intercalation of different ions at the positive and negative electrodes. Most commonly, dual ion batteries utilize organic electrolytes, with the intercalation of anions, such as PF_6^-, into graphite positive electrode ($(PF_6)_xC_6/C_6$) coupled with the intercalation of Li^+ into graphite negative electrode, according to the following equations:

$$\text{Positive electrode:}\quad xPF_6{}^-{}_{(sol)} + C_6{}^{pos}{}_{(s)} \underset{discharge}{\overset{charge}{\rightleftarrows}} (PF_6)_xC_6{}^{pos}{}_{(s)} + xe^- \qquad \text{eq. I}-6$$

$$\text{Negative electrode:}\quad xLi^+{}_{(sol)} + xe^- + C_6{}^{neg}{}_{(s)} \underset{discharge}{\overset{charge}{\rightleftarrows}} Li_xC_6{}^{neg}{}_{(s)} \qquad \text{eq. I}-7$$

$$\text{Full cell:}\quad \text{x}LiPF_{6(sol)} + C_6{}^{pos}{}_{(s)} + C_6{}^{neg}{}_{(s)} \underset{discharge}{\overset{charge}{\rightleftarrows}} (PF_6)_xC_6{}^{pos}{}_{(s)} + Li_xC_6{}^{neg}{}_{(s)} \qquad \text{eq. I}-8$$

Although having a high intercalation potential (5.4 V vs Li^+/Li), the intercalation of PF_6^- in graphite (**eq. I-6**) has a much lower reversible capacity (95 $mAh.g^{-1}$) than NMC-811 or LFP. Moreover, as the electrolyte is depleted from both Li^+ and PF_6^- during charge (**eq. I-8**), large quantities of electrolytes are needed to provide enough salt for the charge to be completed. Overall, dual-ion battery are barely competitive (≈70 $Wh.kg^{-1}$)[34] compared to well established conversion-type batteries such as lead-acid (≈40 $Wh.kg^{-1}$)[21] and nickel-metal hydride (≈80 $Wh.kg^{-1}$)[21] batteries and well below the performances of Li-ion batteries (≈300 $Wh.kg^{-1}$)[13].

The dual-ion battery as designed by Yang *et al.*[7] and further studied in following works[35–38] relies on the intercalation of halogens into a positive graphite electrode coupled with Li^+ intercalation in a negative graphite electrode, according to the following equations:

$$\text{Positive electrode:}\quad xX^-{}_{(sol)} + C_6{}^{pos}{}_{(s)} \underset{discharge}{\overset{charge}{\rightleftarrows}} X_xC_6{}^{pos}{}_{(s)} + xe^- \qquad \text{eq. I}-9$$

$$\text{Negative electrode:}\quad xLi^+{}_{(sol)} + xe^- + C_6{}^{neg}{}_{(s)} \underset{discharge}{\overset{charge}{\rightleftarrows}} Li_xC_6{}^{neg}{}_{(s)} \qquad \text{eq. I}-10$$

$$\text{Full cell:}\quad xLiX_{(sol)} + C_6{}^{pos}{}_{(s)} + C_6{}^{neg}{}_{(s)} \underset{discharge}{\overset{charge}{\rightleftarrows}} X_xC_6{}^{pos}{}_{(s)} + Li_xC_6{}^{neg}{}_{(s)} \qquad \text{eq. I}-11$$

Although the halogen intercalation (**eq. I-9**) occurs at lower potential (4.0-4.2 V vs Li^+/Li) compared to PF_6^- intercalation (5.4 V vs Li^+/Li), a much higher capacity (≈240 $mAh.g^{-1}$) was reported by Yang *et al.*[7] compared to other anion intercalation processes, even competing with Li-ion cathode energy densities. However, contrary to more classical dual-ion batteries, a complex electrolyte having a jellified WiBS in contact with a "hydrated LiBr/LiCl layer" was used, but the exact role played by the liquid/liquid interface thus formed on the redox mechanism remains unclear.

I.C. Liquid-liquid interfaces

Electrochemistry is by essence the science of charge transfer at interfaces. Many efforts have been directed to the electrochemistry of solid/liquid interfaces (*e.g.* the double-layer structure with the Gouy-Chapman-Stern (GCS) model, or the electron transfer with the Marcus microscopic model)[39] but relatively less emphasis was put on the electrochemistry of liquid/liquid interfaces. Nevertheless, remarkable advances have been made with liquid/liquid interfaces beyond an electrochemical context with an array of applications such as separation, extraction or phase-transfer catalysis. The specificity of the liquid/liquid interface is that both media can continuously deform at the microscale to allow mass transfer. Beyond mass transfer that has been extensively used for extraction and purification, charge transfer can also occur at liquid/liquid interface. Charge transfer can take place either as i) an electron transfer, as previously used to direct electrosynthesis of polymers, or more importantly in this thesis ii) via ion transfer which can be directed to the design of novel bifunctional liquid electrolytes, as recently applied to redox flow batteries.

Redox flow batteries

Contrary to intercalation-type batteries where energy is stored in a solid through reversible intercalation into the electrode materials, in redox flow batteries, energy is stored in liquids via two redox active species solubilized in two electrolytes. One electrolyte, the positive electrolyte, contains a high potential redox species and is in contact with the positive electrode while the negative electrolyte in contact with the negative electrode contains a low potential redox species. Upon charge, the redox couple from the positive electrolyte

(Ox_{pos}/Red_{pos}) is oxidized and the redox couple from the negative electrolyte (Ox_{neg}/Red_{neg}) is reduced while charge balance is ensured by ions crossing the membranes, and *vice versa* during discharge. This is illustrated in **Fig. I-4** with the state-of-the-art vanadium redox couples, following the equations:

$$\text{Positive electrode/electrolyte: } VO^{2+}{}_{(aq)} + H_2O_{(l)} \underset{discharge}{\overset{charge}{\rightleftarrows}} VO_2{}^{+}{}_{(aq)} + 2H^{+}{}_{(aq)} + e^{-} \quad \text{eq. I} - 12$$

$$\text{Negative electrode/electrolyte: } \quad V^{3+}{}_{(aq)} + e^{-} \underset{discharge}{\overset{charge}{\rightleftarrows}} V^{2+}{}_{(aq)} \quad \text{eq. I} - 13$$

$$\text{Membrane: } \quad H^{+}{}_{(pos)} \underset{discharge}{\overset{charge}{\rightleftarrows}} H^{+}{}_{(neg)} \quad \text{eq. I} - 14$$

$$\text{Full cell: } \quad VO^{2+}{}_{(aq)} + H_2O_{(l)} + V^{3+}{}_{(aq)} \underset{discharge}{\overset{charge}{\rightleftarrows}} VO_2{}^{+}{}_{(aq)} + 2H^{+}{}_{(aq)} + V^{2+}{}_{(aq)} \quad \text{eq. I} - 15$$

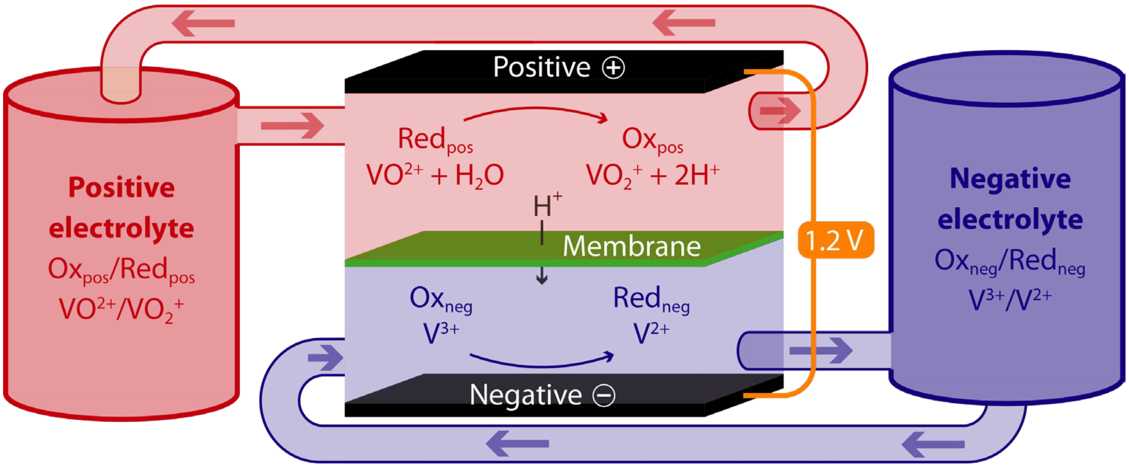

Fig. I-4. Schematics of the all vanadium redox flow battery. In the positive electrolyte, VO^{2+} is oxidized to VO_2^{+} while at the negative V^{3+} is reduced to V^{2+}. Protons cross the Nafion membrane to ensure charge balance.

To prevent self-discharge through mixing of the species, the positive and negative electrolytes must be kept apart. Classically, the two electrolytes are separated by a cation exchange membrane (Nafion-based). However, membranes present numerous drawbacks, being i) expensive (≈40% of total cost of redox flow batteries)[40–42], ii) short-lived in the acidic environment required for all vanadium redox flow batteries[40], iii) poorly conductive[40,42], thus adding a resistance to the system and iv) not selective enough[40,42], leading to crossover of vanadium species, for instance, that plagues the efficiency of all vanadium redox flow batteries.

Membrane-less redox flow batteries

To sidestep the issue of membranes, starting as early as 1862, Callaud proposed a gravity cell by removing the membrane of a primary Daniel cell (Zn|$ZnSO_4$+$CuSO_4$|Cu), thus obtaining a very low resistance device, but with drawbacks in term of efficiency and design.[43] Indeed, the cell has to be kept steady in order to avoid mixing zinc sulfate and copper sulfate which are separated only by slow diffusion due their density difference.[43] Much more recently, membrane-less redox flow batteries were designed by relying on laminar flow to minimize the mixing of the positive and negative electrolytes. Nevertheless, such technology again presents drawbacks in term of design, often using micro-fluidic devices with very low current densities, thus being challenging to upscale. Furthermore, an efficiency of only ≈20% is achieved because of the mixing issue during charge and discharge.[44–49] Indeed, both the Callaud and the laminar redox flow batteries used two liquid electrolytes that are thermodynamically miscible at room temperature and for which mixing is minimized either through density difference or the use of a laminar flow. However, even if being minimized, the mixing leads to large crossover and thus low efficiency along with fast self-discharge.

In contrast to the Callaud and the laminar redox flow batteries which are using miscible electrolytes, thermodynamically immiscible liquids were recently investigated for secondary battery applications. First example is the so-called liquid metal battery for which both electrodes and the electrolyte are liquid.[50] A second example is based on the immiscibility of water with polar organic solvent, allowing to assemble a zinc-ferrocene redox battery with zinc plating at the negative electrode, using a zinc chloride aqueous negative electrolyte, coupled with the redox couple ferrocenium/ferrocene (Fc^+/Fc) at the positive electrode in Butyl acetate (BuAcO) with a mixture of tricaprylylmethylammonium chloride and trioctylmethylammonium chloride as supporting salt (Aliquat 336).[51,52] In this pioneering work, no electrolyte flow was applied and the technology suffers from a high resistance due to the low conductivity of the organic phase (≈0.1 $mS.cm^{-1}$)[53] as well as large self-discharge due to crossover of ferrocenium/ferrocene owing to its solubility in the aqueous phase. On the one hand, further works moved away from the "static" battery, using a stirred electrode, or achieving a redox "flow" battery.[54,55] On the other hand, new chemistries were also investigated by spanning different organic solvents, ionic liquids and redox species to reduce crossover.[56–58] The best technology thus far appears to be achieved when using two organic immiscible electrolytes, to reach a high capacity lithium sulfur battery[59] with the following reactions:

$$\text{Positive electrode/electrolyte:}\quad 8\,Li_2S_{\,(sol)} \underset{discharge}{\overset{charge}{\rightleftarrows}} S_{8(sol)} + 16\,Li^{+}{}_{(sol)} + 16\,e^{-} \qquad \text{eq. I} - 16$$

$$\text{Liquid} - \text{liquid interface:}\quad 16\,Li^{+}{}_{(pos)} \underset{discharge}{\overset{charge}{\rightleftarrows}} 16\,Li^{+}{}_{(neg)} \qquad \text{eq. I} - 17$$

$$\text{Negative electrode:}\quad 16\,Li^{+}{}_{(sol)} + 16\,e^{-} \underset{discharge}{\overset{charge}{\rightleftarrows}} 16\,Li_{(s)} \qquad \text{eq. I} - 18$$

$$\text{Full cell:}\quad 8\,Li_2S_{(sol)} \underset{discharge}{\overset{charge}{\rightleftarrows}} 16\,Li_{(s)} + S_{8(sol)} \qquad \text{eq. I} - 19$$

As seen with **eq. I-17**, ion crossing at the liquid-liquid interface between the two immiscible electrolytes is necessary to maintain the charge balance of the electrolytes. Hence to better understand the impact of a liquid-liquid interface on these applied systems, including potential kinetics limitations due to ion transfer or any overpotential due to large energy for ion transfer, it is important to understand the structure and reactions at electrified liquid-liquid interfaces.[60]

Interface between two immiscible electrolytes (ITIES)

Even though electrochemical applications of liquid-liquid interface are very recent, the interface between to immiscible electrolytes (ITIES) have been studied for more than 50 years starting from early reports of ion[61] and electron[62] transfer at ITIES formed between water with inorganic salts and nitrobenzene with organic salts. Transfer of an ion (X) at an ITIES formed between an aqueous electrolyte (aq) and an organic electrolyte (org) can be represented with the following equations:

$$\text{Ion transfer:}\quad X_{(aq)} \leftrightarrow X_{(org)} \qquad \text{eq. I} - 20$$

At equilibrium, a salt of stoichiometry 1:1 is distributed between the two phases according to the salt partition coefficient with the following equation:

$$K_{salt} = \frac{a_{X^+}{}^{org} a_{X^-}{}^{org}}{a_{X^+}{}^{aq} a_{X^-}{}^{aq}} = exp\left(\frac{-\Delta G^\circ{}_{salt}^{aq\to org}}{RT}\right) \qquad \text{eq. I} - 21$$

$$with \qquad \Delta G^\circ{}_{salt}^{aq\to org} = \Delta G^\circ{}_{X^+}^{aq\to org} + \Delta G^\circ{}_{X^-}^{aq\to org} \qquad \text{eq. I} - 22$$

with $\Delta G^\circ{}_{salt}^{aq\to org}$ the standard Gibbs free energy required to transfer the salt from the aqueous phase to the organic phase and $\Delta G^\circ{}_{X}^{aq\to org}$ the standard Gibbs free energy required to transfer an ion X from the aqueous phase to the organic phase. Positive $\Delta G^\circ{}_{X}^{aq\to org}$ values mean that ions are preferentially in water, *i.e.* hydrophilic ions, while ions preferentially in the organic phase, *i.e.* hydrophobic ions, have negative $\Delta G^\circ{}_{X}^{aq\to org}$ values.[39,63–65] For quantification, one need to make an extrathermodynamic assumption and it is usually assumed that tetraphenylarsonium (TPAs$^+$) and tetraphenylborate (TPB$^-$) have equal standard Gibbs free energy of transfer for any pair of solvent[63–65]:

$$\Delta G^\circ{}_{TPAs^+}^{aq\to org} = \Delta G^\circ{}_{TPB^-}^{aq\to org} = \frac{1}{2}\,\Delta G^\circ{}_{TPAsTPB}^{aq\to org} \qquad \text{eq. I} - 23$$

Following this, one can define a standard ion-transfer potential for ion X with a charge z:

$$\Delta\phi^\circ{}_{X}^{aq\to org} = \frac{\Delta G^\circ{}_{X}^{aq\to org}}{zF} \qquad \text{eq. I} - 24$$

and the corresponding Nernst equation for the difference between the inner Galvani potentials of the aqueous (ϕ^{aq}) and organic (ϕ^{org}) phases:

$$\phi^{aq} - \phi^{org} = \Delta\phi^{aq\to org} = \Delta\phi^\circ{}_{X}^{aq\to org} + \frac{RT}{zF} ln\left(\frac{a_X{}^{org}}{a_X{}^{aq}}\right) \qquad \text{eq. I} - 25$$

As an example, for ion transfers between water and 1,2-Dichloroethane (DCE), Li$^+$ and Cl$^-$ have positive $\Delta G^\circ{}_{X}^{aq\to org}$ values, 56 kJ.mol^{-1} and 51 kJ.mol^{-1}, respectively, due to their hydrophilicity while tetrabutylammonium (TBA$^+$) and TPB$^-$ are found hydrophobic with negative $\Delta G^\circ{}_{X}^{aq\to org}$ of -22 kJ.mol^{-1} and -35 kJ.mol^{-1}, respectively.[64] Hence without applied potential, hydrophobic Li^+ and Cl^- reside in the aqueous phase while TBA^+ and TPB^- are in the organic phase.

Polarizable and non-polarizable ITIES

Similarly to the electrochemistry at solid/liquid interface, the ion transfer at liquid/liquid interface can be driven by applying a potential difference between the aqueous and organic phases. Keeping the same example of aqueous LiCl solutions and DCE containing TBATPB, according to **eq. I-25**, Li^+ can be transferred from the aqueous to the DCE phase by applying an interfacial Galvani potential difference superior to the standard ion-transfer potential, *i.e.* $\Delta\phi^{aq\rightarrow org} > \Delta\phi^{\circ}{}_{Li^+}^{aq\rightarrow org}$ = 576 mV.[64] For aqueous anions such as Cl^-, as the charge z is negative in **eq. I-25**, an interfacial Galvani potential difference inferior to the standard ion-transfer potential is needed, *i.e.* $\Delta\phi^{aq\rightarrow org} < \Delta\phi^{\circ}{}_{Cl^-}^{aq\rightarrow org}$ = -528 mV.[64] As for TBA^+ and TPB^-, since they are transferred from the DCE phase to the aqueous phase, the cations and anions role are inverted with standard ion-transfer potentials of -230 mV and 365 mV respectively.[39] Overall, decreasing $\Delta\phi^{aq\rightarrow org}$ leads to the transfer of aqueous anions to the organic phase as well as the transfer of cations from the organic phase to the aqueous phase. On the contrary, increasing $\Delta\phi^{aq\rightarrow org}$ leads to the transfer of aqueous cations to the organic phase as well as the transfer of anions from the organic phase to the aqueous phase (**Fig. I-5**).

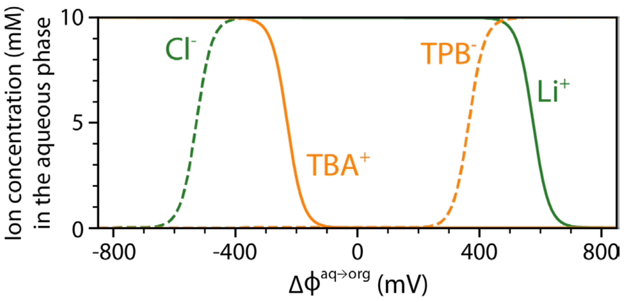

Fig. I-5. Distribution of ions in an aqueous 10 mM LiCl in contact with 10 mM TBATPB in DCE as a function of the interfacial Galvani potential difference, $\Delta\phi^{aq\rightarrow org}$. Concentration profiles of cations (solid lines) and anions (dotted lines) for TBATPB (orange) and LiCl (green). Adapted from Bard *et al.*[39] with values from Shao[64].

Finally, the applied potential only polarizes the interface if the potential is kept within the range where no ion transfer takes place:

$$max\left(\Delta\phi^{\circ}{}_{TBA^+}^{aq\rightarrow org};\Delta\phi^{\circ}{}_{Cl^-}^{aq\rightarrow org}\right) \ll \Delta\phi^{aq\rightarrow org} \ll min\left(\Delta\phi^{\circ}{}_{Li^+}^{aq\rightarrow org};\Delta\phi^{\circ}{}_{TPB^-}^{aq\rightarrow org}\right) \qquad \mathrm{eq.\,I-26}$$

Following **eq. I-26**, if a range of potential exists where the potential can be changed without ion transfer, the interface is called a polarizable ITIES which is the case of the interface between aqueous LiCl solution and TBATPB in DCE in the potential range between -100 mV and 250 mV (**Fig. I-5**).[39,63]

On the contrary, if the potential is fixed and cannot be varied without resulting in ion transfer, the ITIES is non-polarizable. This is the case for example of ITIES with a common ion in the aqueous and organic phases. Indeed, keeping the previous example but replacing Li^+ by TBA^+, for an aqueous phase of TBACl in contact with a TBATPB in DCE phase, we have the following:

$$max\left(\Delta\phi^{\circ}{}_{TBA^+}^{aq\rightarrow org};\Delta\phi^{\circ}{}_{Cl^-}^{aq\rightarrow org}\right) = min\left(\Delta\phi^{\circ}{}_{TBA^+}^{aq\rightarrow org};\Delta\phi^{\circ}{}_{TPB^-}^{aq\rightarrow org}\right) = \Delta\phi^{\circ}{}_{TBA^+}^{aq\rightarrow org} \qquad \mathrm{eq.\,I-27}$$

Thus, from **eq. I-26** and **eq. I-27**, no potential range exists where $\Delta\phi^{aq\rightarrow org}$ can be freely varied without ion transfer. As soon as the potential is changed, TBA^+ is transferred according to the TBA^+ Nernst equilibrium.

Structure of the liquid-liquid interfaces

To better understand ITIES and the reactions taking place at the liquid-liquid interface, the structure of ITIES was studied, originally with the water-nitrobenzene interface. Spectroscopic measurements and simulations established that ITIES are molecularly sharp interfaces but with an interfacial roughness due to thermal capillary wave proportional to $\sqrt{k_BT/\gamma}$, which is estimated to be ≈1 nm in amplitude.[60,66] The first studies of the molecularly sharp interface relied mainly on surface tension and capacitance, and led to the so-called modified Verwey-Niessen (MVN) model assuming a molecularly sharp interface only based on oriented solvents molecules of water and nitrobenzene, thus excluding the role of ions. This model was shown not to be valid when changing nitrobenzene to DCE or when changing the salts ions and concentrations, overall demonstrating the key role of both the solvents and the ions on the structure of ITIES.[60] Thus, taking into account ion-solvent interaction, the Poisson-Boltzmann potential of mean force (PB-PMF) model was developed, predicting sharp ion density profiles at the interface, in agreement with experimental results.[67] However, the PB-PMF model is only using the solvents macroscopic dielectric constants, and thus does not properly model molecular interactions and solvent re-orientation of molecularly sharp ITIES, missing essential molecular interactions at the liquid-liquid interface. Indeed recent studies demonstrated that molecular interactions were key as liquid-liquid interfaces are composed of two monolayer of ions on each side of the interface without any diffuse layer of ions, in stark contrast with solid/liquid interfaces that are usually composed of an adsorbed layer of ions (Stern Layer) and a diffuse layer of ions (Gouy-Chapman diffuse layer).[39,68–70]

Mechanism and kinetics of ion transfer at liquid-liquid interfaces

To design more efficient liquid-liquid interfaces for applied electrochemical systems, gaining insights about ion transfer kinetics and mechanisms is crucial. The kinetics of ion transfer at liquid/liquid interfaces is described similarly to solid-liquid interfaces.[39] The flux of ion from the aqueous phase to the organic phase is described by a first-order rate law:

$$J_X^{aq\rightarrow org} = k_f . {c_X}^{aq} - k_b . {c_X}^{org} \qquad \mathrm{eq. I-28}$$

with k_f and k_b respectively the forward and backward transfer rate constants described by the Butler-Volmer formalism, k_0 the apparent standard rate constant, and α the apparent charge transfer coefficient:

$$k_f = k_0 \exp\left[\frac{\alpha zF\left(\Delta\phi^{aq\rightarrow org} - \Delta\phi^{\circ}{}_X^{aq\rightarrow org}\right)}{RT}\right] \qquad \mathrm{eq. I-29}$$

$$k_b = k_0 \exp\left[\frac{-(1-\alpha) zF\left(\Delta\phi^{aq\rightarrow org} - \Delta\phi^{\circ}{}_X^{aq\rightarrow org}\right)}{RT}\right] \qquad \mathrm{eq. I-30}$$

Taking the values for the transfer of tetraethylammonium (TEA^+), the upper theoretical limit of k_0 is ≈100 $cm.s^{-1}$ for an optimized diffusion-limited process. However, based on both experiments and simulations, slower kinetics (≈0.1-1 $cm.s^{-1}$) of ion transfer are found, and explained by the presence of activation barriers slowing down the transfer of cations or anions from one phase to the other.[71] Two mechanisms are envisioned for the transfer of ions: the “water finger” or the “ion shuttle”.[60] For the water finger mechanism (**Fig. I-6a**), the energy barrier is thought to be linked to the formation/breaking of a series of hydrogen bounded water molecules forming a water finger ensuring the transfer of ion, the ion transfer is thus *a priori* independent on the other ions.[72] On the contrary, for the ion shuttle mechanism (**Fig. I-**

6b), cations are associated to anions, forming ion pairs, before to be transferred from one phase to the other, and *vice versa* for anion transfer.[73]

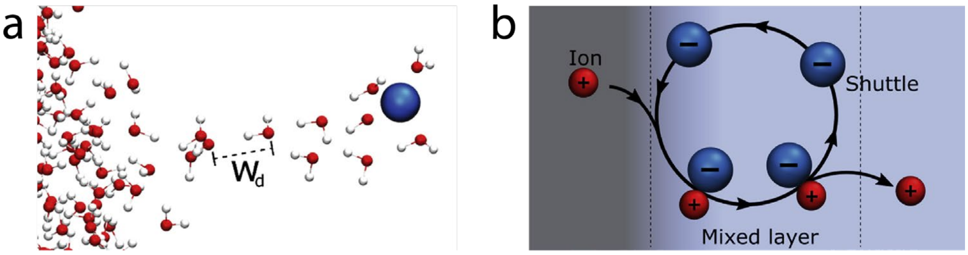

Fig. I-6. The two mechanisms envisioned for the transfer of ions at ITIES. a, Illustration of the water finger mechanism with W_d the coordinate as defined by Kikkawa *et al.*[72]. **b**, Illustration of the ion shuttle mechanism as defined by Laforge *et al.*[73]. Figures from Gschwend *et al.*[60].

I.D. Aqueous biphasic systems (ABS)

As described previously, most of the biphasic systems studied at a fundamental level and biphasic systems used in applied devices rely on an aqueous phase in contact with an organic phase. However, the high cost and low conductivity (≈10 $mS.cm^{-1}$)[53,55,74,75] of the organic phases hinder the development of large scale electrochemical devices using organic/aqueous biphasic electrolytes. Hence, owing to their reduced cost and better conductivities (≈100 $mS.cm^{-1}$)[53,75], latest efforts in designing membrane-less redox flow batteries have turned to biphasic systems made out of two aqueous phases, the so called aqueous biphasic systems (ABS) or aqueous two-phase systems (ATPS).[76–78]

Polymer-polymer ABS

In 1896, Beijerinck M. W. reported that when an aqueous solution of gelatin was mixed with a polysaccharide (either agar or soluble starch)[79–81] in concentrations of few weight percent, the solution was turbid. When allowed to sit for a while, two phases were reported to be formed with a gelatin-rich phase and a polysaccharide-rich phase. Phase separation between two polymers is common[82], and such immiscible systems are designated in the literature as ABS or ATPS. Taking the example of the historical PEG-Dextran-H_2O system[83], these ABS can be reported either with usual ternary triangular diagrams (**Fig. I-7a**) or more recently as simplified orthogonal diagrams omitting the water content (**Fig. I-7b**). These ternary systems are miscible at low polymers weight percentage while at higher weight percentage (such as the green points A in **Fig. I-7**), a phase separation occurs, leading to the formation of two distinct solutions which compositions (green points B and C in **Fig. I-7**) are described by the tie lines (green dash-dotted lines in **Fig. I-7**).[83] As a general rule of thumb, longer polymer chains will phase separate at lower weight percentage as shown when moving from the PEG 8000 (black dashed lines in **Fig. I-7**) to the PEG 20000 (black solid lines in **Fig. I-7**) where the latter separates at lower weight percentage.[83]

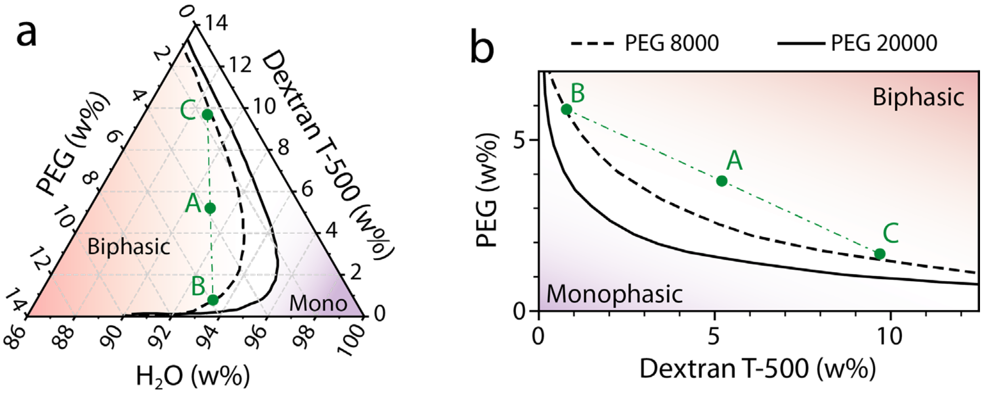

Fig. I-7. Two different representations of the same phase diagrams for PEG-Dextran-H_2O systems. **a**, Triangular representation of the phase diagrams for ternary PEG-Dextran-H_2O systems. **b**, Orthogonal representation of the phase diagrams for ternary PEG-Dextran-H_2O systems. The diagrams are that of Dextran T-500 associated with PEG 20000 (solid line) or PEG 8000 (dashed line). The purple area represents the monophasic side of the binodal curves while the red area represents the biphasic side of the binodal curves. The green dash-dotted lines represents the tie line for the composition of the biphasic system of the green points A, which separates into two phases of compositions given by the green points B and C. Adapted from Diamond *et al.*[83].

However, the driving force for phase separation is still subject to debate and, despite numerous studies dedicated to study the phenomenon, it remains unclear if the phase separation can be rationalized by the large enthalpy gain against a small entropy loss when de-mixing large molecules such as polymers (Flory-Huggins theory) or can be rationalized by the very different structure of polymeric water structures.[84–86] Nevertheless, starting from the work of Albertsson, polymer-polymer ABS have been used as biocompatible systems for the extraction, separation and purification of biological products (proteins, peptides, nucleic acids, …), following the biologic product size and affinity with each phase.[79,86,87] The large variety of non-ionic (dextran (DEX), polyethylene glycol (PEG), polypropylene glycol (PPG), polyvinylpyrrolidone (PVP), polyvinyl alcohol (PVA), …) and ionic (dextran sulfate, polyacrylic acid (PAA), polyacrylamide (PAM), …) polymers available to form ABS enables to fine tune the extraction properties and reach even more complex multi-phased systems, *i.e.* with more than two phases.[79,86,88]

Polymer-salt ABS

Apart from polymer-polymer ABS, Albertsson also first reported the formation of ABS when mixing a polymer with a salt, thus opening even more possibilities for extraction applications.[89] Since then, this so-called polymer-salt ABS have been widely studied with different polymer and salt combinations.[86] For the polymer, it is found that longer PEG chains facilitate the phase separation, alike for polymer-polymer ABS.[90] For the salts, PEG have been studied in combination with different sodium salts showing that anions with a "salting-in" ability, such as chloride (Cl^-) and nitrate (NO_3^-), have a lower tendency to form ABS while on the contrary anions with a "salting-out" ability, such as carbonate (CO_3^{2-}), have a higher tendency to form ABS.[86,91] Hence ABS formation follows the "salting-in/salting-out" ability of anions as expressed by the Hofmeister series (also called lyotropic series). Originally, the Hofmeister series was established according to the ability of anion to either precipitate folded proteins ("salting-out") or on the contrary, to unfold proteins, thus increasing their solubility ("salting-in").[92] However, translating a macroscopic phenomenon such as the precipitation of a protein to molecular parameters is not easy. Different parameters have been used to rationalize the Hofmeister series, leading to series valid within a family of ions but often showing discrepancies when changing from cations to anions or from inorganic to organic ions.

The first parameter to rationalize the "salting-in/salting-out" ability of salts was the viscosity measured as function of concentration, fitted with the Jones-Doles equation:

$$\frac{\eta}{\eta_0} = 1 + A\sqrt{c} + Bc \quad with \quad B = \sum_i B_i \qquad eq. I-31$$

With η_0 the viscosity of pure water, η the viscosity of water with a concentration c of salt, A the salt coefficient for charge-charge interactions and B the salt coefficient and B_i the ions coefficients for solvent-charge interactions.[93–95] By convention, KCl is considered as a reference, with $B_{K^+} = B_{Cl^-} \approx 0$. Following this methodology, for $B_i > 0$, the ion is considered kosmotropic, *i.e.* the ion-water interaction is stronger than the water-water interaction. On the contrary, for $B_i < 0$ the ion is considered chaotropic, *i.e.* that the ion-water interaction is weaker than water-water interaction. Hence, kosmotropic ions do not interact with water and only locally weaken the water hydrogen bonding network while chaotropic ions disturb the water hydrogen bonding network.

For anions, the following order is obtained for B_- coefficient:

$$\begin{array}{ccc} "Salting-out" & & "Salting-in" \\ \mathrm{B}_- > 0 & \mathbf{B_- \approx 0} & \mathrm{B}_- < 0 \end{array} \qquad eq.I-32$$

$$\mathrm{CH_3CO_2}^- > \mathrm{SO_4}^{2-} > \mathrm{F}^- > \mathrm{HCO_2}^- > \mathbf{Cl}^- > \mathrm{Br}^- > \mathrm{NO_3}^- > \mathrm{ClO_4}^- > \mathrm{I}^- > \mathrm{SCN}^-$$

However, for cations, the reverse order is obtained, as positive B_+ coefficient leads to “salting-in” phenomenon and *vice versa*:

$$\begin{array}{ccc} "Salting-in" & & "Salting-out" \\ \mathrm{B}_+ > 0 & \mathbf{B_+ \approx 0} & \mathrm{B}_+ < 0 \end{array} \qquad eq.I-33$$

$$Al^{3+} > \mathrm{Mg}^{2+} > \mathrm{Ca}^{2+} > \mathrm{Ba}^{2+} > \mathrm{Li}^+ > \mathrm{Na}^+ > \mathbf{K}^+ > \mathrm{NH_4}^+ > \mathrm{Rb}^+ > \mathrm{Tl}^+ > \mathrm{Cs}^+$$

This reverse order is believed to be due to the interaction of cations with the polymer functional groups, such as oxygen for PEG.[86,91]

The Hofmeister series partially follows the same trend as the Gibbs free energy of hydration (ΔG_{hyd}) from which the entropic part (ΔS_{hyd}) is believed to be key.[96,97] However, one has to be careful with such series, indeed, some cations such as tetramethylammonium (Me_4N^+) are not classified the same way when using the Jones-Doles equation (kosmotropic, $\mathrm{B}_+ > 0$)[95] as when using the Gibbs free energy of hydration ($\Delta G_{hyd} \approx 0$)[98]. Hence, no parameter was found to be universal for cations/anions or organic/inorganic ions and the current understanding is that polymer-ABS are formed more easily with salts taking water from the polymer (“salting-out”) while not interacting with the polymer.[86,91]

Ionic liquid-salt ABS

In 2003, following the pioneering works on polymer-salt ABS, Rogers R. D. *et al.* reported an aqueous solution composed of ionic liquid to form an ABS upon the addition of a kosmotropic salts.[99] Further works proved that salt with more negative ΔG_{hyd} (“salting-out”), leads to the formation of ionic liquid-salt ABS more easily.[86,100] Analogous to the case of polymer-salt ABS, ΔS_{hyd} is believed to be key in forming ABS,[101–103] with overall, the same understanding than for polymer-salt ABS, *i.e.* that the salt has to de-hydrate the ionic liquid to generate the phase separation of the ABS. Following this logic, it was found that more "hydrophobic", *i.e.* chaotropic, ionic liquids are forming ABS as they can be dehydrated more easily. On the contrary, more "hydrophilic", *i.e.* kosmotropic, ionic liquids are more difficult to de-hydrate thus being less prone to forming ABS.[102,103] As a consequence, ABS are found to be more easily formed with ionic liquid having longer hydrophobic alkyl chains.[102,104] To further rationalize the "hydrophobicity/hydrophilicity", *i.e.* chaotropicity/kosmotropicity, of ionic liquids, the capacity of ionic liquids to accept a proton via hydrogen bounding, *i.e.* hydrogen bonding basicity (β), which is experimentally determined by solvatochromism, was correlated to the capacity of ionic liquids to induce the formation of ABS. It was found that ionic liquids with lower hydrogen bonding basicity, *i.e.* ionic liquids that do not accept protons from hydrogen bounding, correlate with an easier formation of ionic liquid-salt ABS.[102–106]

Overall, it is found that a chaotropic ionic liquid associated to a kosmotropic salts are needed to form an ABS. Such understanding of the ionic liquid "hydrophobicity/hydrophilicity" and of salt "salting-out" role is of utmost importance to optimize each phase of the ABS in order to design better extraction processes.[102] Due to their tunability, ionic liquid-salt ABS offer more possibilities of extractions than the previously studied polymer-polymer or polymer-salt ABS. More interestingly, each phase forming the ionic liquid-salt ABS are fairly conductive, with one phase having the salt ions and high conductivity[77] ≈100 mS.cm^{-1} and the other phase having ionic liquid ions, with conductivity[77] in the order of ≈10 mS.cm^{-1}.

Salt-Salt ABS

While searching for improved aqueous electrolytes such as the WiSE discussed in **I-A**, Dubouis *et al.* found that mixing LiTFSI with LiCl at high concentration leads to the formation of a salt-salt ABS.[33] Interestingly, both salts contain the same cation (Li^+), thus this salt-salt ABS is driven by anions with one inorganic (Cl^-) and one organic anion ($TFSI^-$). This ABS does not follow the condition previously discussed for ionic liquid-salt ABS formation, where both kosmotropic and chaotropic species are needed. Indeed, viscosity measurements indicated that both Cl^- and $TFSI^-$ anions have positive B_- values, thus both being kosmotropic. However, by changing the organic anions $TFSI^-$ to a smaller sulfonamide anion (FSI^-), no ABS was obtained with LiCl or any other lithium halide salt. On the contrary, when changing $TFSI^-$ to a bigger sulfonamide ($BETI^-$), the ABS is obtained more easily, *i.e.* at lower concentration.[107] As a consequence, the trend for organic anions concur with the trend observed for the ionic liquid in ionic liquid-salt ABS: bigger, more hydrophobic, organic ions leads to easier formation of ABS. Nevertheless, no difference was found with different lithium halides (LiCl, LiBr, LiI) as they are all forming an ABS when mixed with LiTFSI, with similar phase diagrams,[107] thus questioning previous series as halides have different size[107], B coefficient,[95] ΔG_{hyd}[98], ΔS_{hyd}[108] and hydrogen bonding basicity[109] values. Furthermore lithium nitrate ($LiNO_3$) or lithium perchlorate ($LiClO_4$) were shown not to form ABS with LiTFSI despite their similarities with halides in size[107], B coefficient,[95] ΔG_{hyd}[98], ΔS_{hyd}[108] and hydrogen bonding basicity[109] values. Dubouis *et al.* rationalized the differences between halides and perchlorate or nitrate by a large difference in shape,[107] bearing in mind that ABS have large packing constrains since they are formed at high concentration of salts. Furthermore, effect related to interactions with the environment, such as through hydrogen bounding, can also be involved.

Overall, this new type of ABS shows that the correlations found for polymer-polymer, polymer-salt or ionic liquid-salt ABS are not general and can be challenged when new immiscible liquid systems are found. But, interestingly, novel opportunities to build electrochemical devices are brought by the finding of salt-salt ABS, with for instance the design of LiTFSI-LiCl-water biphasic system where each phase has a high conductivity[110,111], leading to electrochemical devices such as the work of Yang *et al.*[7] and Dubouis *et al.*[33]

Chapter Conclusions

Liquid-liquid phase separation is a cornerstone for the extraction and purification at industrial scale. However, the use of liquid-liquid interfaces in electrochemical devices lags behind compared to that of solid-liquid interfaces. Most of the knowledge on electrochemistry of liquid-liquid interface is coming from fundamental studies of water-oil interfaces, and only few attempts to use water-oil interfaces in applied electrochemical systems were made. Comparatively, even though ABS have been known for more than 100 years, the electrochemistry of aqueous-aqueous interface is rather unexplored. Indeed, the first ABS discovered were polymer-polymer ABS and polymer-salt ABS and were rapidly used as biocompatible liquid-liquid phase separation media. However, polymer-rich phases have low conductivities, preventing their use in electrochemistry. In contrast, ionic liquid-salt ABS and salt-salt ABS have been recently developed and very recent work using these ABS in redox flow batteries showed how promising ionic liquid-salt and salt-salt ABS can be for energy storage devices. Indeed, by spontaneously forming two conductive aqueous phases, ABS can segregate the positive and negative redox couples without the need for expensive and short-lived ion-specific membranes. Salt-salt ABS were thus recently used by Yang *et al.*[7] to enable the design of a dual-ion battery by taking advantage of the two different ABS phases to drive two different intercalation reactions, Li^+ intercalation and halogens intercalation, respectively in negative and positive graphite electrodes.

Despite the recent development of redox flow and dual-ion batteries using ABS, the electrochemistry of ABS is still in its infancy. Salt-salt ABS are formed at high salts concentration, i) making their electrochemistry potentially differing from that of more classical dilute solutions, as previously observed for WiSE, and ii) enabling new chemistries such as the reversible intercalation of halogens in graphite proposed by Yang *et al.*[7]. Contrary to the molecularly sharp water-oil interfaces formed due to the immiscibility of solvents, the formation of ABS is driven by solutes. This difference raises numerous questions regarding the structure of the aqueous-aqueous interface with possible impact on the kinetics of ion transfer.

Chapter II – Electrochemistry of highly concentrated aqueous solutions

This chapter is based on the following article that I co-authored:

Degoulange D., Dubouis N. and Grimaud A., “Toward the understanding of water-in-salt electrolytes: Individual ion activities and liquid junction potentials in highly concentrated aqueous solutions”, *The Journal of Chemical Physics* **155**, 064701 (2021).

II.A. Introduction

Highly concentrated aqueous solutions have been known to play a key role in biological environment, changing both the thermodynamics and kinetics of biochemical reactions.[112–114] As highlighted in **Chapter I**, highly concentrated aqueous solutions nowadays find an increasing number of applications in electrochemistry, from the long-standing chlor-alkali process, the more recent Water-in-salt (WiSE) Li-ion batteries, all the way to the use of aqueous biphasic systems (ABS). As stated in part **I.A.**, shifting from diluted electrolytes to WiSE is necessary for the design of high voltage aqueous batteries, as it enable the electrochemical window of water to be enlarged from ≈1.5 V to ≈3 V.

Nevertheless, the origin for such enlarged window, it being kinetics or thermodynamics, remains largely debated to date.[31,115,116] Indeed, the lack of knowledge regarding critical physical parameters such as ions activity in these highly concentrated solutions hampers accessing to the reversible potentials for reactions such as the HER. For instance, the activity of protons, equivalent to the pH, has been subject to controversy with reports of acidic pH being measured in highly concentrated solutions while pH was presumed to be neutral as the salts used are not acidic nor basic.[117] Such doubts on the pH and thus on the HER reversible potential are preventing us to estimate the cathodic stability of the electrolyte in this regime. Moreover, when moving from the ideal infinite dilution regime to a highly concentrated one, not only the potential for the HER is modified but the one of other reactions such as Li^+ reversible intercalation as well. Indeed, preliminary studies suggested that when increasing the concentration from a diluted 1m system to a WiSE with 20m of organic Li-salt, namely lithium bis(trifluoromethanesulfonyl)imide (LiTFSI), the reversible potential for cations (de)intercalation shifts positively by ≈200 mV as the result of an increased activity of Li-ions (**Fig. II-1a**).[27]

Hence, from a practical point of view, changes in ions activity are of prime importance. Indeed, if the activity of Li-ions and protons in concentrated solutions evolve differently as a function of salt concentration, lithium intercalation can be favoured in electrode materials such as Mo_6S_8 used in aqueous batteries at the expense of the HER (**Fig. II-1a**), or *vice versa* (**Fig. II-1b**). Such activity shifts would thus directly impact the reactivity at the electrode-electrolyte interface and affect the performances of electrochemical aqueous systems.

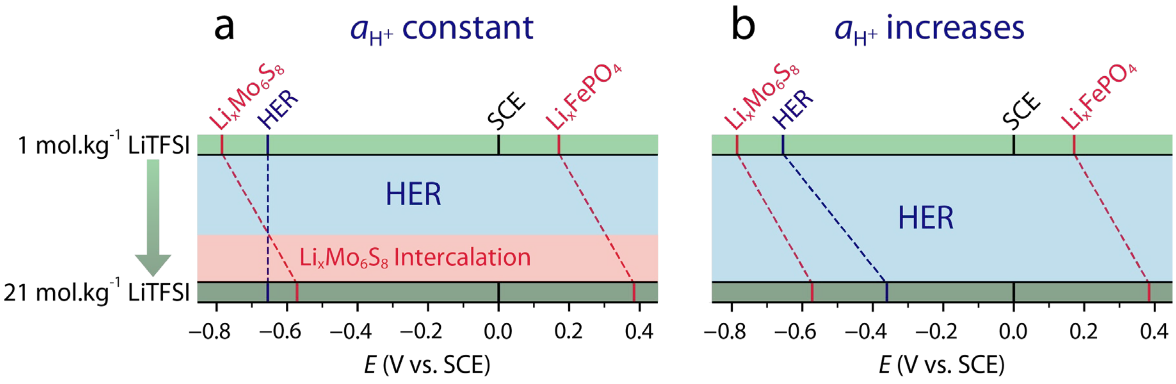

Fig. II-1. Potential shifts for the HER and the Li^+ intercalation in $LiFePO_4$ and Mo_6S_8, from a 1m LiTFSI electrolyte to a 21m LiTFSI WiSE. a, Chemical shifts considering the activity of protons constant, equivalent to a constant pH=7. **b**, Chemical shifts considering an increasing activity of protons, equivalent to a decreasing pH from pH=7 at 1m LiTFSI to pH=2 for 21m LiTFSI.

In solution, the activity of a species S, a_S, is the product of its concentration, c_S, and its activity coefficient, γ_S[118]:

$$a_S = \gamma_S \; c_S \qquad eq.II-1$$

From a fundamental point of view, our current understanding of variations of the activity of species in aqueous systems emerges from complementary theoretical and experimental studies. In very diluted electrolytes, the activity coefficients can be approximated through the Debye and Hückel limiting law:

$$\ln(\gamma_{\text{salt}}) = -A|z_+\ z_-|\sqrt{I} \qquad eq.II-2$$

$$\text{where}\ \ \gamma_{\text{salt}} = \sqrt{\gamma_+\ \gamma_-}\ \ ;\ \ I = \frac{1}{2}\sum\nolimits_{i=\pm} c_i\ z_i^2\ \ ;\ \ A = \frac{e^2 B}{8\pi\varepsilon_0\varepsilon_r k_B T}\ \ ;\ \ B = \sqrt{\frac{2}{\varepsilon_0\varepsilon_r RT}}$$

with γ_{salt} the mean activity coefficient of the salt, γ_+ the cation activity coefficient, γ_- the anion activity coefficient, I the ionic strength, c_i the concentration of ion i, z_i the charge of ion i, e the unit charge, ε_0 the vacuum permittivity, ε_r the relative permittivity of the solvent, k_B the Boltzmann constant, R the gas constant and T the temperature, all given in SI units.[118] In the Debye-Hückel model, the solvent is introduced as a dielectric continuum with a fixed dielectric constant. However, for increased concentrations, the presence of ions is influencing the physical properties of the medium leading to the development of a model with a dielectric constant dependant on ions concentration.[119] Nevertheless, all the above-mentioned models consider the solvent as a dielectric continuum in which solvent-ions interactions are modelled with a Coulomb law between the ions and an average dielectric continuum.[120] While such assumption seems reasonable as long as the ions solvation sphere is kept constant, switching from diluted to highly concentrated aqueous electrolytes the amount of ions-water molecules interactions will decrease, as for a WiSE in which the salt concentration (21m of LiTFSI) corresponds to a stoichiometry of 1:2.6 LiTFSI to water molecules. At such concentration, molecular ion-ion interactions such as ion pairing or bigger ionic aggregates are significantly interfering with the solvation shell of ions[25,121,122,33] but are only poorly modelled via a dielectric continuum. Eventually, equations such as the one developed by Pitzer[123–125] enable the description of ions activity in concentrated electrolytes but are only empirical and do not explain the physics behind any changes in activity coefficients. Consequently, new models are currently being developed to gain a molecular understanding of both solvent-ions and ions-ions interactions and their impact on single ions activity coefficients in highly concentrated electrolytes.[120,126]

Unfortunately, experimental data regarding activity coefficient for ions in highly concentrated solutions pertinent to electrochemical devices are scarce. While the activity of water can be measured using vapour pressure and the mean activity coefficient of a salt determined via osmotic coefficient[127], the activity of individual ions can theoretically be approximated from the Nernst potential of ion selective electrodes (ISE) at equilibrium. Several studies have thus been conducted on individual ions activity in such highly concentrated electrolytes, all pointing towards the increase of ions activity as a function of concentration.[120,126] However, questions remain regarding the validity of such measurements, in part due to difficulties in properly correcting for experimental artefacts such as junction potentials, often completely neglected. Thus, in this work, we discuss our ability to accurately measure single or mean ions activities in highly concentrated electrolytes by the means of electrochemical measurements. For that, we selected two systems, the H_2O-Cl^- one relevant to the chlor-alkali process and the H_2O-$TFSI^-$ one relevant to the battery field. For these systems, Li^+, Zn^{2+} and H^+ cations were studied, giving access to monovalent, divalent and proton chemistries.

II.B. Theory and approximations

First, a redox couple for an oxidising (Ox) and a reducing (Red) agent in solution is considered, with its Nernst potential E_N being described as follow:

$$\mathrm{Ox} + n\,\mathrm{e}^- = \mathrm{Red} \qquad eq.II-3$$

$$E_N = E°_{\mathrm{Ox/Red}} + \frac{RT}{nF}\ln\left(\frac{c_{\mathrm{Ox}}}{c_{\mathrm{Red}}}\right) + \frac{RT}{nF}\ln\left(\frac{\gamma_{\mathrm{Ox}}}{\gamma_{\mathrm{Red}}}\right) \qquad eq.II-4$$

with, F the Faraday constant, $E°_{\mathrm{Ox/Red}}$ the standard potential of the redox couple, c_{Ox} the concentration of the oxidizing agent, c_{Red} the concentration of the reducing agent, γ_{Ox} the activity coefficients of the oxidizing agent and γ_{Red} the activity coefficients of the reducing agent.[39] In this study, three cations have been studied, two monovalent Li^+ and H^+ and a divalent one Zn^{2+}, as well as an anion Cl^-, considering the following Nernst equation and redox equations:

$$x\mathrm{Li^+}_{(\mathrm{aq})} + x\mathrm{e^-} + (1-x)\mathrm{LiFePO_4}_{(\mathrm{s})} + x\mathrm{FePO_4}_{(\mathrm{s})} = \mathrm{LiFePO_4}_{(\mathrm{s})} \qquad eq.II-5$$

$$E_N = E°_{\mathrm{FePO_4/LiFePO_4}} + \frac{RT}{F}\ln\left(a_{\mathrm{Li^+}}(m)\right) \qquad eq.II-6$$

$$2\mathrm{H^+}_{(\mathrm{aq})} + 2\mathrm{e^-} = \mathrm{H_2}_{(\mathrm{g})} \qquad eq.II-7$$

$$E_N = E°_{\mathrm{H^+/H_2}} + \frac{RT}{F}\ln\left(a_{\mathrm{H^+}}(m)\right) \qquad eq.II-8$$

$$\mathrm{Zn^{2+}}_{(\mathrm{aq})} + 2\mathrm{e^-} = \mathrm{Zn}_{(\mathrm{s})} \qquad eq.II-9$$

$$E_N = E°_{\mathrm{Zn^{2+}/Zn}} + \frac{RT}{2F}\ln\left(a_{\mathrm{Zn^{2+}}}(m)\right) \qquad eq.II-10$$

$$\mathrm{AgCl}_{(\mathrm{s})} + \mathrm{e^-} = \mathrm{Ag}_{(\mathrm{s})} + \mathrm{Cl^-}_{(\mathrm{aq})} \qquad eq.II-11$$

$$E_N = E°_{\mathrm{AgCl/Ag}} - \frac{RT}{F}\ln\left(a_{\mathrm{Cl^-}}(m)\right) \qquad eq.II-12$$

$$\mathrm{AgBr}_{(\mathrm{s})} + \mathrm{e^-} = \mathrm{Ag}_{(\mathrm{s})} + \mathrm{Br^-}_{(\mathrm{aq})} \qquad eq.II-13$$

$$E_N = E°_{\mathrm{AgBr/Ag}} - \frac{RT}{F}\ln\left(a_{Br^-}(m)\right) \qquad eq.II-14$$

ISEs used to study Li^+, H^+ and Zn^{2+} were respectively a half lithiated $FePO_4$/$LiFePO_4$ electrode (Li^+-ISE)[128], a reversible hydrogen electrode (RHE) (H^+-ISE) and a metallic Zn electrode (Zn^{2+}-ISE) while a commercial Cl^- selective electrode was used as Cl^--ISE (see details in **S-II: Materials and Methods**).

Experimentally, the accessible quantity is the open circuit voltage (OCV), *i.e.* the difference between the potential of the working electrode (E_{WE}) and the potential of a reference electrode (E_{SCE}), in our case a saturated calomel electrode (SCE). When using an ion-sensitive electrode (ISE), the OCV is dependent on the molality m via the Nernst potential of the redox couple (E_N) as well as the liquid junction potential ($\phi^m - \phi^{SCE}$) arising from the interface between the electrolyte at a molality m with an electric potential ϕ^m and the solution of the reference electrode (SCE) with an electric potential ϕ^{SCE}.[39] Our electrochemical cell (**Fig. II-2d**) and the measured OCV (**Fig. II-2c**) can thus be described as follow:

$$\mathrm{Hg/Hg_2Cl_2/KCl_{sat}/salt}(m)\mathrm{/ISE}$$

$$\mathrm{OCV}(m) = E_{WE}(m) - E_{SCE} = E_N(m) - E_{SCE} + (\phi^m - \phi^{SCE}) \qquad eq.II-15$$

First, we compared the OCV values measured at a molality m using a SCE $(\mathrm{OCV}(m))$ with the OCV measured in a concentration cell (CC) (**Fig. II-2a** and **2b**) between molality m and a molality of reference (m_{Ref}) using no reference electrode $(\mathrm{OCV_{CC}}(m))$, which is given by:

$$\mathrm{ISE/salt}(m_{Ref})\mathrm{/salt}(m)\mathrm{/ISE}$$

$$\mathrm{OCV_{CC}}(m) = E_N(m) - E_N(m_{Ref}) + (\phi^m - \phi^{m_{Ref}}) \qquad eq.II-16$$

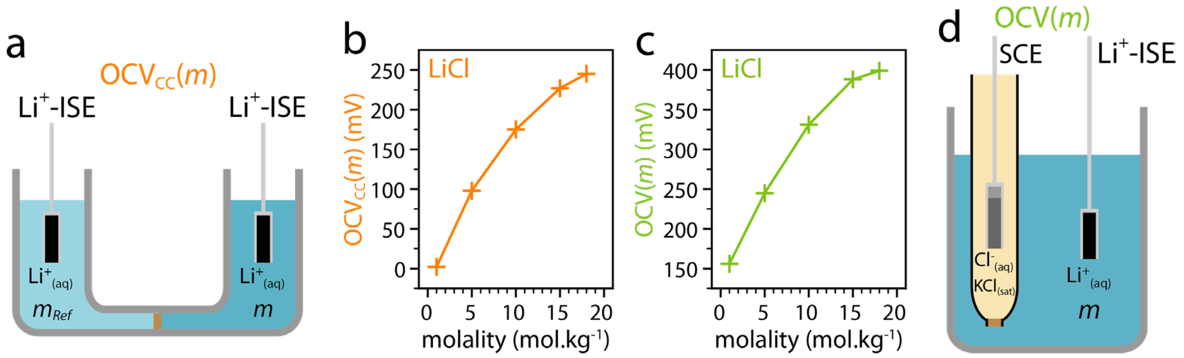

Fig. II-2. OCV values measured from 1m to 18m LiCl. a-b, Scheme representing the measurements with the concentration cell (**a**) and the corresponding OCV values (**b**). **c-d**, Scheme representing the measurements using a SCE reference electrode (**d**) and the corresponding OCV values (**c**).

In a system containing Li$^+$ cations and using a Li$^+$-ISE, the evolution of the OCV values as a function of salt molality are found perfectly similar in both configuration (**Fig. II-2b** and **2c**), thus demonstrating the equivalence between these two configurations (**Fig. II-2a** and **2d**). As a consequence, we establish that the electrode potential of the SCE (E_{SCE}) and the electric potential of the KCl saturated solution of the SCE (ϕ^{SCE}) can be cancelled by taking the difference $\mathrm{OCV}(m) - \mathrm{OCV}(m_{Ref})$ (**Fig. II-3**):

$$\begin{aligned}\mathrm{OCV}(m) - \mathrm{OCV}(m_{Ref}) \\ &= [E_N(m) - E_{SCE} + (\phi^m - \phi^{SCE})] - [E_N(m_{Ref}) - E_{SCE} + (\phi^{m_{Ref}} - \phi^{SCE})] \\ &= E_N(m) - E_N(m_{Ref}) + (\phi^m - \phi^{m_{Ref}}) = \mathrm{OCV_{CC}}(m) \qquad eq.II-17\end{aligned}$$

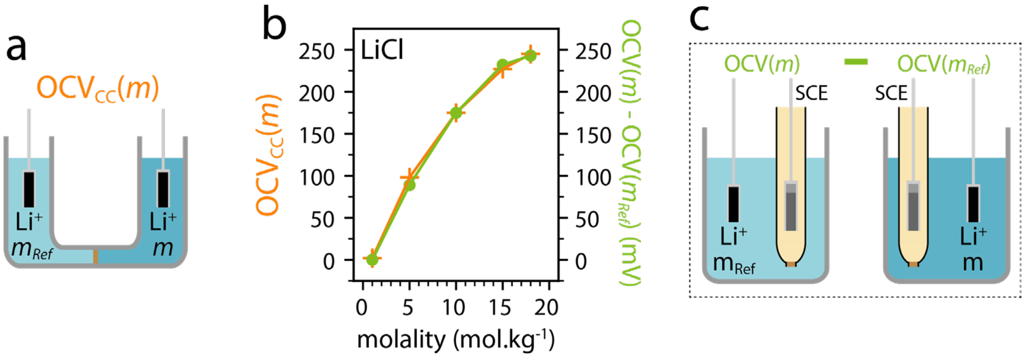

Fig. II-3. Comparison of the concentration cell with the differences of two measurements using a SCE reference electrode from 1m 18m LiCl. a, Scheme representing the measurements with the concentration cell. **b**, Comparison of the OCV values of the concentration cell with the OCV differences measured using a SCE reference electrode from 1m to 18m LiCl. **c**, Scheme representing the difference between two measurements using a SCE reference electrode.

Such result was not evident experimentally-wise regarding the electrical potentials since, as highlighted by Bard and Faulkner,[39] such experiments are strongly dependent on the nature of the physical junction. Hence, hereafter, we fixed the reference concentration to 1m, value which is i) high enough to enable to sum and cancel electrical potentials, ii) widely discussed in previous literature and thus enabling us to compare with our findings[27,129] and iii) low enough not to be considered as being within the "super-concentrated" regime. Moreover, as most of the organic salts used to prepare the electrolytes are very costly, and for the sake of simplicity, the SCE configuration (**Fig. II-3c**) was privileged in the following.

Having demonstrated the equivalence between these two configurations, the difference between $\mathrm{OCV}(m)$ and $\mathrm{OCV}(m_{Ref})$, denoted ΔE in the following, can be split into a Nernstian part (ΔE_N) and a liquid junction part $\left(\Delta E_{LJP}\right)$ and expressed as:

$$\Delta E = \mathrm{OCV}(m) - \mathrm{OCV}\left(m_{Ref}\right) = \Delta E_N + \Delta E_{LJP} \qquad eq.II-18$$

$$\text{with} \quad \Delta E_N = E_N(m) - E_N\left(m_{Ref}\right) \qquad eq.II-19$$

$$\text{and} \quad \Delta E_{LJP} = \left(\phi^{m} - \phi^{m_{Ref}}\right) \qquad eq.II-20$$

The Nernstian part ΔE_N (details for each ISE is given in **S-II: Supplementary Equations** from eq. II-S1 to S25) can be further split into two parts associated with the change of concentration (ΔE_N^c) and the change of activity coefficient $\left(\Delta E_N^{\gamma}\right)$:

$$\Delta E_N = \Delta E_N^c + \Delta E_N^\gamma \qquad eq.II-21$$

$$\Delta E_N^c = \frac{RT}{nF}\ln\left(\frac{c_{\mathrm{Ox}}(m)}{c_{\mathrm{Ox}}(m_{Ref})}\frac{c_{\mathrm{Red}}(m_{Ref})}{c_{\mathrm{Red}}(m)}\right) \qquad eq.II-22$$

$$\Delta E_N^\gamma = \frac{RT}{nF}\ln\left(\frac{\gamma_{\mathrm{Ox}}(m)}{\gamma_{\mathrm{Ox}}(m_{Ref})}\frac{\gamma_{\mathrm{Red}}(m_{Ref})}{\gamma_{\mathrm{Red}}(m)}\right) \qquad eq.II-23$$

Importantly, not only the Nernstian part depends on the activity of individual ions a_i, but the liquid junction potential as well:

$$\Delta E_{LJP} = \frac{-RT}{F}\sum_i \int_{m_{Ref}}^{m} \frac{t_i}{z_i}\,\mathrm{d}\ln a_i \qquad eq.II-24$$

with a_i the activity of the ion i, z_i the charge of the ion i and t_i the transport number of the ion i.[39] Thus, the difference of OCV measured between two different solutions contains three parts, one being dependent on the concentration of the species involved in the redox couple, another one being dependent on their activity coefficient and the third one being dependent on the activity of all the ions in solution:

$$\begin{aligned}\Delta E &= \mathrm{OCV}(m) - \mathrm{OCV}(m_{Ref}) = \Delta E_N^c + \Delta E_N^\gamma + \Delta E_{LJP} \\ &= \frac{RT}{nF}\ln\left(\frac{c_{\mathrm{Ox}}(m)}{c_{\mathrm{Ox}}(m_{Ref})}\frac{c_{\mathrm{Red}}(m_{Ref})}{c_{\mathrm{Red}}(m)}\right) + \frac{RT}{nF}\ln\left(\frac{\gamma_{\mathrm{Ox}}(m)}{\gamma_{\mathrm{Ox}}(m_{Ref})}\frac{\gamma_{\mathrm{Red}}(m_{Ref})}{\gamma_{\mathrm{Red}}(m)}\right) \\ &\quad + \frac{-RT}{F}\sum_i \int_{m_{Ref}}^{m} \frac{t_i}{z_i}\,\mathrm{d}\ln a_i \qquad eq.II-25\end{aligned}$$

Evidently, with this in mind, difficulties in accurately measuring single ion activities of species in solutions can be foreseen, as discussed below.

II.C. Effect of salt molality on the OCV shift for different cations

The OCV values using a Li$^+$-ISE were first measured as a function of LiCl and LiTFSI salt concentration, from diluted to highly concentrated electrolytes. The equilibrium potentials, plotted in **Fig. II-4a**, shifts from ≈150 mV vs SCE in 1m solution to ≈375 mV vs SCE in highly concentrated solutions. In **Fig. II-4b** and **4c** are plotted, respectively for LiCl and LiTFSI, the ΔE

values extrapolated between given molalities m and the reference molality m_{Ref} = 1m. The Nernstian part associated to the change in Li$^+$ concentration ΔE_N^c was calculated and plotted, before to be subtracted from the potential shift to give the corresponding values of $\Delta E - \Delta E_N^c = \Delta E_N^\gamma + \Delta E_{LJP}$. Doing so, $\Delta E - \Delta E_N^c$ values close to each others are obtained for LiCl and LiTFSI (**Fig. II-4b** and **4c**). This observation suggests that the nature of the anion (organic or inorganic) has no drastic impact on the measured shift in potential, despite LiCl and LiTFSI aqueous solutions showing very different solvation structures as well as physical properties.[33]

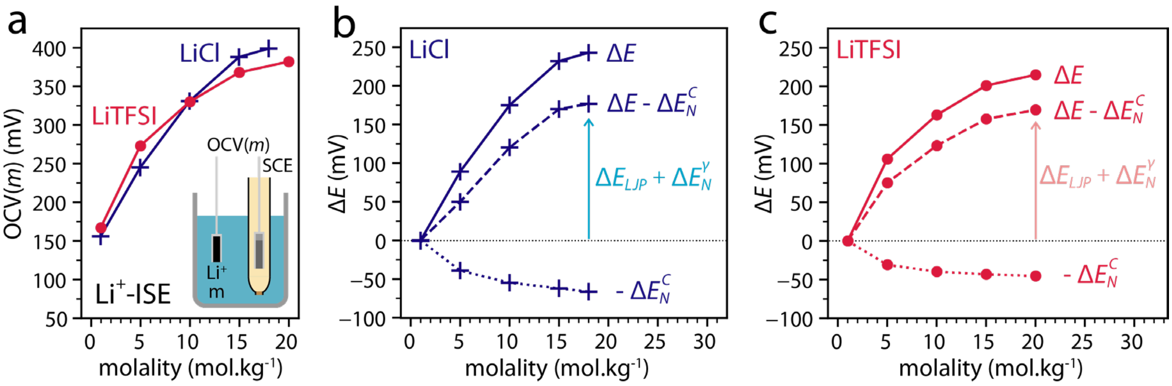

Fig. II-4. Values of $(\Delta E_{LJP} + \Delta E_N^\gamma)$ extracted from the OCV measured with a Li$^+$-ISE in LiCl and LiTFSI solutions. a, OCV values of the ISE-Li$^+$ in LiCl (blue) and LiTFSI (red) solutions. **b-c**, Values of ΔE, calculated values of ΔE_N^C and values of $(\Delta E - \Delta E_N^c)$ for LiCl (**b**) and for LiTFSI (**c**) solutions.

To understand such trend, similar measurements were then performed in Zn^{2+}-containing electrolytes using a Zn^{2+}-ISE. Two cases were considered, one similar to the previous measurement in which the concentration and the molality are simultaneously increased by adding a Zn^{2+}-salt $ZnCl_2$ and a second one in which the concentration of Zn^{2+} is fixed while the overall molality of the solution is increased by increasing the LiTFSI concentration. Doing so, pure $ZnCl_2$ solutions ranging from 1m to 20m were compared to a fixed concentration of 10 mmol.L^{-1} (mM) of Zn(TFSI)$_2$, which solubility is limited in water, dissolved in different LiTFSI solutions. As the concentration of Zn^{2+} at m_{Ref} is 0.87 mol.L^{-1} for $ZnCl_2$ while it is only of 10 mM for Zn(TFSI)$_2$:LiTFSI, a ≈50 mV difference in the absolutes values of OCVs at m_{Ref} is observed (**Fig. II-5a**). Nevertheless, when plotting $\Delta E - \Delta E_N^c$ (**Fig. II-5c**), shifts of ≈250 mV are found from 1m to 20m salt molalities for both $ZnCl_2$ and Zn(TFSI)$_2$:LiTFSI solutions with only a slight deviation being observed at very large concentrations. Surprisingly, this result suggests that the shift in OCV, linked to both the junction potential and the activity coefficient, is independent i) on the concentration of the ion probed, it being the main salt or added in small quantities in a concentrated solution, and ii) on the ion environment which is presumably very different between $ZnCl_2$ and LiTFSI solutions. Even more troubling, the shifts measured as a function of salt molality are close to the ones previously observed for LiTFSI and LiCl solutions using a Li^+-ISE (**Fig. II-4**), despite obvious differences in solvation structures existing between mono- and divalent cations.[33,130]

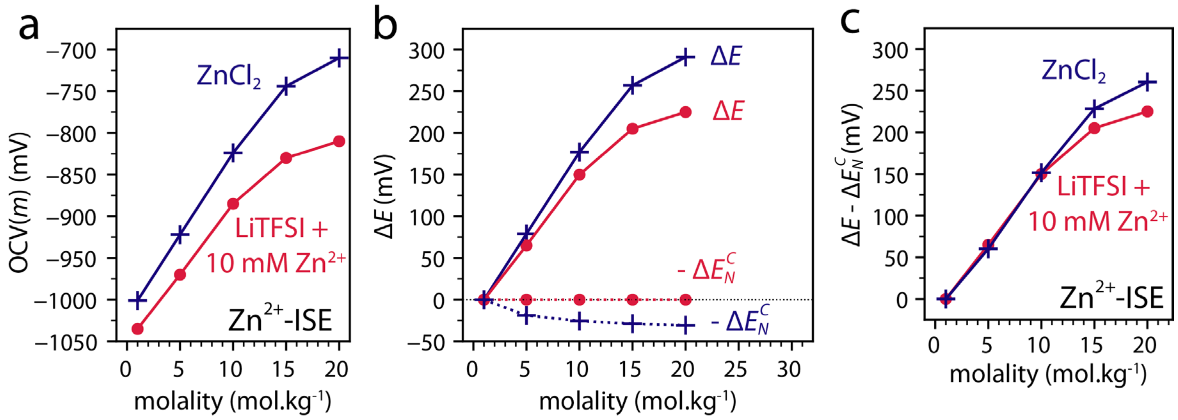

Fig. II-5. Potential shift measured for a Zn^{2+}-ISE as a function of salt molalities. a, OCV values of the Zn^{2+}-ISE in $ZnCl_2$ solutions (blue) and LiTFSI solutions with 10 mM of added $Zn(TFSI)_2$ (red). **b**, Extracted values of ΔE and calculated values of ΔE_N^C in $ZnCl_2$ solutions (blue) and LiTFSI solutions with 10 mM of added $Zn(TFSI)_2$ (red). **c**, $(\Delta \mathrm{E} - \Delta \mathrm{E}_\mathrm{N}^\mathrm{C})$ values of a Zn^{2+}-ISE in $ZnCl_2$ solutions (blue) and $(\Delta \mathrm{E} - \Delta \mathrm{E}_\mathrm{N}^\mathrm{C})$ values of a Zn^{2+}-ISE in LiTFSI solutions with 10 mM of added $Zn(TFSI)_2$ (red).

Startled by this observation, shifts in potential from diluted to highly concentrated LiCl and LiTFSI solutions in which 10 mM of $HClO_4$ is added were measured for a third cation, protons, using a H^+-ISE (**Fig. II-6**). For both series the concentration of protons is fixed to 10 mM by addition of $HClO_4$, thus the concentration term between two given Li-salt concentrations ΔE_N^C is null (**eq. II-S14**). Similar shifts of ≈200 mV are measured from 1m to 15m for both LiCl and LiTFSI solutions with a deviation observed for LiCl near the saturation limit (**Fig. II-6c**).

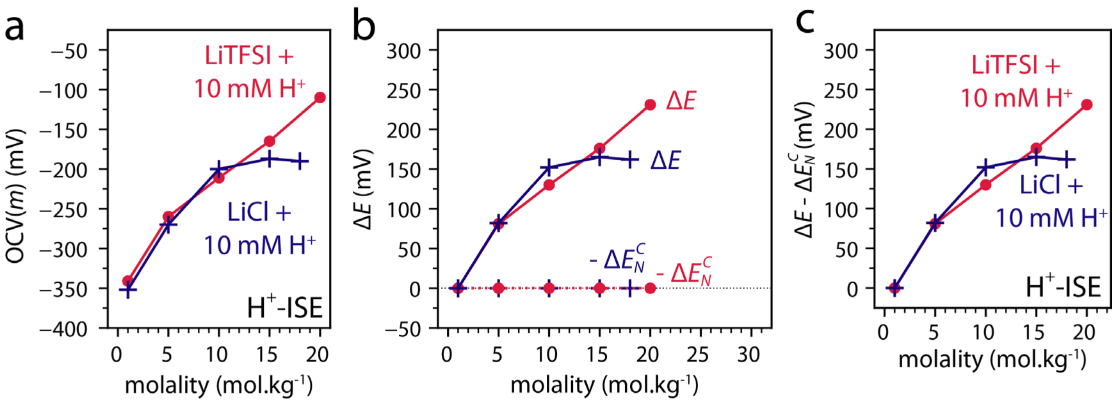

Fig. II-6. Potential shift measured for a H$^+$-ISE as a function of salt molalities. a, OCV values of the H$^+$-ISE in LiCl solutions with 10 mM of added $HClO_4$ (blue) and in LiTFSI solutions with 10 mM of added $HClO_4$ (red). **b**, Extracted values of ΔE and calculated values of ΔE_N^C in LiCl solutions with 10 mM of added $HClO_4$ (blue) and LiTFSI solutions with 10 mM of added $HClO_4$ (red). **c**, $(\Delta E - \Delta E_N^C)$ values of a H$^+$-ISE in LiCl solutions with 10 mM of added $HClO_4$ (blue) and $(\Delta E - \Delta E_N^C)$ values of a H$^+$-ISE in a LiTFSI solution with 10 mM of added $HClO_4$ (red).

Furthermore, when compared to the results previously obtained for Li$^+$ and Zn^{2+}, fairly comparable values for H$^+$ are measured (**Fig. II-7**). These results thus lead to the conclusion that, for either inorganic (Cl$^-$) or organic (TFSI$^-$) anions, the shifts in potential measured for Li$^+$, Zn^{2+} or H$^+$ cations are fairly comparable when subtracting for the concentration term (**Fig. II-7a** and **7b**, respectively). Thus, we demonstrate that neither the nature nor the concentration of the cation or the environment around the cation drastically impacts $\Delta E_N^{\gamma} + \Delta E_{LJP}$, term which is directly accessible by electrochemical means. These observations raise obvious questions, owing to the very different chemistries involved and for which one would expect single ion activity coefficients to drastically differ in all the cases studied in this work.

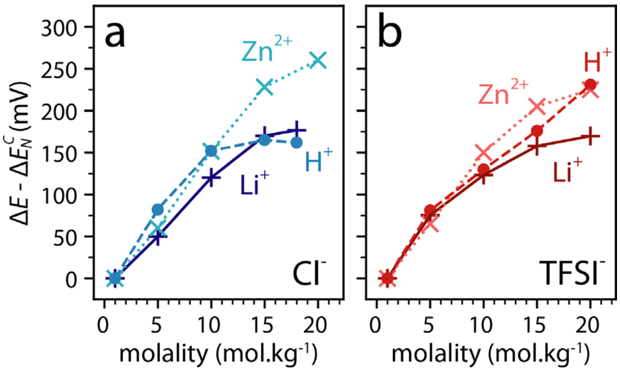

Fig. II-7. $(\mathbf{\Delta E - \Delta E_N^C})$ **values measured with a Li$^+$-ISE compared to that measured with an H$^+$-ISE and a Zn^{2+}-ISE. a**, Comparison of LiCl, LiCl + 10 mM $HClO_4$ and $ZnCl_2$ solutions studied respectively with a Li$^+$-ISE, H$^+$-ISE and Zn^{2+}-ISE. **b**, LiTFSI, LiTFSI + 10 mM $HClO_4$ and LiTFSI + 10 mM $Zn(TFSI)_2$ solutions studied respectively with a Li$^+$-ISE, H$^+$-ISE and Zn^{2+}-ISE.

II.D. Effect of salt molality on the junction potential

To access the shift in potential arising from a change in activity coefficients ΔE_N^{γ}, the junction potential ΔE_{LJP} must be precisely known. Unfortunately, the activity of ions and thus the activity coefficients of individual ions are intrinsically correlated to the liquid junction potential (**eq. II-24**), making the exact determination of junction potentials mathematically irresolvable without approximations.[39] Several approximations were thus previously proposed, one of the most acclaimed ones being the Henderson equation which can be applied to any type of liquid junctions:

$$\Delta E_{LJP} = (\phi^{m} - \phi^{SCE}) - (\phi^{m_{Ref}} - \phi^{SCE})$$

$$= \left(\frac{\sum_i \frac{|z_i|u_i}{zi}\left(c_i(m) - c_i^{SCE}\right)}{\sum_i |z_i| u_i \left(c_i(m) - c_i^{SCE}\right)} \frac{RT}{F} \ln \frac{\sum_i |z_i| u_i \, c_i^{SCE}}{\sum_i |z_i| u_i \, c_i(m)} \right)$$

$$- \left(\frac{\sum_i \frac{|z_i|u_i}{zi}\left(c_i(m_{Ref}) - c_i^{SCE}\right)}{\sum_i |z_i| u_i \left(c_i(m_{Ref}) - c_i^{SCE}\right)} \frac{RT}{F} \ln \frac{\sum_i |z_i| u_i \, c_i^{SCE}}{\sum_i |z_i| u_i \, c_i(m_{Ref})} \right) \qquad eq. II - 26$$

with $c_i(m)$ the concentration of the ion i at molality m, c_i^{SCE} the concentration of the ion i in the KCl_{sat} solution of the SCE, u_{i} the mobility of the ion i in infinitely diluted regimes and z_i the charge of the ion i.[39]

To apply the Henderson equation, two assumptions are made: i) the activities of ions are approximated to be equal to the concentration of ions in solution at each point of the junction and ii) the mobility of ions in solutions is independent of the molality and equal to the mobility measured in infinitely diluted regimes.[39] Doing so, the liquid junction potentials calculated with the Henderson equation are negligible, in the order of few millivolts (**Fig. II-8a**). However, both assumptions regarding the activity and the mobility of ions are certainly not valid in highly concentrated solutions. Indeed, theoretical studies recently pointed out that the activity coefficient largely deviates from unity in highly concentrated regimes[126] while both theoretical and experimental results have shown that diffusion coefficients are greatly dependent on the salt concentration for ions such as Li^+ for instance.[110,131]

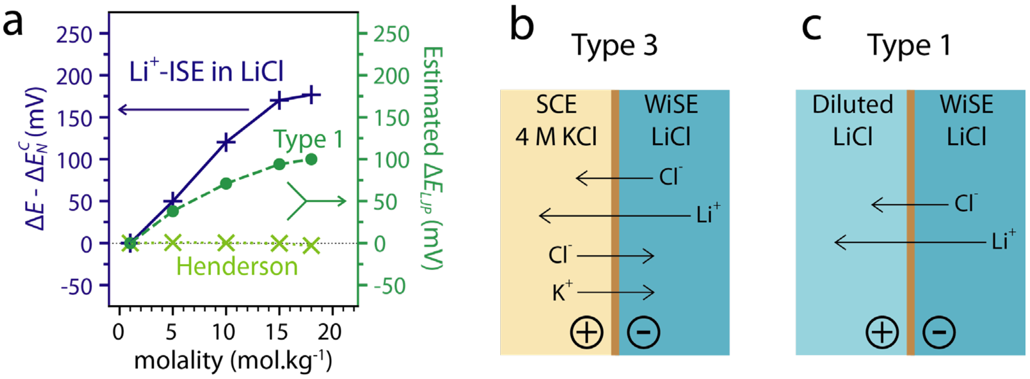

Fig. II-8. Approximations and illustrations of Type 3 and Type 1 liquid junction potential. a, Comparison of $(\Delta\mathrm{E} - \Delta\mathrm{E}_{\mathrm{N}}^{\mathrm{C}})$ values measured with a Li⁺-ISE in LiCl with estimation of the liquid junction potential made using the Henderson equation and Type 1 approximations. **b**, Scheme of a Type 3 liquid junction. **c**, Scheme of a Type 1 liquid junction.

Evidently, measuring the difference in potentials between the solutions considered in this work and a saturated calomel reference electrode, a Type 3 liquid junction potential is formed for which different ions cross the junction in both ways (**Fig. II-8b**) and for which the best approximation is the Henderson equation.[39] Nevertheless, having established earlier the equivalence between our measurements and a concentration cell (**Fig. II-3**), one can tentatively approximate the liquid junction potential to a Type 1 liquid junction potential, *i.e.* a junction between two solutions of common ions but different concentrations and where ions cross the junction to move to the lower concentration (**Fig. II-8c**)[39], which is expressed as:

$$\Delta E_{LJP} = (t_{-} - t_{+})\frac{RT}{F}\ln\left(\frac{\gamma_{\mathrm{salt}}(m)}{\gamma_{\mathrm{salt}}\left(m_{Ref}\right)}\frac{c(m)}{c\left(m_{Ref}\right)}\right) \qquad eq.II - 27$$

with t_{i} the transport number of the ion i, $c(m)$ the concentration of salt at molality m and $\gamma(m)$ the mean activity coefficient of the salt at molality m.[39] Doing so, two assumptions must once again be made: i) the activity of ions are approximated to be equal to the mean activity of the salt given by the product $c(m)\,\gamma(m)$ and ii) transport numbers for cations and anions are considered independent of the molality. Considering LiCl solutions with constant transport numbers ($t_{+} = 0.2$ and $t_{-} = 0.8$)[132] and $\gamma(m)$ values previously reported[127] and summarized in **Table II-1**, non-negligible values ranging between 40 mV and 100 mV are estimated for the Type 1 junction approximation (**Fig. II-8a**). Observing this, one could conclude that the junction potential accounts for a large part of the shift in potential observed in this work as well as in previous studies switching from diluted to highly concentrated solutions.

γ_{salt}	1m	5m	10m	15m	18m
LiCl	0.775	2.000	9.600	30.9	50.3

Table II-1. Mean activity coefficients of LiCl solutions from 1m to 15m. Data from Hamer *et al.*[127].

Nevertheless, the second assumption necessary to apply the Type 1 junction approximation can once again be challenged. Indeed, as previously reported[110,132] and shown in **Fig. II-9**, the transport numbers for both cations and anions do not remain constant across the concentration range studied in this work. Furthermore, mean activity coefficients are used to estimate the junction potentials for a Type 1 junction, rather than single ions activity coefficients theoretically obtained when using ion selective electrodes.

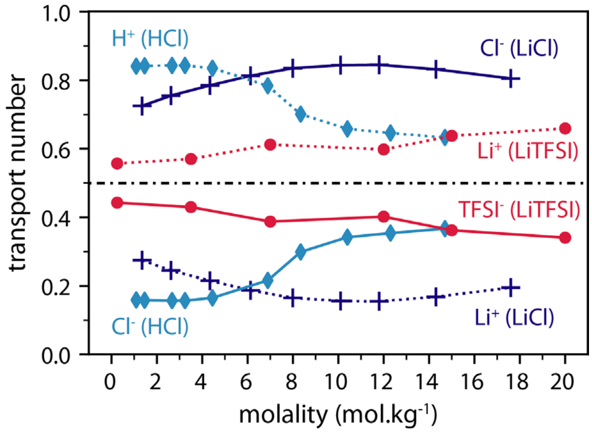

Fig. II-9. Transport numbers for cations (dotted lines) and anions (solid lines) for LiCl (blue), LiTFSI (red) and HCl (cyan). Data from Li *et al.*[110] and Chapman *et al.*[132].

Overall, and similarly to the activity of ions, no good approximation currently exists for treating the junction potential in such highly concentrated solutions. Despite such limitations, one can suggest that values close to or greater than 100 mV are found when forming a junction between a 1m solution and a highly concentrated solutions. Such conclusion is further re-enforced by observing that very similar potential shifts are measured for three very different chemistries – a monovalent alkali-cation Li^+, a divalent transition metal Zn^{2+} and protons – both when the cations studied is diluted in a highly concentrated environment, such as for Zn^{2+} and protons in LiTFSI, and when the cations of interest are the main cation forming the highly concentrated solutions, as for Li^+ in LiTFSI solution or Zn^{2+} in $ZnCl_2$. A common pitfall would thus be to completely neglect the junction potential when studying shift in redox potentials in highly concentrated solutions, or to use a glass electrode pH-meter as previously done to estimate the pH in LiTFSI solutions as a function of salt molality.[39] We should rather conclude that, using electrochemical cells in which a liquid junction is formed, the activity coefficients and thus the activity of ions can hardly be extracted in highly concentrated solutions owing to a very large junction potential. This conclusion holds true when using a reference electrode alike the SCE used in this work, as well as when building its equivalent concentration cell (**Fig. II-3**).

To be free of any junction potential, potentials can be measured between two ISEs, one being selective to the cation (Li^+) and the other one to the anion (Cl^- for instance), in the same solution to avoid inducing a junction potential:

$$\mathrm{Li^+ - ISE\ /LiCl}(m)/\ \mathrm{Cl^- - ISE}$$

$$\mathrm{OCV}(m) = E°_{\mathrm{Li^+-ISE}} - E°_{\mathrm{Cl^- -ISE}} + \frac{2RT}{F}\ \ln\big(c(m)\big) + \frac{2RT}{F}\ \ln\left(\sqrt{\gamma_{\mathrm{Li^+}}(m)\ \gamma_{\mathrm{Cl^-}}(m)}\right) \qquad eq.II-28$$

While being experimentally convenient, such measurement only gives access to the mean activity coefficients of ions defined as follow:

$$\gamma_{\mathrm{LiCl}}(m) = \sqrt{\gamma_{\mathrm{Li^+}}(m)\ \gamma_{\mathrm{Cl^-}}(m)} \qquad eq.II-29$$

and which are commonly obtained by osmotic measurements.[133] Hence, in **Fig. II-10**, the activity of Cl^- was studied using a Cl^--ISE in LiCl solutions.

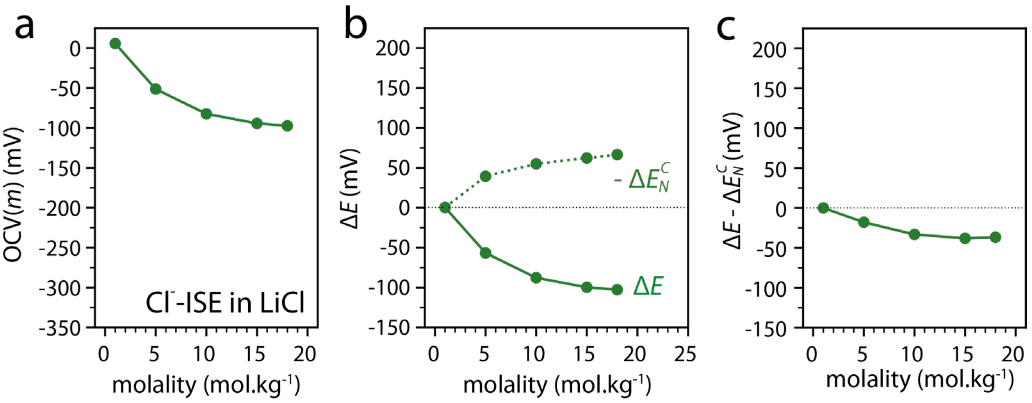

Fig. II-10. Potential shift measured for a Cl^--ISE as function of LiCl molality. a, OCV values in LiCl solutions against a SCE reference electrode. **b**, Extracted values of ΔE and calculated values of ΔE_N^C. **c**, $(\Delta E - \Delta E_N^c)$ values in LiCl solutions.

In **Fig. II-11b** are plotted the $(\Delta E - \Delta E_N^c)$ values for the Cl$^-$-ISE and Li$^+$-ISE measured independently against a SCE reference electrode, and their difference is reported in **Fig. II-11c**. The difference between the Cl$^-$-ISE and Li$^+$-ISE measured independently against a SCE (configuration a1 in **Fig. II-11a**) provides similar values that those obtained in a single solution (configuration a2 in **Fig. II-11a**), thus confirming that the electrode potential of the SCE (E_{SCE}) and the electric potential of the KCl saturated solution of the SCE (ϕ^{SCE}) can be cancelled, as previously stated in **eq. II-17**. Moreover, in configuration a1 (**Fig. II-11a**), the electrical potential of the LiCl solution at molality m (ϕ^m) is also expected to cancel, the liquid junction potentials is thus completely cancelled as following:

$$
\begin{aligned}
(\Delta E - \Delta E_N^c)_{\mathrm{Li^+}} - (\Delta E - \Delta E_N^c)_{\mathrm{Cl^-}} &= \left[\Delta E_{LJP} + \Delta E_N^\gamma(\mathrm{Li^+})\right] - \left[\Delta E_{LJP} + \Delta E_N^\gamma(\mathrm{Cl^-})\right] \\
&= \left[(\phi^m - \phi^{SCE}) - (\phi^{m_{Ref}} - \phi^{SCE}) + \Delta E_N^\gamma(\mathrm{Li^+})\right] \\
&\quad - \left[(\phi^m - \phi^{SCE}) - (\phi^{m_{Ref}} - \phi^{SCE}) + \Delta E_N^\gamma(\mathrm{Cl^-})\right] \\
&= \left[(\phi^m - \phi^{m_{Ref}}) + \Delta E_N^\gamma(\mathrm{Li^+})\right] - \left[(\phi^m - \phi^{m_{Ref}}) + \Delta E_N^\gamma(\mathrm{Cl^-})\right] \\
&= \Delta E_N^\gamma(\mathrm{Li^+}) - \Delta E_N^\gamma(\mathrm{Cl^-}) \qquad eq.II-30
\end{aligned}
$$

We therefore demonstrate with these measurements that configurations a1 and a2 (**Fig. II-11a**) are equivalent. Moreover, the results of both configurations overlap with the potential shifts calculated with the following equation and using the average activity coefficients for LiCl solution already reported[16]:

$$
\Delta E_N^\gamma(\mathrm{Li^+}) - \Delta E_N^\gamma(\mathrm{Cl^-}) = \frac{2RT}{F}\ln\left(\frac{\gamma_{\mathrm{LiCl}}(m)}{\gamma_{\mathrm{LiCl}}(m_{Ref})}\right) \qquad eq.II-31
$$

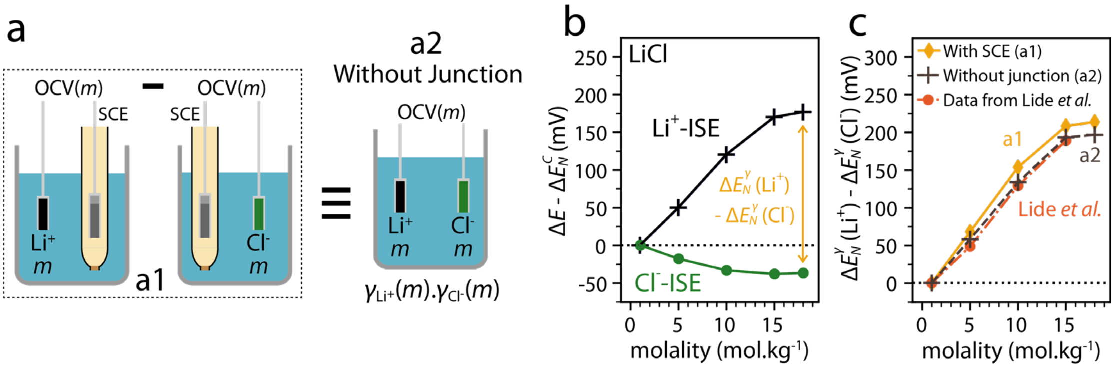

Fig. II-11. Schemes and comparison of the cell configurations with or without liquid junction. a, Cell without liquid junction using a Li$^+$-ISE and a Cl$^-$-ISE (**a2**) and the equivalent configuration using an SCE (**a1**). **b**, Potential of the Li$^+$-ISE and a Cl$^-$-ISE in the a1 configuration. **c**, Comparison between the calculated shift from Lide *et al.*[16] with the potential shifts in the a1 and a2 configurations.

Overall, we demonstrate that electrochemical measurements can reliably provide mean activity coefficients, using two different configurations. Even though mean activity coefficients are useful for certain applications, activity coefficients of single ions are the values of interest to comprehend interfacial redox reactions relevant to electrochemical devices. Unfortunately, they cannot be extrapolated directly from mean activity coefficients. To measure single ion activity coefficient free of any liquid junction potential, quasi-reference electrode such as a Platinum wire calibrated via an internal reference such as the Ferrocenium/Ferrocene couple (Fc^+/Fc) could be used.[39] However, doing so the OCV is then expressed as the product of the activities coefficients between the two redox couples:

$$\mathrm{Li^+-ISE\ /LiCl}(m)/\mathrm{Pt}$$

$$\mathrm{OCV}(m) = E°_{\mathrm{Li^+-ISE}} - E°_{\mathrm{Fc^+/Fc}} + \frac{RT}{F}\ln\left(c_{\mathrm{Li^+}}(m)\right) + \frac{RT}{F}\ln\left(\frac{\gamma_{\mathrm{Li^+}}(m)\,\gamma_{\mathrm{Fc}}(m)}{\gamma_{\mathrm{Fc^+}}(m)}\right) \qquad eq.II-32$$

Hence, such measurement gives access to the product of activity coefficients, alike the combined Li^+-ISE and Cl^--ISE discussed above (**eq. II-28**). To access single ion activity coefficients for Li^+ $\left(\gamma_{\mathrm{Li^+}}(m)\right)$ in such configuration, the following must be met: $\gamma_{\mathrm{Fc}}(m) = \gamma_{\mathrm{Fc^+}}(m)$, implying that the formal potential of the Ferrocenium/Ferrocene couple is independent on the solution. However, this assumption seems fallacious since the formal potential of Ferrocenium/Ferrocene redox couple is modified by both the nature and the concentration of the salt.[134] Combined with the low solubility of Ferrocene in aqueous solutions (≈10^{-5} mol.L^{-1}),[135] its use or the use of any other ferrocene derivatives as a proper internal reference should thus be considered with extreme care. Similarly, the use of non-electrochemical means such as molecular probes or pH paper[136] does not lead to the formation of a liquid junction. However, once again, this approach only gives access to a product of activity coefficients between the molecular probes and the ion of interest.

II.E. Effect of the salt molality on proton concentration

Finally, despite difficulties in extracting the activity for single ions using electrochemical methods, such approach reveals useful to probe changes in concentration of ions in solution. Indeed, while 10 mM of $HClO_4$ was added in the previous experiments to fix the concentration of protons, we demonstrate that in the absence of added $HClO_4$, protons concentration is increased from diluted to highly concentrated aqueous solutions.

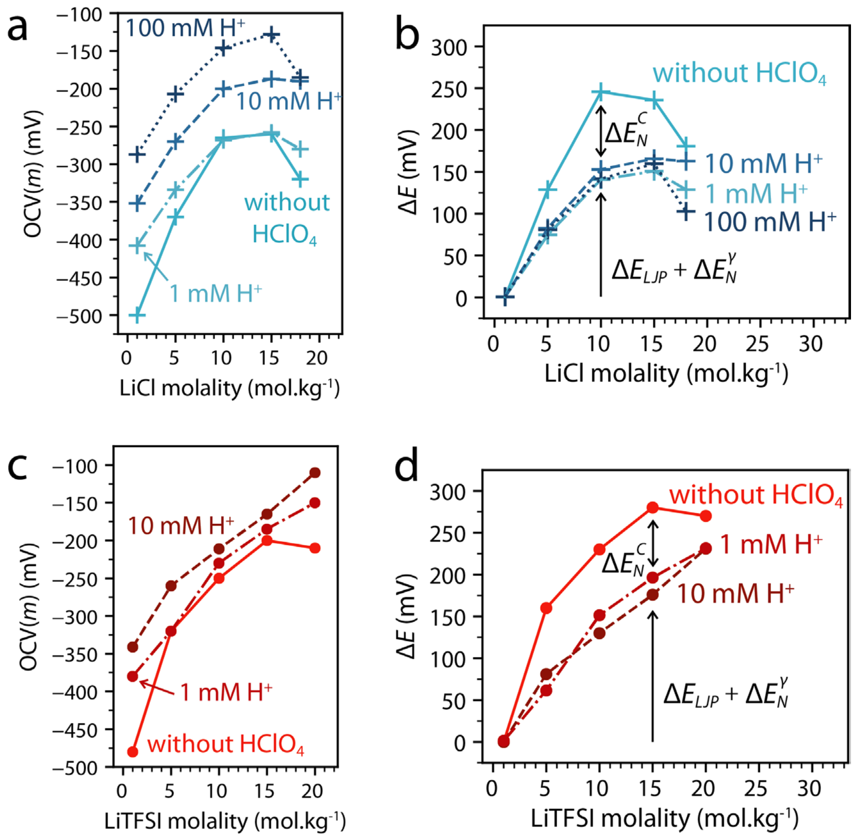

Fig. II-12. Potential shifts in highly concentrated LiCl and LiTFSI solutions via the use of a H^+-ISE against a SCE reference electrode. a-b, OCV (**a**) and ΔE (**b**) values of the H^+-ISE in LiCl solutions with 1mM, 10mM, 100mM or without added $HClO_4$. **c-d**, OCV (**c**) and ΔE (**d**) values of the H^+-ISE in LiTFSI solution with 1 mM, 10mM or without added $HClO_4$.

For that, we first compared the OCV and ΔE values measured with 1 mM, 10 mM and 100 mM added protons ($HClO_4$) in LiCl and 1 mM and 10 mM added protons ($HClO_4$) in LiTFSI electrolytes using H^+-ISE (**Fig. II-12**) (due to solubility issues, the measurements with 100 mM of added protons in LiTFSI electrolytes could not be performed across the whole molality range). For ΔE values (**Fig. II-12b** and **2d**) when protons are added, aside from the shift of ≈150 mV measured from 1m to highly concentrated solutions discussed previously, no significant changes are observed between 1 mM, 10 mM and 100 mM of added protons for LiCl or between 1 mM and 10 mM of added protons in LiTFSI. One can thus estimate that the proton concentration is fixed by the addition of $HClO_4$. Thus, the ΔE_N^c term is null and $\Delta E = \Delta E_N^\gamma + \Delta E_{LJP}$, with $\Delta E_N^\gamma + \Delta E_{LJP}$ independent on the addition of $HClO_4$. This experimental result is rationalized as both the proton activity coefficients and the junction potentials are not expected to drastically change with the addition of small quantities of $HClO_4$ relative to the lithium salt molality. This conclusion is further confirmed by the similar values of $\Delta E - \Delta E_N^c$ obtained with and without added $HClO_4$ using the Li^+-ISE (**Fig. II-13**).

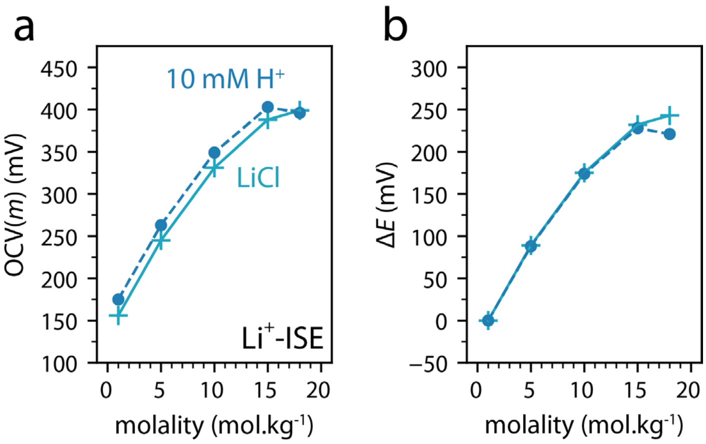

Fig. II-13. Comparison of the results between a Li^+-ISE in LiCl solutions with or without added 10 mM of $HClO_4$. a, OCV values of the Li^+-ISE from LiCl solutions (cyan) and LiCl solutions with 10 mM of added $HClO_4$ (blue). **b**, Extracted values of ΔE in LiCl solutions (cyan) and LiCl with 10 mM of added $HClO_4$ (blue).

Building upon this result, potentials measured with and without added $HClO_4$ were then compared for LiCl and LiTFSI solutions (**Fig. II-12b** and **2d**, respectively). Doing so, without added protons, an additional shift of ≈100 mV is observed compared to the ΔE values obtained with added protons. It is to be noted that, without the addition of protons and especially at low salt concentration, LiCl and LiTFSI electrolytes are unbuffered media and thus OCV values could vary of a few dozen millivolts rendering any quantitative analysis difficult. However, as previously discussed, $\Delta E = \Delta E_N^\gamma + \Delta E_{LJP}$ with added protons, thus this additional shift originates from a change in the concentration part of the Nernstian potential ΔE_N^c as a function of salt concentration when no protons are added. Thus, to account for the additional ≈100 mV shift in potential, an increase from one to two orders of magnitude of the proton concentration going from diluted to highly concentrated LiCl and LiTFSI solutions must be invoked.

In definitive, we confirm that WiSE are more acidic than classical diluted solutions. Nevertheless, as the addition of 1 mM of $HClO_4$ in WiSEs is sufficient to fix the concentration of protons (*i.e.* no difference is found between 1, 10 and 100 mM added protons), one can conclude that the concentration of protons in WiSEs is lower than 10^{-3} mol.L^{-1}. Hence, the shift from pH 7 to pH 2 (corresponding to a shift of about 300 mV) previously reported using a glass pH-meter does not reflect a change in concentration by 5 orders of magnitude of the proton concentration. Moreover, it certainly does not mean that the concentration of protons is equal to 10^{-2} mol.L^{-1} (pH 2 in a diluted regime) in highly concentrated aqueous electrolytes. Hence, adopting this electrochemical approach, we highlight that any shift in reversible potential measured with a protons selective electrode in WiSEs should not be discussed with regard to a change of pH, often implicitly understood as a change of proton concentration, but rather be discussed with regards to a change in activity of protons. Furthermore, while we confirm that the activity of protons is increased in WiSEs compared to diluted solutions, this increase originates from both a change in concentration and a change in activity coefficient. Finally, as demonstrated above, an increase of the liquid junction potential contributes to a non-negligible portion of the measured shift in potential and must be considered for any activity measurement in highly concentrated solutions. Unfortunately, this prevents us from gaining quantitative values for activity coefficients in highly concentrated solutions as they are correlated with the junction potential.

II.F. Chapter Conclusions

In conclusion, we have established that shift in redox potentials as a function of salt concentration from diluted to highly concentrated regimes measured using ion selective electrodes originates in large from an increased junction potential. This is not to say that the activity coefficients of single ions do not increase as a function of salt concentration, as it certainly does, but that such increase cannot be captured by a simple electrochemical method in which a liquid/liquid junction is formed. Such limitation is nested in the dependence of the junction potential on the activity of ions. Furthermore, while electrochemical methods exist to avoid the formation of such junction, they only allow for accessing the mean activity coefficients, alike the ones obtained by osmotic pressure measurements.

While unfortunate for a broad range of fields from bio-electrochemistry to batteries, such conclusion renders futile the search for any electrochemical means to extract activities and/or activity coefficients for individual ions, even though such data is cruelly lacking to validate recent theoretical studies.[126] Nevertheless, the comparison of potential shifts for a fixed junction potential enable to partially avoid this issue. Doing so, we could demonstrate that protons are indeed created when switching from a diluted to a highly concentrated aqueous electrolytes. Even though quantitative values cannot be estimated, in part owing to the limited stability of these solutions[136], our results suggest that the proton concentration changes by almost two orders of magnitude from 1m to 18m for LiCl or 20m for LiTFSI solutions. Finally, this effect will add to the increased activity coefficient for protons and shift the HER towards more positive potentials, counter-balancing the shift towards more positive potentials expected for Li^+-based intercalation processes when increasing the Li-salt concentration (**Fig. II-1b**). Thus, for practical applications, the use of highly concentrated Li-based electrolytes does not prevent water reduction, from a thermodynamics point of view, which correlates with previous self-discharge experiments for WiSE batteries.[31] However, the increased activity coefficient for Li^+ does displace the solubility equilibrium for solid electrolyte interphase (SEI) inorganic components such as LiF,[137] and thus slows down interfacial reactivity. Similarly, such shifts in activity coefficients explain the limited solubility of transition metal halides in superconcentrated electrolytes that were recently uncovered as novel Li^+-intercalation compounds.[138] Overall, such study highlights the difficulties in accurately measuring physical properties of prime importance for assessing the competition existing at the electrode/electrolyte interface both at the negative electrode, as highlighted in this chapter, as well as at the positive electrode as we will see in the next chapter.

Chapter III – Halogen intercalation into graphite using ABS

This chapter is based on the following article that I co-authored:

Degoulange D., Rousse G. and Grimaud A., “Two-Step Mechanism for Halogen Intercalation in Graphite Enabled by Aqueous Biphasic Systems”, *ACS Energy Letters* **8**, 4397-4405 (2023)

III.A. Introduction

As stated in **Chapter I**, beside their interest for separation or recycling, ABS recently showed interest for battery applications, enabling the use of distinct aqueous electrolytes and thus distinct chemistries at the positive and at the negative electrodes. This is made possible by the formation of a liquid/liquid interface selective to dissolved ionic species, thus preventing cross-talking events in lithium-sulfur or redox-flow batteries.[76,78] As presented in **Chapter I**, Yang *et al.*[7] used an ABS based on LiTFSI, LiCl and LiBr to design a so called “dual-ion" battery relying on the reversible intercalation of lithium cations from the TFSI-rich phase at the negative electrode and the reversible conversion/intercalation of halide anions from the halide-rich phase into graphite at the positive electrode (**Fig. III-1a**). This halide conversion/intercalation mechanism enables a transition metal free aqueous battery with a reversible capacity of 243 $mAh.g^{-1}$, for > 200 cycles with 80% capacity retention at 200 $mA.g^{-1}_{graphite}$.

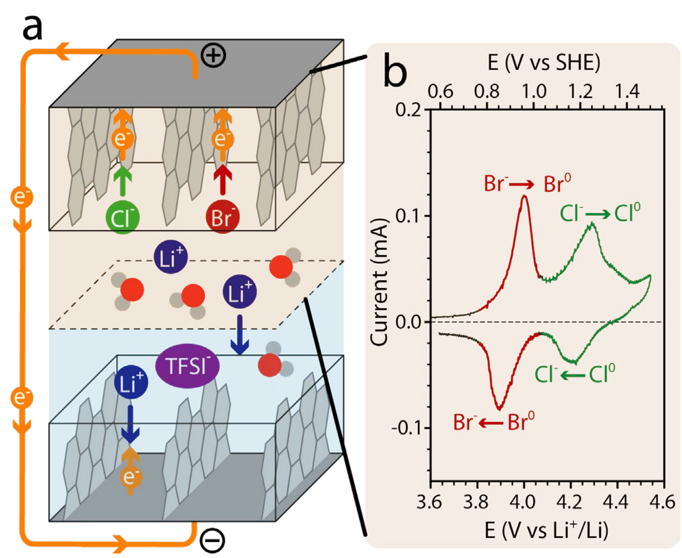

Fig. III-1. Schematics and cyclic voltammogram of the aqueous battery using ABS forming at high concentration. a, Schematics of a battery based on halogen conversion/intercalation at the positive electrode and Li-ion intercalation at the negative electrode, using an ABS as electrolyte having a TFSI-rich phase in contact with the negative electrode and a halide-rich phase in contact with the positive electrode. **b**, Three-electrodes cycling voltammetry recorded for the intercalation of halides into graphite, with first the intercalation of bromide (red) then followed by the intercalation of chloride (green).

Halogens conversion/intercalation into graphite was reported to occur at high potentials, following two sequential reactions (**eq. III-1**): first bromide (Br^-) is intercalated at 3.95 V vs. Li^+/Li to form $C_6[Br_2]$ followed by chloride (Cl^-) intercalation at 4.25 V vs. Li^+/Li to form $C_6[BrCl]$ (**Fig. III-1b**). Both reactions are associated with the oxidation of halide anions, but differ from direct halides oxidation into either halogen gases (**eq. III-2**) or soluble polyhalides (**eq. III-3**).

$$2X^-{}_{(sol)} + C_{6\,(s)} = C_6[X_2]_{(s)} + 2e^- \quad (X = Br, Cl) \qquad eq.\,\mathrm{III}-1$$

$$2X^-{}_{(sol)} = X_{2\,(g)} + 2e^- \quad (X = Br, Cl) \qquad eq.\,\mathrm{III}-2$$

$$3X^-{}_{(sol)} = X_3{}^-{}_{(sol)} + 2e^- \quad (X = Br, Cl) \qquad eq.\,\mathrm{III}-3$$

While X-ray diffraction and X-ray absorption measurements have revealed this conversion/intercalation of halides into graphite[7], the exact role played by the ABS in enabling the intercalation of halogens while preventing competing oxidative reactions remains elusive. More precisely, past studies and **Chapter II** have revealed effects of high salt concentrations[25,27,139] on redox potentials for reactions involving cations such as Li^+, H^+ or Zn^{2+}, but our current understanding of concentration-dependence of anions redox is still limited.[140–

[142] Furthermore, ABS are known for their ability to partition ions, more precisely anions, as previously demonstrated for TFSI$^-$ [33,107,143,7,139] or for soluble polysulfides[76]. Nevertheless, very little is known regarding solvation properties and speciation of halide anions in ABS. Developing further multiphasic (ABS) electrolytes for dual-ion, lithium-sulfur, redox flow or beyond Li-ion battery technologies thus relies on gaining a deeper understanding of the role played by ABS. Hence, we studied the effect of ABS high salt concentrations and liquid/liquid interface in i) modulating redox potentials for halide oxidation and ii) changing the chemical nature and solvation properties of soluble halides in each aqueous phase.

III.B. Trihalides formation

The main difficulty in assessing the redox potentials for Br$^-$ oxidation (or Cl$^-$ oxidation, see below) originates from the co-existence of three reactions (**eqs. III-4, III-6, III-8**), depending on Br$^-$ concentration and pH, following Nernst potentials (**eqs. III-5, III-7, III-9**):

$$Br_{2(aq)} + 2e^- = 2Br^-{}_{(aq)} \qquad eq.\mathrm{III}-4$$

$$E = E°_{Br_2/Br^-} + \frac{RT}{2F} ln\left(\frac{a\left(Br_{2(aq)}\right)}{a\left(Br^-{}_{(aq)}\right)^2}\right) \qquad eq.\mathrm{III}-5$$

$$Br_3{}^-{}_{(aq)} + 2e^- = 3Br^-{}_{(aq)} \qquad eq.\mathrm{III}-6$$

$$E = E°_{Br_3{}^-/Br^-} + \frac{RT}{2F} ln\left(\frac{a\left(Br_3{}^-{}_{(aq)}\right)}{a\left(Br^-{}_{(aq)}\right)^3}\right) \qquad eq.\mathrm{III}-7$$

$$BrO_3{}^-{}_{(aq)} + 6H^+{}_{(aq)} + 6e^- = Br^-{}_{(aq)} + 3H_2O_{(l)} \qquad eq.\mathrm{III}-8$$

$$E = E°_{BrO_3{}^-/Br^-} + \frac{RT}{6F} ln\left(\frac{a\left(BrO_3{}^-{}_{(aq)}\right).a\left(H^+{}_{(aq)}\right)^6}{a\left(Br^-{}_{(aq)}\right).\ a\left(H_2O_{(l)}\right)^3}\right) \qquad eq.\mathrm{III}-9$$

with $E°$ the standard potentials, R the molar gas constant, T the temperature, F the Faraday constant, $a\left(H_2O_{(l)}\right)$ the water activity (see details in **S-III: Supplementary Discussion**)[144] and $a\left(X^-{}_{(aq)}\right)$ the activities of the different ions linked to the concentrations, $c\left(X^-{}_{(aq)}\right)$, and activity coefficients, $\gamma\left(X^-{}_{(aq)}\right)$, of the different ions with $a\left(X^-{}_{(aq)}\right) = c\left(X^-{}_{(aq)}\right).\gamma\left(X^-{}_{(aq)}\right)$.

Calculating the Pourbaix diagram (E = f(pH)) for the bromide-water system[145] as function of Br^- concentration (see details in **S-III: Materials and Methods**), a three-dimensional Pourbaix diagram is obtained (**Fig. III-2**). For pH above 7, Br^- oxidation to bromate (BrO_3^-) is thermodynamically favoured at all concentrations. However, for pH below 7, two oxidation products can exist depending on the Br^- concentration. At concentrations below 0.1m, Br^- is oxidized to bromine (Br_2). Instead, at concentration above 0.1m, Br^- is oxidized to tribromide (Br_3^-). As previously demonstrated (**Chapter II**), highly concentrated aqueous solutions are slightly acidic[117,139], hence oxidation of Br^- to Br_3^- is thermodynamically favoured in conditions pertinent to ABS.

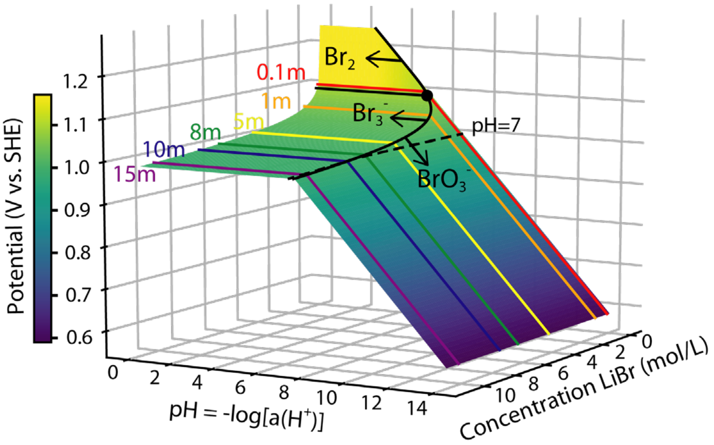

Fig. III-2. Three-dimensional graph obtained by plotting the Pourbaix diagram of bromide (E = f(pH)) as function of the lithium bromide concentration.

Knowing that Br_3^- is the thermodynamically favored oxidation product at high concentration, a cubic dependence of Br^- oxidation potential on LiBr concentration is expected following **eq. III-7** and $a(X^-{}_{(aq)}) = c(X^-{}_{(aq)}).\gamma(X^-{}_{(aq)})$. Hence, we studied the Br^- oxidation by cyclic voltammetry (CV) on glassy carbon rotating disk electrodes (GC-RDE) in electrolytes containing lithium Br^- in concentration ranging from 0.1m to 15m (**Fig. III-3a**). Increasing the concentration was found to shift the oxidation toward less positive potentials (**Fig. III-3a**), from 1.05 V vs the standard hydrogen electrode (SHE) at 0.1m to 0.85 V vs SHE at 15m.

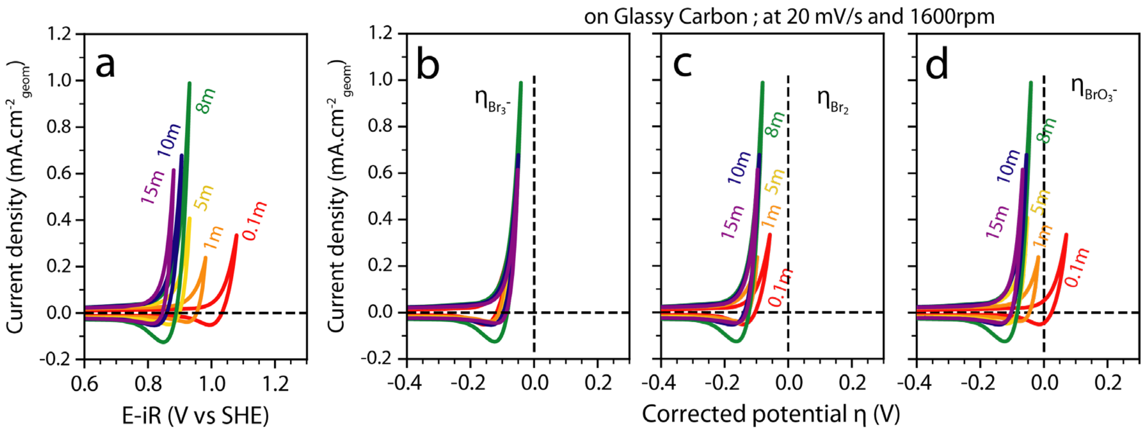

Fig. III-3. Halogens oxidation in highly concentrated LiBr solutions. a, Cyclic voltammograms of the bromide oxidation recorded on Glassy Carbon rotating disk electrodes at 1600 rpm for LiBr solutions of concentration between 0.1m and 15m plotted as function of the ohmic drop compensated potential. **b-d**, Cyclic voltammograms described in (**a**) with potentials corrected for the oxidation of bromide to tribromide (**b**), bromine (**c**) or bromate assuming pH=7 in Nernst equation (**d**).

As the reversible potential of Br^-/Br_3^- has a cubic dependence on Br^- concentration ($-\frac{RT}{2F}ln\left(c\left(Br^{-}{}_{(aq)}\right)^{3}\right)$), potentials were converted into Br_3^- corrected potential ($\eta_{Br_3^-}$) (**eq. III-10**, derived from **eq. III-7**) by taking into consideration such cubic Br^- concentration dependence. Alternatively, potentials can be converted to Br_2 or BrO_3^- corrected potential (η_{Br_2} or $\eta_{BrO_3^-}$) (**eq. III-11** or **eq. III-12**, both derived from **eq. III-5** and **eq. III-9**) by taking into consideration, respectively, a square or linear Br^- concentration dependence as well as the pH dependence of **eq. III-9**. Potentials are corrected for the liquid junction potential (LJP) and potential shift due to ions' activity coefficient as estimated in **Fig. III-S1** following the procedure established in **Chapter II** by calculating values of $\Delta E - \Delta E_N^c = \Delta E_N^\gamma + \Delta E_{LJP}$, simply written $E_{LJP/\gamma}$ in the following.

$$\eta_{Br_3^-} = E - \left(E°_{Br_3^-/Br^-} - \frac{RT}{2F} ln\left(c\left(Br^{-}{}_{(aq)}\right)^{3}\right)\right) - iR - E_{LJP/\gamma} \qquad eq. \text{III} - 10$$

$$\eta_{Br_2} = E - \left(E°_{Br_2/Br^-} - \frac{RT}{2F} ln\left(c\left(Br^{-}{}_{(aq)}\right)^{2}\right)\right) - iR - E_{LJP/\gamma} \qquad eq. \text{III} - 11$$

$$\eta_{BrO_3^-} = E - \left(E°_{BrO_3^-/Br^-} - \frac{RT}{6F} ln\left(c\left(Br^{-}{}_{(aq)}\right)\right) + \frac{RT}{F} ln\left(a\left(H^{+}{}_{(aq)}\right)\right)\right) \\ -iR - E_{LJP/\gamma} \qquad eq. \text{III} - 12$$

After conversion, CVs recorded do not overlap at all concentrations for η_{Br_2} (**Fig. III-3c**) nor for $\eta_{BrO_3^-}$ (**Fig. III-3d**). However, all concentrations overlap for $\eta_{Br_3^-}$ (**Fig. III-3b**), which coincides with Br$^-$ oxidation following a cubic dependence on Br$^-$ concentration alike what was expected for the Br$_3^-$ formation. Hence, we conclude that Br$^-$ is oxidized to Br$_3^-$ at any concentration tested in this study. Furthermore, we note that negative values of $\eta_{Br_3^-}$ are measured at all concentrations (**Fig. III-3b**), which is expected for a Nernstian reaction with fast kinetics and in the initial absence of the oxidized formed of the redox couple, *i.e.* absence of Br$_3^-$ in solution.[16,39] Indeed, the potential deviates from the standard potential following[39]:

$$E = E°_{Ox/Red} - \frac{RT}{nF} ln\left(\frac{j_l - j}{j}\right) \qquad eq.III-13$$

with j the measured current density and j_l the limiting current density as expressed following Levich equation[39]:

$$j_l = 0.62nFD_{Red}{}^{3/2}\omega^{1/2}\nu^{-1/6}c_{Red} \qquad eq.III-14$$

Hence, for n=2, F=96485 C.mol^{-1}, D_{Red}=2.080.10^{-5} cm^2.s^{-1}, ω=167 rad.s^{-1} (1600rpm), ν=10^{-2} cm^2.s^{-1} and c_{Red}=c^0=1 mol.L^{-1}, corresponding to the case of Br$^-$ oxidation to Br$_3^-$, **eq. III-14** gives an approximation of j_l=316 mA.cm^{-2}.[16] Applying **eq. III-13** for j=1 mA.cm^{-2} gives $-\frac{RT}{2F} ln\left(\frac{j_l - j}{j}\right)$= -74 mV. Hence at current density of 1 mA.cm^{-2}, the deviation from the standard potential is ≈ -74 mV. Data reported in **Fig. III-3b** are in agreement with such approximation, with a potential lower than the reversible potential by ≈ -50 mV at 1 mA.cm^{-2}.

The same methodology was applied to the oxidation reactions of Cl$^-$ (**eqs. III-15** to **III-26**). The theoretical three-dimensional graph obtained by plotting the Pourbaix diagram of the chloride-water system[145] as a function of the Cl$^-$ concentration is shown in **Fig. III-4a**.

$$Cl_{2(aq)} + 2e^- = 2Cl^-{}_{(aq)} \qquad eq.\ III-15$$

$$E = E°_{Cl_2/Cl^-} + \frac{RT}{2F} ln\left(\frac{a\left(Cl_{2(aq)}\right)}{a\left(Cl^-{}_{(aq)}\right)^2}\right) \qquad eq.III-16$$

$$\eta_{Cl_2} = E - \left(E°_{Cl_2/Cl^-} - \frac{RT}{2F} ln\left(c\left(Cl^-{}_{(aq)}\right)^2\right)\right) - iR - E_{LJP/\gamma} \qquad eq.III-17$$

$$Cl_3{}^-{}_{(aq)} + 2e^- = 3Cl^-{}_{(aq)} \qquad eq.III-18$$

$$E = E°_{Cl_3^-/Cl^-} + \frac{RT}{2F} ln\left(\frac{a\left({Cl_3^-}_{(aq)}\right)}{a\left({Cl^-}_{(aq)}\right)^3}\right) \qquad eq.III-19$$

$$\eta_{Cl_3^-} = E - \left(E°_{Cl_3^-/Cl^-} - \frac{RT}{2F} ln\left(c\left({Cl^-}_{(aq)}\right)^3\right)\right) - iR - E_{LJP/\gamma} \qquad eq.III-20$$

$$HClO_{(aq)} + {H^+}_{(aq)} + 2e^- = {Cl^-}_{(aq)} + H_2O_{(l)} \qquad eq.III-21$$

$$E = E°_{HClO/Cl^-} + \frac{RT}{2F} ln\left(\frac{a\left(HClO_{(aq)}\right).a\left({H^+}_{(aq)}\right)}{a\left({Cl^-}_{(aq)}\right).a\left(H_2O_{(l)}\right)}\right) \qquad eq.III-22$$

$$\eta_{HClO} = E - \left(E°_{HClO/Cl^-} - \frac{RT}{2F} ln\left(c\left({Cl^-}_{(aq)}\right)\right) + \frac{RT}{2F} ln\left(a\left({H^+}_{(aq)}\right)\right)\right) - iR - E_{LJP/\gamma} \qquad eq.III-23$$

$$ClO^-{}_{(aq)} + 2{H^+}_{(aq)} + 2e^- = {Cl^-}_{(aq)} + H_2O_{(l)} \qquad eq.III-24$$

$$E = E°_{ClO^-/Cl^-} + \frac{RT}{2F} ln\left(\frac{a\left(ClO^-{}_{(aq)}\right).a\left({H^+}_{(aq)}\right)^2}{a\left({Cl^-}_{(aq)}\right).a\left(H_2O_{(l)}\right)}\right) \qquad eq.III-25$$

$$\eta_{ClO^-} = E - \left(E°_{ClO^-/Cl^-} - \frac{RT}{2F} ln\left(c\left({Cl^-}_{(aq)}\right)\right) + \frac{RT}{F} ln\left(a\left({H^+}_{(aq)}\right)\right)\right) - iR - E_{LJP/\gamma} \qquad eq.III-26$$

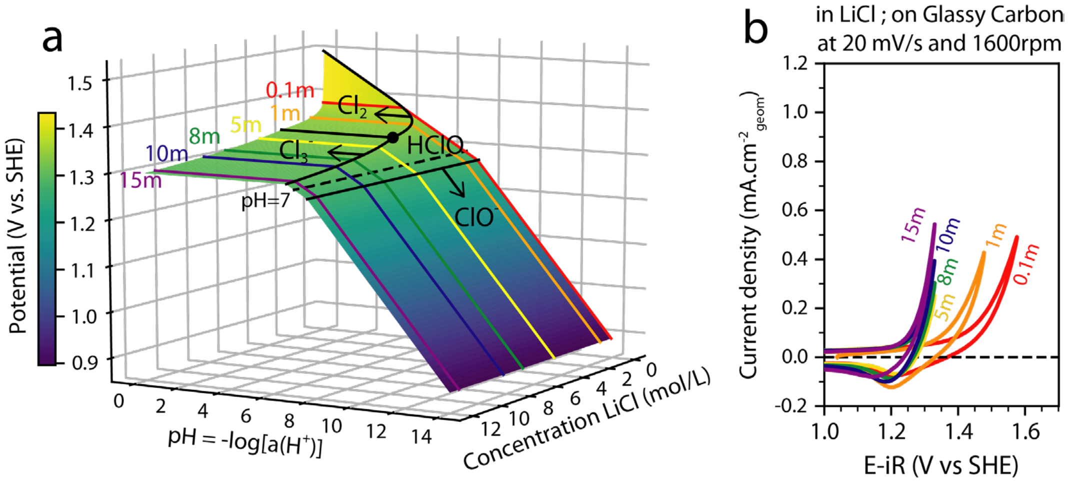

Fig. III-4. Chloride oxidation in highly concentrated LiCl solutions. a, Three-dimensional graph obtained by plotting the Pourbaix diagram of chloride (E = f(pH)) as function of the lithium chloride concentration. **b**, Cyclic voltammograms of the chloride oxidation recorded on Glassy Carbon rotating disk electrodes at 1600 rpm for LiCl solutions of concentration between 0.1m and 15m plotted as function of the ohmic drop compensated potential.

At pH above 7.5, hypochlorite anions (ClO^-) are formed, while for 6.5 < pH < 7.5, hypochlorous acid (HOCl) is preferentially formed. At lower pH, Cl^- is oxidized into chlorine (Cl_2) for concentrations below 3m or to trichloride (Cl_3^-) above 3m. Thus, similarly to the Br^-

oxidation, the formation of Cl_3^- is expected to be thermodynamically favoured in concentrated solutions that are slightly acidic.[117,139] However, for concentrations of Cl^- below 3m, Cl_2 or HOCl formation are expected to be thermodynamically favourable. The experimental CVs recorded as function of LiCl concentration (**Fig. III-4b**) show decreasing oxidation potentials with increasing concentrations, in accordance with Nernst equations (**eqs. III-16, III-19, III-22, III-25**).

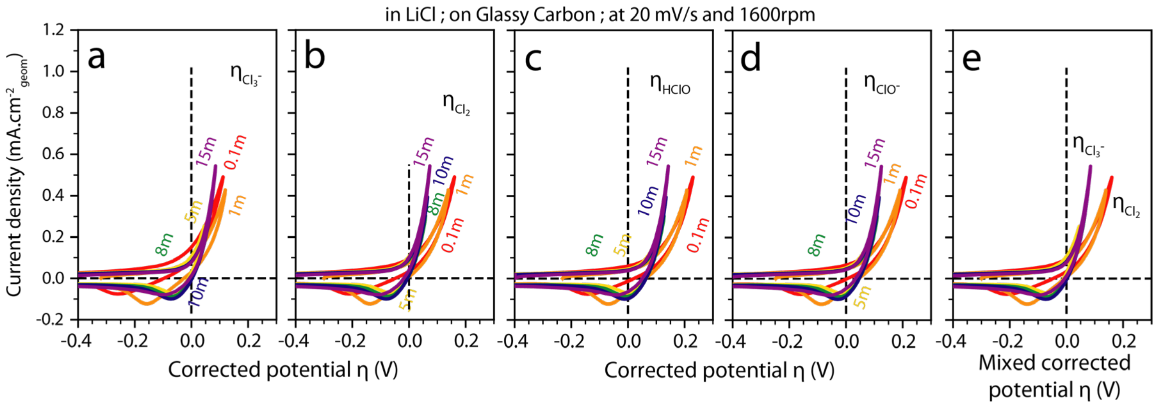

Fig. III-5. Halogens oxidation in highly concentrated LiCl solutions. a-d, Cyclic voltammograms described in (**Fig. III-4b**) with potentials corrected for the oxidation of chloride to trichloride (**a**), chlorine (**b**), hypochlorous acid (**c**) or hypochlorite (**d**) assuming pH=7 in Nernst equation. **e**, potentials corrected for the oxidation of chloride to chlorine for concentrations of 0.1m and 1m and corrected for the oxidation of chloride to trichloride for concentrations between 5m and 15m.

Using the $E_{LJP/\gamma}$ values obtained in **Chapter II** (**Fig. II-10c**) for Cl^- in LiCl, the corrected potentials (**Fig. III-5a, 5b, 5c, 5d**) of the four Cl^- oxidations reactions (**eqs. III-17, III-20, III-23, III-26**) were plotted. The corrected potentials are positive, suggesting an overpotential due to slower kinetics than for the Br^- oxidation. More importantly, none of the corrected potentials overlap at all concentrations (**Fig. III-5a, 5b, 5c, 5d**), suggesting that a unique reaction cannot explain the potential shifts in the whole concentration range. Nevertheless, $\eta_{Cl_3^-}$ are found to overlap for concentrations from 15m down to 5m, while η_{Cl_2}, η_{HClO} or η_{ClO^-} overlap for concentrations below 1m (**Fig. III-5e**). Overall, concordant with the three-dimensional Pourbaix diagram, we can expect that the oxidation of Cl^- below 3m leads to the formation of Cl_2 or HOCl while in regimes pertinent to ABS, *i.e.* above 3m, Cl_3^- is formed.

Extending our study to iodide (**eqs. III-27 to III-32**), the theoretical three-dimensional graph obtained by plotting the Pourbaix diagram of the iodide-water system[145] as a function of the I^- concentration is shown in **Fig. III-6**.

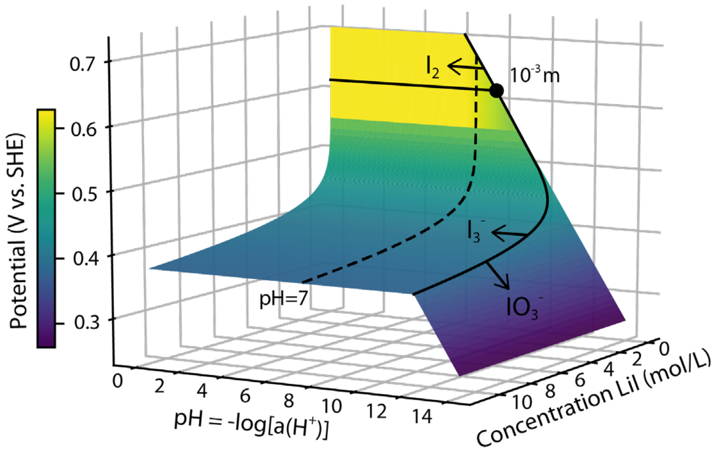

Fig. III-6. Iodide oxidation in highly concentrated solutions. Three-dimensional graph obtained by plotting the Pourbaix diagram of iodide (E = f(pH)) as function of the lithium iodide concentration.

$$I_{2(aq)} + 2e^- = 2I^-{}_{(aq)} \qquad eq.\mathrm{III}-27$$

$$E = E°_{I_2/I^-} + \frac{RT}{2F} ln\left(\frac{a\left(I_{2(aq)}\right)}{a\left(I^-{}_{(aq)}\right)^2}\right) \qquad eq.\mathrm{III}-28$$

$$I_3{}^-{}_{(aq)} + 2e^- = 3I^-{}_{(aq)} \qquad eq.\mathrm{III}-29$$

$$E = E°_{I_3{}^-/I^-} + \frac{RT}{2F} ln\left(\frac{a\left(I_3{}^-{}_{(aq)}\right)}{a\left(I^-{}_{(aq)}\right)^3}\right) \qquad eq.\mathrm{III}-30$$

$$IO_3{}^-{}_{(aq)} + 6H^+{}_{(aq)} + 6e^- = I^-{}_{(aq)} + 3H_2O_{(l)} \qquad eq.\mathrm{III}-31$$

$$E = E°_{IO_3{}^-/I^-} + \frac{RT}{6F} ln\left(\frac{a\left(IO_3{}^-{}_{(aq)}\right).a\left(H^+{}_{(aq)}\right)^6}{a\left(I^-{}_{(aq)}\right)}\right) \qquad eq.\mathrm{III}-32$$

At pH above 12, iodate anions (IO_3^-) are formed. At lower pH, iodide is oxidized to iodine (I_2) only below 10^{-3} m while above 10^{-3} m iodine is oxidized to triiodide (I_3^-). Thus, at high concentration, *i.e.* in regimes pertinent to ABS, iodide, bromide and chloride are all oxidized to trihalides.

The recent studies on ABS by Dubouis *et al.*[33,107] show that the halogen-rich (top) phase contains small amount of LITFSI, and *vice versa*. To evaluate the potential impact of LiTFSI and LiCl on Br^- oxidation, mix solutions containing both lithium halides (LiBr and LiCl) or LiBr with LiTFSI were studied. Addition of large amount of LiCl (5m to 8m, **Fig. III-7a**) or small amount of LiTFSI (0.1 mol.L^{-1}, **Fig. III-7b**) in concentrated LiBr solutions does not lead to substantial changes in Br^- oxidation. Instead, we reveal that by adding large amount of LiTFSI (1m to 15m) in diluted LiBr solutions, Br^- oxidation is facilitated (**Fig. III-7c**) due to LJP and potential shift due to ions' activity coefficient in concentrated LiTFSI solutions (estimated in **Fig. III-S2**) as shown with the overlapping $\eta_{Br_3^-}$ corrected potentials in **Fig. III-7d**.

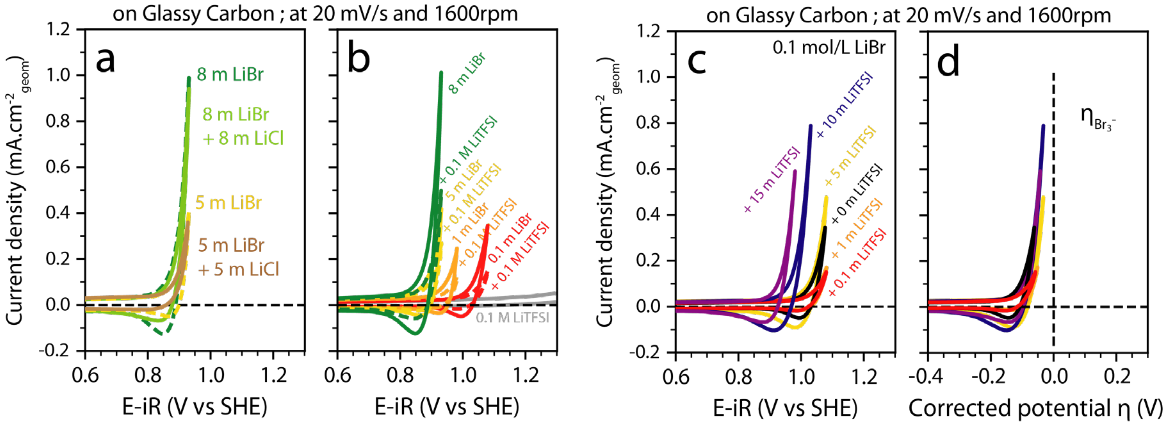

Fig. III-7. Bromide oxidation in mixed LiBr, LiCl and LiTFSI solutions. a, Cyclic voltammograms of the bromide oxidation on Glassy Carbon rotating disk electrodes at 1600 rpm for 5m LiBr solution compared to 5m LiBr + 5m LiCl solution and 8m LiBr solution compared to 8m LiBr + 8m LiCl solution. **b**, Cyclic voltammograms of the bromide oxidation on Glassy Carbon rotating disk electrodes at 1600 rpm for LiBr solutions between 0.1m and 8m without (solid lines) and with 0.1 mol.L^{-1} LiTFSI (dotted lines). **c**, Cyclic voltammograms of the bromide oxidation on Glassy Carbon rotating disk electrodes at 1600 rpm for 0.1 mol.L^{-1} LiBr with added LiTFSI from 0.1m to 15m. **d**, Potentials corrected for oxidation on Glassy Carbon rotating disk electrodes at 1600 rpm for 0.1 mol.L^{-1} LiBr with added LiTFSI from 0.1m to 15m.

To confirm that trihalides are formed, the equilibrium in concentrated solutions between Br_2 and Br_3^- (**eq III-33**) was assessed:

$$Br_{2(aq)} + Br^-{}_{(aq)} = Br_3{}^-{}_{(aq)} \qquad eq.\mathrm{III}-33$$

For this, Ultraviolet-Visible (UV-Vis) measurements were carried out for 1m and 15m LiBr solutions with added Br_2 (**Fig. III-8a and 8b in red**). Absorption maxima and absorption coefficient of halogens and trihalides are given in **Table III-S1** and **Table III-S2**.[146–150] Solely the absorption band of Br_3^- was observed for 1m LiBr (**Fig. III-8a in red**, at 266 nm) as well as for 15m LiBr (**Fig. III-8b in red**, at 277nm), confirming that Br_3^- is favorably formed over Br_2 at LiBr concentration above 1m and up to 15m. The absorption band of Br_3^- in 15m LiBr is found slightly red shifted compare to 1m LiBr which could be linked to solvatochromism effect resulting from the high LiBr concentration. Nevertheless, with the Br_2/Br_3^- equilibrium being displaced toward the formation of Br_3^-, Br_2 is found highly soluble in LiBr concentrated solutions, as show in **Fig. III-8c** where a 15m $LiBr_3$ solution was formed by adding equimolar quantities of Br_2 in a 15m LiBr solution. On the contrary, solubility of Br_2 as estimated from Beer-Lambert law at 407 nm is found limited in 20m LiTFSI (Br_2 solubility in 20m LiTFSI ≈0.03 $mol.L^{-1}$ compared to ≈0.21 $mol.L^{-1}$ in pure water[151]), and no Br_3^- was observed as Br^- is absent for **eq. III-33** to take place (**Fig. III-8a in orange and III-8d**).

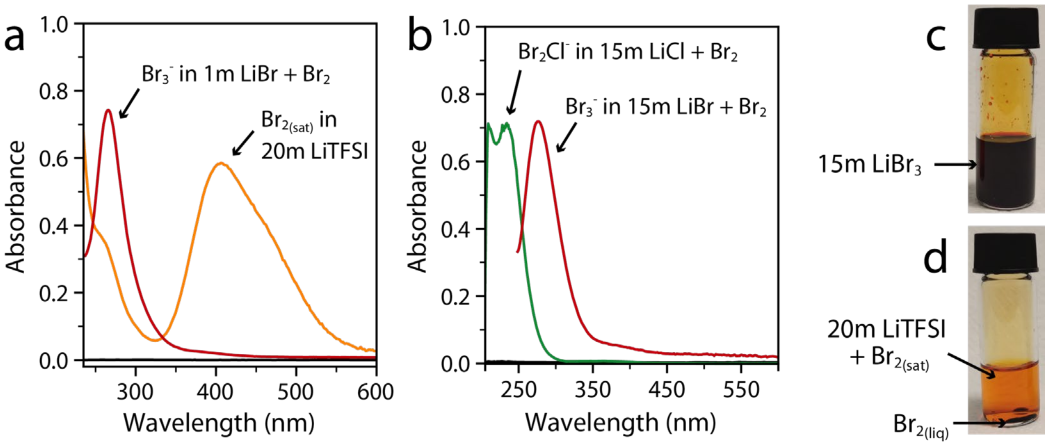

Fig. III-8. UV-Vis detection and pictures of Br_3^- and Br_2 in LiBr and LiTFSI, respectively. a, UV-Vis spectra of diluted Br_2 in 1m LiBr forming Br_3^- (red) with a maximum at 266 nm and UV-Vis spectra recorded for Br_2 saturated in 20m LiTFSI (orange) with a maximum at 407 nm. **b**, UV-Vis spectra of diluted Br_2 in 15m LiBr forming Br_3^- (red) with a maximum at 277 nm and diluted Br_2 in 15m LiCl forming Br_2Cl^- (green) with a maximum at 235 nm. **c**, Picture of equimolar quantities of Br_2 in 15m LiBr forming a 15m $LiBr_3$ solution. **d**, Picture of the 20m LiTFSI solution saturated in Br_2 (drops of liquid Br_2 are in the solution as it is saturated).

For mixed LiBr-LiCl solutions, Br_3^- is in equilibrium with Br_2Cl^- (**eq. III-34**), however Br_3^- is thermodynamically more favorable hence the first oxidation in **Fig. III-1b** is expected to be mainly the oxidation of Br^- to Br_3^- (**eq. III-6**) while Br_2Cl^- could be formed at the end of the first oxidation when all Br^- anions in solutions have been oxidized to trihalides in the remaining LiCl solution (**eq. III-34** and **Fig. III-8b in green**).[141,150]

$$Br_3{}^-{}_{(aq)} + Cl^-{}_{(aq)} \underset{\longrightarrow}{\longleftarrow} Br_2Cl^-{}_{(aq)} + Br^-{}_{(aq)} \;\;;\;\; K = 8.10^{-2} \qquad eq.III-34$$

$$Cl_3{}^-{}_{(aq)} + Br^-{}_{(aq)} \underset{\longleftarrow}{\longrightarrow} BrCl_2{}^-{}_{(aq)} + Cl^-{}_{(aq)} \;\;;\;\; K = 33.3 \qquad eq.III-35$$

Similarly, Cl_3^- is in equilibrium with $BrCl_2^-$ (**eq. III-35**), with $BrCl_2^-$ being more stable,[141,145,150] thus the second peak in **Fig. III-1b** is expected to be mainly the oxidation of Cl^- to $BrCl_2^-$ (**eq. III-36**):

$$Br_2Cl^-{}_{(aq)} + 3Cl^-{}_{(aq)} = 2BrCl_2{}^-{}_{(aq)} + 2e^- \qquad eq.III-36$$

III.C. Two-step halogen intercalation

We have demonstrated that monophasic solutions at high concentration such as those encountered in ABS do not prevent halides oxidation, and instead push the oxidation reaction toward the formation of trihalides (Br_3^-, Br_2Cl^-, $BrCl_2^-$, Cl_3^-). Thus, our attention then turned to biphasic systems and understanding the selectivity toward trihalide anions of the liquid/liquid interface formed for the LiTFSi-LiCl/LiBr-water system. For that, Br_3^- was formed in a 5m LiTFSI - 10m LiBr ABS by addition of Br_2 (**Fig. III-9a and 9b**). Doing so, we observed the characteristic color (**Fig. III-9b**) and UV-Vis absorption peak (**Fig. III-9c**) associated with Br_3^- only in the halide-rich phase (top phase), while the TFSI-rich phase (bottom phase) remains colorless. This finding indicates that Br_3^- spontaneously separates from the TFSI-rich phase.

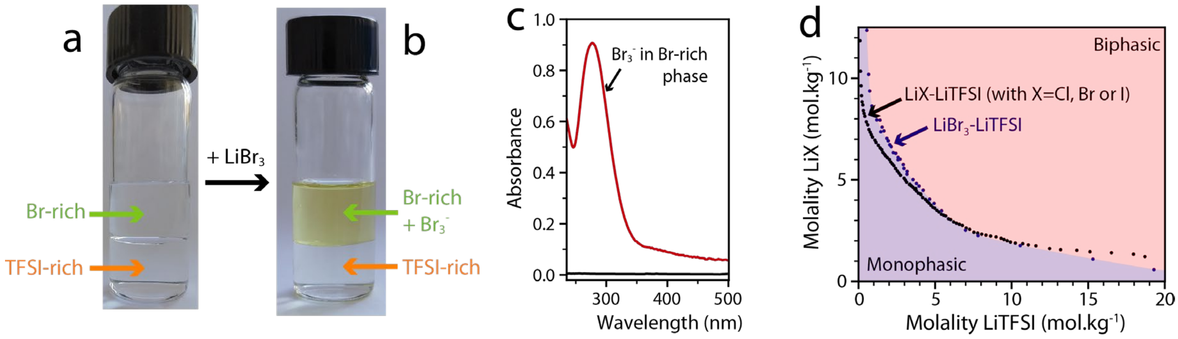

Fig. III-9. ABS confines Br_3^- in the Br-rich phase. a-b, Pictures of a 5m LiTFSI - 10m LiBr ABS without (**a**) and with added $LiBr_3$ (**b**). **c**, UV-Vis of Br-rich phase (top phase) of ABS with added bromine, showing the formation of tribromide. **d**, Comparison of the phase diagram of the LiTFSI-$LiBr_3$-water system (dark blue) with the phase diagram of the LiTFSI-LiBr-water system (black).

To confirm this assertion, the phase diagram for the LiTFSI-$LiBr_3$-water system was determined by cloud point titration and compared with that of LiTFSI-LiBr-water ABS[33,107,143] (**Fig. III-9d**). Both phase diagrams are found very similar, with only a slight increase of the miscible domain at large concentration of Br_3^- along with a slight decrease of the miscible domain at large concentration of LiTFSI when compared to LiBr. We thus conclude that trihalides behave similarly to halides and thus will mostly not mix into the TFSI-rich phase. This finding has a major implication for the electrochemical device, as trihalides electrochemically generated during battery operation will mainly stay confined in the halide-rich phase at the positive electrode. Hence, the liquid/liquid interface plays a confinement role, avoiding cross-diffusion of the oxidation products toward the negative electrode.

Thus far, our study revealed that at high concentration, halides are oxidized to trihalides at ≈0.85 V vs SHE for Br^- (**Fig. III-2**, **Fig. III-3** and **eq. III-6**) and at ≈1.25 V vs SHE for Cl^- (**Fig. III-4**, **Fig. III-5** and **eq. III-18**), *i.e.* at potentials similar to those recorded for the conversion/intercalation of halogens into graphite (**Fig. III-1b**). Such finding suggests that either trihalides are a side product of the conversion/intercalation reaction which is confined at the positive electrode in the halide-rich phase, the ABS thus inhibiting the cross-diffusion to the negative electrode and ensuring that trihalides can be reduced back during discharge, or that trihalides are involved into the conversion/intercalation mechanism. To probe if trihalides are involved into the conversion/intercalation mechanism, graphite electrodes were exposed to trihalide solutions, before to be analyzed by X-ray powder diffraction (**Fig. III-10a and 10b**). A Rietveld refinement[152] confirms that pristine graphite presents an interlayer spacing of 6.716(2) Å, in line with previous reports[153] (**Fig. III-10a**). However, when graphite is exposed to 10m LiBr + 5m $LiBr_3$, the (002) and (004) diffraction peaks shift to lower angles (**Fig. III-10b**), indicating an interlayer spacing of graphite increase to 6.811(2) Å, as deduced from the Rietveld refinement (**Fig. III-10a**). The increase of interlayer distance concurs with the intercalation of Br_2 into graphite, as previously reported[7,153], hence proving that trihalides are involved in the halogen intercalation mechanism following a chemical equilibrium (**eq. III-37**):

$$X_3{}^-{}_{(sol)} + C_{6(s)} = C_6[X_2]_{(s)} + X^-{}_{(sol)} \quad (X = Br, Cl) \qquad eq.\mathrm{III}-37$$

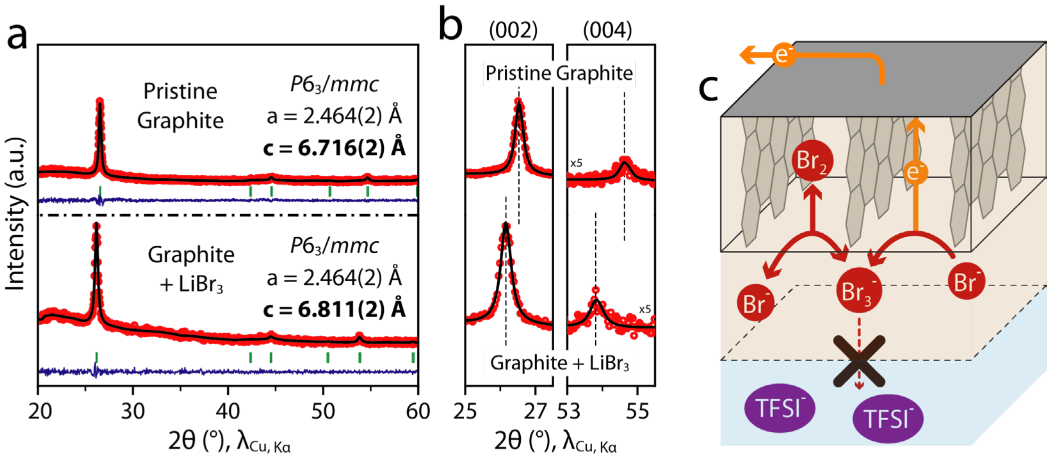

Fig. III-10. Br_3^- in the Br-rich phase enables the chemical intercalation of Br_2 into graphite. a-b, Rietveld refinement (**a**) of the pristine graphite (top) and of graphite in contact with $LiBr_3$ (bottom). The red circles, black continuous line and bottom blue line represent the observed, calculated, and difference patterns respectively. Vertical green tick bars are the Bragg positions. A zoom on the (002) and (004) reflections is shown in (**b**). **c**, Scheme of the two-step halides intercalation mechanism.

Experimental results thus suggest that intercalation of halogen can follow a two-step reaction, with first the electrochemical oxidation of halides to trihalides (**eq. III-3**) followed by chemical intercalation of halogens into graphite (**eq. III-37**), as illustrated with **Fig. III-10c**. To assess the equilibrium between trihalides in solution and halogens intercalated in graphite, quantitative UV-Vis spectroscopy was conducted after electrolysis of halide solutions using graphite electrodes (**Fig. III-11**). Potentials of 0.9 V vs SHE and 1.3 V vs SHE are respectively measured for the electrolysis of 15m LiBr (**Fig. III-11a in red**) and 15m LiCl (**Fig. III-11a in green**) solutions (1.2 mA for 8 min, charged passed of 0.576 C), similar to the potentials of both halogens conversion/intercalation (**Fig. III-1b**) and halides oxidation to trihalides (**Fig. III-3** and **Fig. III-4b**). UV-Vis conducted after the electrolysis of 15m LiBr shows the characteristic spectra of Br_3^- (**Fig. III-11b**) while for the electrolysis of 15m LiCl, spectra is characteristic of $BrCl_2^-$ or Br_2Cl^- (**Fig. III-11c**), most probably due to Br^- impurities coming from commercial LiCl salt (**eq. III-35** and **eq. III-38**).

$$BrCl_2{}^-{}_{(aq)} + Br^-{}_{(aq)} = Br_2Cl^-{}_{(aq)} + Cl^-{}_{(aq)} \quad ; \quad K = 3.10^3 \qquad eq. III-38$$

More importantly, theoretical concentrations calculated from the charge passed during the electrolysis ($Q_{electrolysis}$; **Fig. III-11a in blue**) using Faraday law (**Fig. III-11d in blue**) were then compared with absorption maximums (**Fig. III-11b and 11c**) and experimental concentrations calculated using Beer-Lambert law (**Fig. III-11d in red and green**). We found that ≈63% of the Br_3^- generated during the electrolysis of 15m LiBr stays in the electrolyte, the rest being intercalated as Br_2 into graphite (≈37%). Similarly, ≈89% of $BrCl_2^-$ generated by the electrolysis of 15m LiCl stays in the electrolyte while only ≈11% are intercalated as bromine monochloride (BrCl).[7] Our results thus demonstrate that a large part of the charged passed can be stored as trihalides in the electrolyte instead of intercalated halogens in graphite.

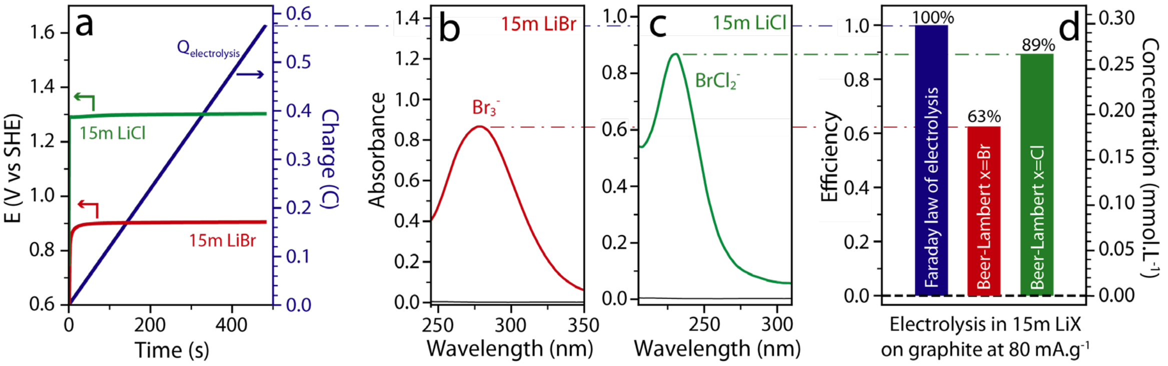

Fig. III-11. Electrolysis of LiBr and LiCl solutions along with quantitative UV-Vis to detect oxidation products. a, Chronopotentiometry at 1.2 mA for 8 minutes recorded for electrolysis of 15m LiBr (red) and 15m LiCl (green) solutions. In blue is plotted the charge passed during the electrolysis. **b-c**, UV-Vis spectra of the 15m LiBr (**b**) and 15m LiCl (**c**) electrolytes after electrolysis. **d**, Efficiency of the electrolysis calculated by comparing the ideal Faraday law of electrolysis with the concentration detected via Beer-Lambert law.

Nevertheless, one as to keep in mind that such intercalation percentages are highly dependent on the electrode/electrolyte ratio, with here a large excess of electrolyte (≈2 $g.mg^{-1}_{graphite}$) leading to lower intercalation percentage compared to cells reported by Yang C. *et al.*[7] for instance (≈0.01 $g.mg^{-1}_{graphite}$).[7] Bearing this in mind, we tried to reduce the electrode/electrolyte ratio by using Swagelok cells, similarly to Yang C. *et al.*[7], however cycling performances both two- and three-electrodes cells where found limited (**Fig. III-12**). Knowing that we could never reproduce the artificial SEI nor the jellified WiSE reported previously[7,32], such poor performance can arise from the lack of electrolyte viscosity and coating at the anode material which could both prevent self-discharge and improve the cycling behavior.

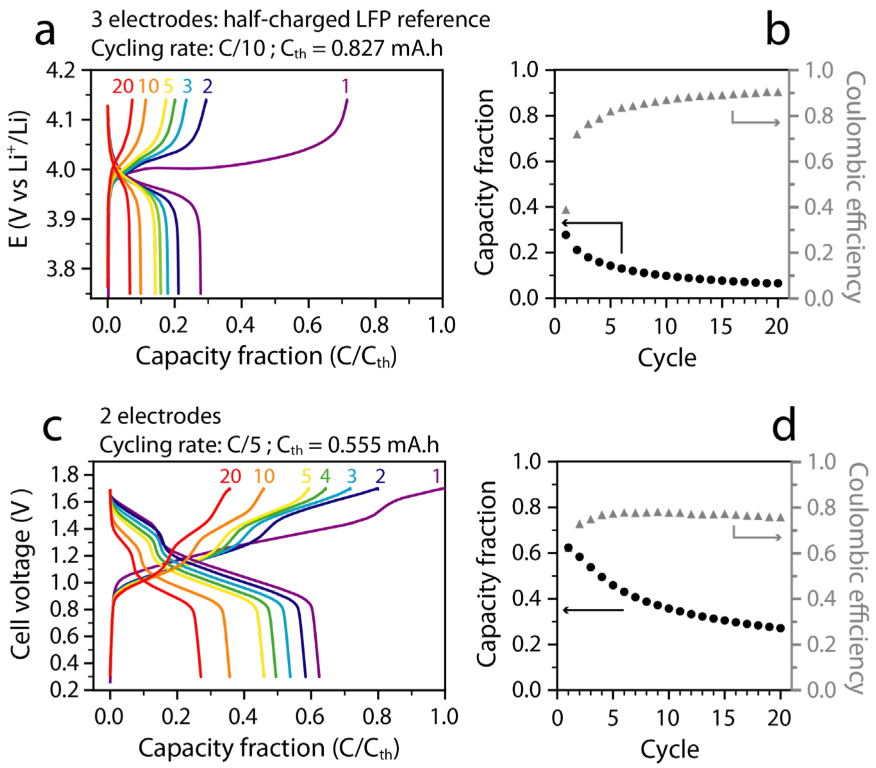

Fig. III-12. Galvanostatic charge/discharge performances of the halogens intercalation chemistry in two or three electrodes Swagelok cells. a, Galvanostatic charge/discharge cycles at C/10 in three electrodes Swagelok cells with Graphite/LiBr/LiCl/SP positive electrodes, YP-50F negative electrode and half-charge LFP reference. **b**, Capacity fraction and Coulombic efficiency for the cycles in (**a**). **c**, Galvanostatic charge/discharge cycles at C/5 in two electrodes Swagelok cells with Graphite/LiBr/LiCl/SP positive electrodes, YP-50F negative electrode. **d**, Capacity fraction and Coulombic efficiency for the cycles in (**c**).

III.D. Chapter conclusions

Overall, we proved that high concentrations of halide salts, as the ones find in ABS, enable the oxidation of halides to trihalides at potentials similar to the ones previously reported for conversion/intercalation of halides into graphite. Moreover, the spontaneous intercalation of Br_2 into graphite via Br_3^- was proved to be possible. Hence, our electrochemical and spectroscopic results demonstrate that the intercalation of halogen into graphite can follow a two-step intercalation with first the oxidation of halides to trihalides (**eq. III-3**) followed by chemical intercalation of halogens (**eq. III-37**). Such two-step intercalation concurs with a recent study from Xu *et al.* using quasi-ionic liquid electrolyte[154] where halides are first oxidized to liquid halogens and then intercalated in graphite. An important implication of our finding is that, alike halogens and intercalated halogens[155,156], trihalides in solution and the intercalated halogens are in dynamic equilibrium (**eq. III-37**). As a consequence, this battery is not truly a "dual-ion battery" but more a redox "static" battery similar to a non-flowing zinc-bromide hybrid redox battery[157], where the zinc negative electrode is replaced by the negative graphite Li^+ intercalation electrode while the positive electrode graphite intercalation plays the role of complexing agent replacing the quaternary ammonium bromides usually used in zinc-bromide batteries.[157] Quantitative UV-Vis analysis proved that for the equilibrium between trihalides and intercalated halogens (**eq. III-33**), a non-negligible part of the capacity is carried by trihalides in solution, increasing the risk of self-discharge via the diffusion of trihalides to the negative electrode. However, our work unambiguously demonstrates that trihalides are highly soluble in the halide-rich phase, *i.e.* the phase in contact with the positive electrode, while trihalides are poorly soluble in the TFSI-rich phase, *i.e.* the phase in contact with the negative electrode, demonstrating ABS to be the cornerstone in reaching good coulombic efficiencies by thermodynamically preventing the diffusion of trihalides to the negative electrode. Even though the use of ABS would most probably limit such device to stationary applications in order to have a proper layering of the ABS, the development of ABS could be key to improve efficiencies and cost of other batteries such as redox "static" zinc-halogen,[35–38] or redox flow batteries. Indeed, by spontaneously separating the positive and negative electrolytes without the use of expensive and fragile membranes, ABS can be further used to develop membrane-less redox batteries. Importantly, our work put forward the possibility to use as redox species the salts forming the ABS, such as the halides/trihalides redox, reaching higher concentration and thus higher capacities than previous work based on the addition of organic redox species to an already formed ABS.[56,77,78] Nevertheless, to optimize cost, LiTFSI quantities have to be minimized thus aiming at the top-left part of the ABS diagram (**Fig. III-9d**), *e.g.* 2m LiTFSI – 10m LiBr ABS, while future work will have to find cheaper and safer alternatives to LiTFSI that would still form an ABS with lithium halides/trihalides. Moreover, moving from a redox "static"[77,56,158] to a redox "flow"[78] membrane-less battery brings the challenge of maintaining a proper layering of ABS with the need to design suitable flow-cells with an optimal flow of the positive and negative electrolytes. Finally, the use of ABS in electrochemical devices is still in its infancy, and further work is needed to improve our understanding of the electrochemistry of the ABS, especially concerning the selectivity and kinetics of ion transfer at liquid-liquid interface which will be critical for achieving both good coulombic efficiency and high power density.

Chapter IV – ABS liquid-liquid interface

This chapter is based on the following article that I co-authored:

> Degoulange D., Pandya R., Deschamps M., Skiba D.A., Gallant B.M., Gigan S., de Aguiar H.B. and Grimaud A., "Direct imaging of micrometer-thick interfaces in salt–salt aqueous biphasic systems", *Proceedings of the National Academy Of Sciences* **120**, e2220662120 (2023).

IV.A. Introduction

As described in **Chapter I** and further investigated in **Chapter III**, the development of membrane-less electrochemical devices heavily relies on finding systems preventing the crossover of redox active ions, *e.g.* trihalides. However, it is nonetheless crucial for the liquid-liquid interface to enable the ion transfer and ensure the electroneutrality during battery operation. Furthermore, the kinetics for ion transfer must be fast enough not to introduce overpotential. Thus, for salt-salt ABSs to be efficiently implemented in electrochemical devices, mastering the ion transfer at liquid-liquid interface is critical as it directly controls the (dis)charging rate by inducing an interfacial overpotential if too slow or can induce self-discharge when not selective. Despite this key role, interfaces of ABSs are poorly understood, almost entirely *via* surface tension measurements.[159–162] Classically, the surface tension between two phases α and β is captured by the Gibbs adsorption equation:

$$\mathrm{d}\gamma = -\sum_{\mathrm{J}} \mathit{\Gamma}_{\mathrm{J}} \mathrm{d}\mu_{\mathrm{J}} \qquad eq.\,\mathrm{IV}-1$$

with γ being the surface tension between the two phases, $\mathit{\Gamma}_{\mathrm{J}}$ the surface excess concentration compared to the Gibbs dividing surface and μ_{J} the chemical potential of the different species J in solution.[163] Noting that $\mu_{\mathrm{J}} = \mu_J^0 + RT\ln(a_J)$, the surface excess concentration can be expressed as:

$$\Gamma_S = -\frac{a_S}{RT}\left(\frac{\partial \gamma}{\partial a_S}\right)_{T,J\neq S} \qquad eq.\mathrm{IV}-2$$

linking the surface tension to the adsorption of species at the interface.[163] If by increasing the activity of species *S* the surface tension decreases (*i.e.* $\left(\frac{\partial \gamma}{\partial a_S}\right) < 0$), then $\Gamma_S > 0$ and the species *S* is accumulated at the interface (positive adsorption – **Fig. IV-1a**). However, if by increasing the activity of species S the surface tension increases (*i.e.* $\left(\frac{\partial \gamma}{\partial a_S}\right) > 0$), then $\Gamma_S < 0$ and the species S is depleted at the interface (negative adsorption – **Fig. IV-1b**).[163] The thickness of the interface can be defined as the length across which the negative (or positive) adsorption takes place.

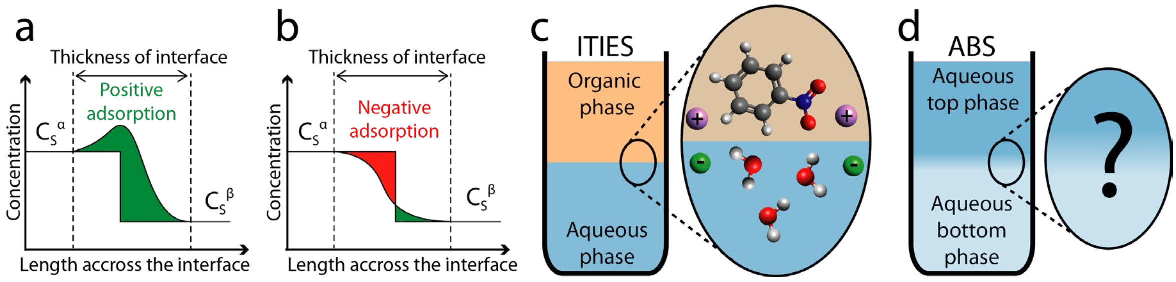

Fig. IV-1. Description of the different types of liquid-liquid interfaces. a-b, Schematic depicting the concentration profile of a solute (S) from phase α ($C_S{}^\alpha$) to phase β ($C_S{}^\beta$) across an interface for positive (**a**) and negative (**b**) adsorption. Green and red represent, respectively, positive and negative integrals when compared to a step change of concentration. **c-d**, Cartoons of ITIES (**c**) and ABSs (**d**) interfaces.

In contrast to ABSs, interfaces between two immiscible electrolyte solutions (ITIES), such as between water and nitrobenzene or other polar solvents, have been widely studied. They are known to be molecularly sharp with a positive adsorption of ions over only a few nanometers at the interface (**Fig. IV-1c**), as demonstrated by a combination of surface tension, capacitance and surface-sensitive spectroscopic methods.[164,70,60,68] This picture of the ITIES was essential towards developing new applications based on ion[72,73] or electron transfer[165,166] such as coupling reactions[167] or electrosynthesis[168] at the interface. Thus, for ABSs to reach their full potential, a deeper understanding of their interfaces is critical (**Fig. IV-1d**). Yet the requirement of nanoscale chemical sensitivity means, to the best of our knowledge, that no experimental visualization of any aqueous-aqueous interfaces has yet been reported, with information regarding their composition remaining generally sparse. In this work, we use a unique combination of variable temperature nuclear magnetic resonance (VT-NMR) and high-spatial-resolution Raman imaging to resolve and understand the interface of salt-salt ABSs. Studying the LiTFSI-LiCl-water and the LiTFSI-HCl-water systems, we provide the demonstration for a negative adsorption of ions and water at the interface. Strikingly, we reveal a continuous, microscale change of chemical environment, fundamentally different from the nanoscale, molecularly sharp ITIES. Our results call for the reinvestigation of previously known ABSs using chemically sensitive imaging/spectroscopic methods and to, more broadly, study the structure and dynamics of liquid-liquid interfaces.

IV.B. Characterization of the LiTFSI-LiCl-water system

To first understand the composition demixing for the LiTFSI-LiCl-water system, the phase diagram was obtained *via* the cloud point titration technique (see details in **S-IV: Materials and Methods**). As shown in **Fig. IV-2a**, the phase diagram shows a binodal curve separating the monophasic region (purple) from the biphasic one (red).[33,107] The interfacial tension for the LiTFSI-LiCl-water systems were measured from the drop-weight method (see details in **S-IV: Materials and Methods**) using Tate's law with Harkins and Brown correction[169] (**Fig. IV-2b**). For the 5m LiTFSI – 10m LiCl biphasic system, the interfacial tension is estimated as ≈3 $mN.m^{-1}$. This value is similar to IL-salt ABSs (0.4 to 2.3 $mN.m^{-1}$)[162] but ten times lower than values reported for ITIES (20 to 30 $mN.m^{-1}$)[164] and higher than that reported for polymer-polymer ABSs (0.01 to 500 $\mu N.m^{-1}$)[159,170]. Decreasing the molalities to 3m LiTFSI – 6m LiCl, the interfacial tension decreases down to values ≈200 $\mu N.m^{-1}$. When plotting the interfacial tension as a function of the difference between salts total molality from these systems and the binodal curve at 2.6m LiTFSI – 5.2m LiCl (Δm, **Fig. IV-2b**), the surface tension tends to zero when reaching the binodal curve, *i.e.* for $\Delta m = 0$. This result agrees with the system becoming monophasic on crossing the binodal curve, hence having no interfacial tension. According to **eq. IV-2**, this increasing interfacial tension with increasing molality suggests either that salts have a negative adsorption at the interface, as schematized in **Fig. IV-1b**, or that water has a positive adsorption, as schematized in **Fig. IV-1a**, or both.

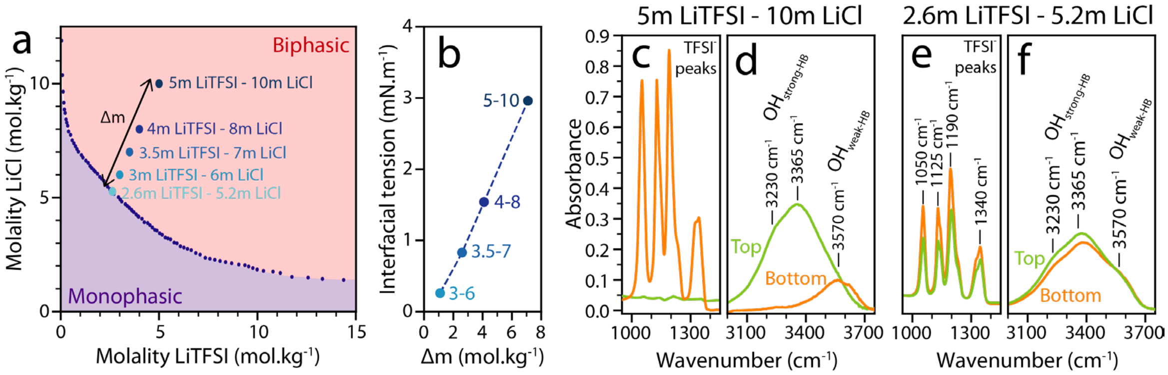

Fig. IV-2. LiTFSI-LiCl-water system description. a, Phase diagram of the LiTFSI-LiCl-water system with the monophasic region in purple and the biphasic region in red. Xm LiTFSI - Ym LiCl systems are studied along the line 2X=Y, as indicated with light to dark blue dots. Along this line, the binodal curve is crossed at 2.6m LiTFSI – 5.2m LiCl. **b**, Interfacial tensions for the LiTFSI-LiCl-water system as function of the salts total molality differential to the binodal curve in moles per kg (Δm) i.e. Δm=(X+Y)-(2.6+5.2). **c-d**, Infra-red spectra recorded for the 5m LiTFSI - 10m LiCl system for TFSI⁻ vibrations (**c**) and OH vibrations (**d**) with top phase in green and the bottom phase in orange. **e-f**, Infra-red spectra for the 2.6m LiTFSI - 5.2m LiCl system for TFSI⁻ vibrations (**e**) and OH vibrations (**f**) with the top phase in green and the bottom phase in orange.

The top and bottom phases collected from the 5m LiTFSI – 10m LiCl biphasic system were characterized by infrared spectroscopy (**Fig. IV-2c and 2d**). By looking at the TFSI⁻ peaks at 1340, 1190, 1125 and 1050 cm^{-1} (**Fig. IV-2c**), the top phase is found to be nearly depleted in TFSI⁻ anions while the bottom phase is rich in TFSI⁻[33]. In **Fig. IV-2d**, the peak at 3365 cm^{-1} and the shoulder at 3230 cm^{-1} corresponding to OH vibrations for water molecules with strong hydrogen bonding network ($OH_{strong-HB}$) are only observed for the top phase.[171,172] In contrast, the bottom phase shows a band at 3570 cm^{-1} previously ascribed to OH vibrations for water with weaker hydrogen bonding network resembling that of the so-called water-in-salt systems, *i.e.* a TFSI-rich environment ($OH_{weak-HB}$).[172,173] The bottom phase is thus richer in TFSI⁻ when compared to the top one, indicating a high ion partition coefficient. By decreasing the concentration close to the binodal curve and studying the 2.6m LiTFSI – 5.2m LiCl system (**Fig. IV-2e and 2f**), vibrations associated with the top and the bottom phases are found qualitatively similar, however with the intensities of the TFSI⁻ peaks still being modestly higher in the bottom phase, thus resulting in a low ion partition coefficient (**Fig. IV-2e**). Moreover, **Fig. IV-2f** shows that the intensity of the shoulder in the region of the $OH_{weak-HB}$ vibration is constant for both phases. Only a slight decrease in the region corresponding to $OH_{strong-HB}$ vibrations intensity, linked to a weakening of the water-water hydrogen bonding network, is found in the bottom phase. Overall, IR spectroscopy indicates that when moving away from the binodal curve, *i.e.* as the interfacial tension increases, there is greater ion partition between the two immiscible phases.

To probe the influence of temperature on salt-salt ABSs interface, the 2.6m LiTFSI – 5.2m LiCl system was studied between 0°C and 35°C. Upon cooling from room temperature to a temperature close to 0°C, the system reversibly switches from biphasic to monophasic, forming a so-called lower critical temperature (T_{LC}) system. This is confirmed by reaction microcalorimetry[163,174]. Indeed, T_{LC} systems, as the LiTFSI-LiCl-water system, have a negative Gibbs free energy of mixing ($\Delta_{mix}G < 0$) for temperatures below T_{LC}, enabling mixing at low temperature, and a positive Gibbs free energy of mixing ($\Delta G_{mix} > 0$) for temperature above T_{LC}. As discussed in the field, since $\Delta G_{mix} = \Delta H_{mix} - T\Delta S_{mix}$, having a T_{LC} implies that both the enthalpy and entropy of mixing for the LiTFSI-LiCl-water system are negative ($\Delta H_{mix} < 0$ and $\Delta S_{mix} < 0$). To probe the enthalpy of mixing, titration calorimetry was carried out. The enthalpy of mixing $\Delta_{mix}H$ is given by:

$$\Delta_{mix}H = H - \sum_{i} x_i H_i \qquad eq. IV - 3$$

with H being the enthalpy of the mixture and H_i the enthalpy of the pure substances. However, the enthalpy measured during the titration calorimetry as carried out in this work differs from the enthalpy of mixing as pure substances are not injected into the solvent. Rather, biphasic systems were first prepared at the temperature at which the system is immiscible (at 25°C for LiTFSI-LiCl-water system) and then separated. Following this, during the titration calorimetry, one phase was injected into the second one at a temperature at which these two solutions are miscible (at 2°C for LiTFSI-LiCl-water system) giving access to an enthalpy that can be described as a partial mixing enthalpy $\Delta_{mix}H'$ with:

$$\Delta_{mix}H' = H - \sum_{J} x_J H_{sol(J)} \qquad eq. IV - 4$$

with $H_{sol(J)}$ the enthalpy of the solutions after equilibration. For the LiTFSI-LiCl-water system, the heat measured by calorimetry for a reference experiment reveals no heat exchange when the biphasic system is separated at 25°C and mixed at the same temperature of 25°C (**Fig. IV-3a**). However, an exothermic reaction is measured for the biphasic system separated at 25°C and mixed at 2°C (**Fig. IV-3b**), hence revealing a negative partial mixing enthalpy $\Delta_{mix}H'$ confirming that the LiTFSI-LiCl-water system is a T_{LC} system.

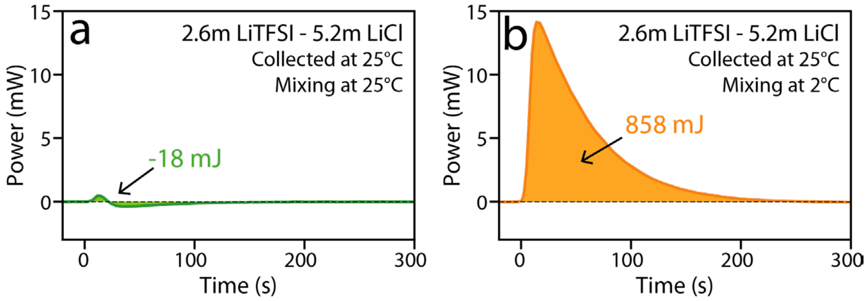

Fig. IV-3. Calorimetry measurements and partial mixing enthalpy for the 2.6m LiTFSI – 5.2m LiCl system. a, TFSI-rich and TFSI-poor phases are collected at 25°C and titrated at 25°C at which both solutions are immiscible. **b**, TFSI-rich and TFSI-poor phases are collected at 25°C and titrated at 2°C at which both solutions are miscible.

Next, VT-NMR was used to provide spatially resolved information across the ABS interface and to assess the ion partition as function of temperature (**Fig. IV-4** and z-axis calibration in **S-IV**: **Fig. IV-S1**). At 35°C, the intensity profile for ^{19}F shows a sharp difference across the interface, with more $TFSI^-$ found in the bottom phase than in the top phase (**Fig. IV-4** - right panels in red), in agreement with the infrared spectroscopy data (**Fig. IV-2e and 2f**). Similarly, the intensity profiles for ^{7}Li and ^{1}H show the top phase, *i.e.* the TFSI-poor one, to be richer in lithium and protons. By lowering the temperature to 20°C, the partitions for Li^+ and $TFSI^-$ ions and for water decrease (**Fig. IV-4** - middle panels in yellow). Finally, at 1°C, the system is monophasic and the solution is found to be homogeneous (**Fig. IV-4** - left panels in blue). Therefore, the ion partition decreases when decreasing the temperature, eventually crossing the binodal curve and forming a monophasic system at low temperature. For systems far from the binodal curve, *i.e.* 5m LiTFSI – 10m LiCl, much larger ion and water partitions are recorded at room temperature, as seen in **Fig. IV-2c and 2d**, and no transition from biphasic to monophasic was observed between -15°C and 80°C.

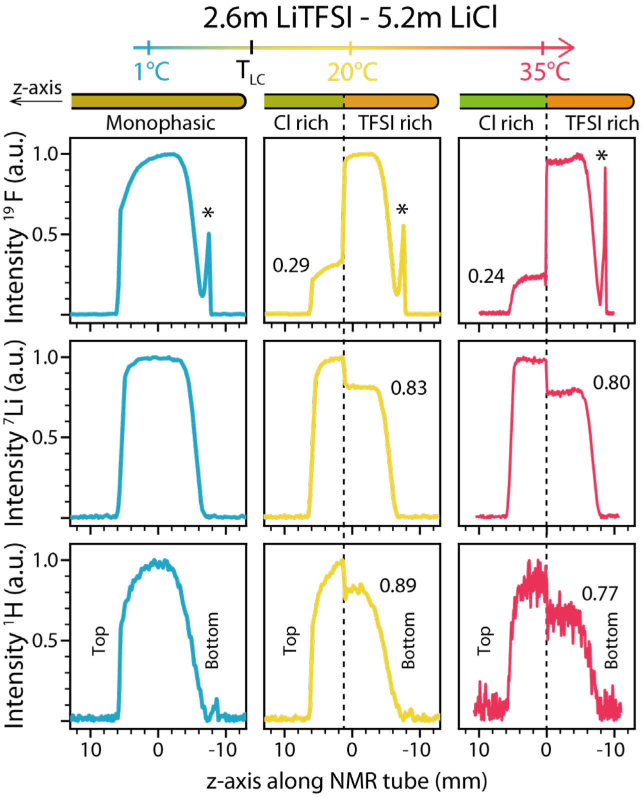

Fig. IV-4. Variable temperature nuclear magnetic resonance analysis of the 2.6m LiTFSI - 5.2m LiCl system at 1°C (blue), 20°C (yellow) and 35°C (red) for the nucleus ^{19}F (top), ^{7}Li (middle) and ^{1}H (bottom) along the height of the NMR tube from left (top of the tube) to right (bottom of the tube).

IV.C. Physical properties of the LiTFSI-LiCl-water system interface

In order to gain a microscopic understanding of the interface composition, Raman imaging was performed (lateral resolution ≈300 nm; axial resolution ≈800 nm, spectral resolution ≈15 cm^{-1}), taking advantage of the different phase-dependent vibrations for $TFSI^-$ anions and water. **Fig. IV-5a** shows the heat map of the integrated intensity of the $TFSI^-$ peak at ≈740 cm^{-1} for the 2.6m LiTFSI – 5.2m LiCl system, with increasing $TFSI^-$ concentration shown from blue to red. Comparing the Raman spectra collected across the interface (**Fig. IV-5b**) reveals a continuous change of the spectra, indicating a gradient of chemical compositions and solvation environments (behavior also seen in **Fig. IV-5c** for OH vibrations).

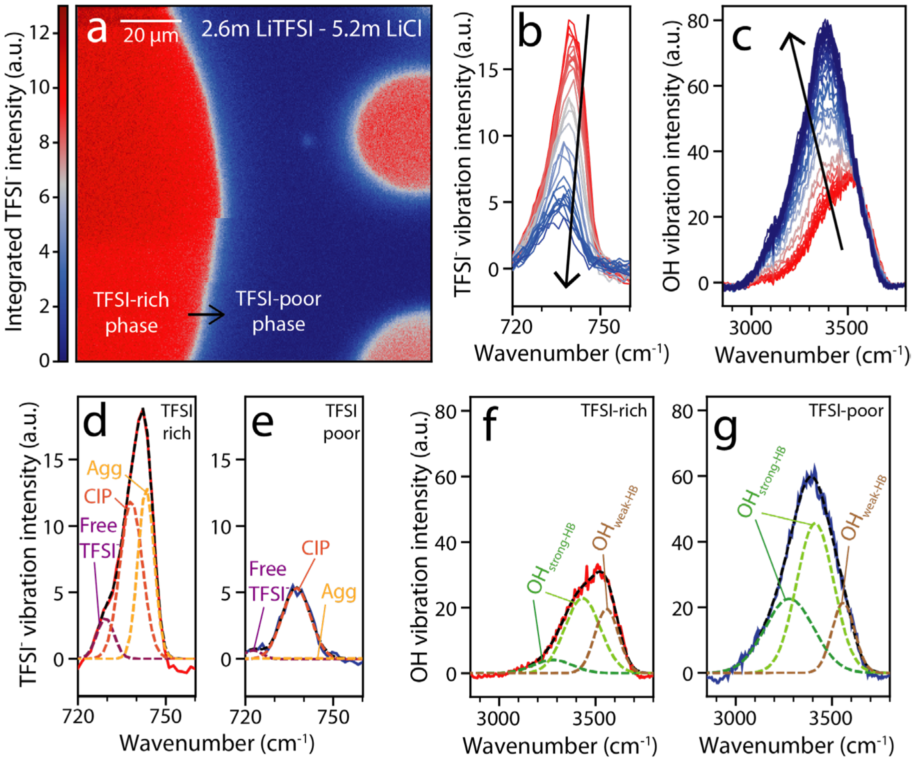

Fig. IV-5. Raman imaging across the interface of the 2.6m LiTFSI – 5.2m LiCl system. a, Raman imaging of the 2.6m LiTFSI – 5.2m LiCl system generated by integration of the TFSI⁻ vibrations. A slight movement of the liquid during imaging results in a partial shift in the image (≈50 µm from bottom); the top and bottom parts of the image are hence not compared. **b-c**, Raman spectra collected across the interface for TFSI⁻ vibrations (**b**) and for OH vibrations (**c**) of the 2.6m LiTFSI – 5.2m LiCl system. The color of plots matches that in (**a**). **d-e**, Peak decomposition of the TFSI⁻ vibrations in the TFSI-rich phase (**d**) and TFSI-poor phase (**e**) of the 2.6m LiTFSI – 5.2m LiCl system. **f-g**, Peak decomposition of the OH vibrations in the TFSI-rich phase (**f**) and TFSI-poor phase (**g**) of the 2.6m LiTFSI – 5.2m LiCl system.

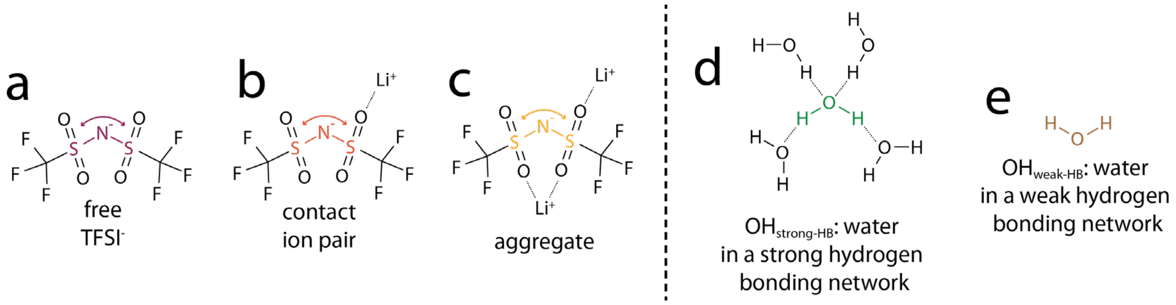

Fig. IV-6. Cartoon of the spectral components for the TFSI⁻ vibrations (left) and OH vibrations (right). a, TFSI⁻ vibrations in the case of the "free" TFSI⁻ (725 cm⁻¹). **b,** TFSI⁻ vibrations in the case of mono-coordinated TFSI⁻ i.e. contact ion pair (738 cm⁻¹). **c,** TFSI⁻ vibrations in the case of bi-coordinated TFSI⁻ i.e. aggregate (743 cm⁻¹). **d,** OH vibrations of water molecules in a strong hydrogen bonding network (3365 and 3230 cm⁻¹). **e,** OH vibration of water molecules in a weak hydrogen bonding environment (3570 cm⁻¹).

The Raman spectra were deconvoluted into their respective components to obtain qualitative chemical insight into the changes occurring across the interface. Based on previous studies[173,175,176], the $TFSI^-$ band can be decomposed into three components: free, mono- or bi-coordinated $TFSI^-$ ions as schematized in **Fig. IV-6a, 6b and 6c** respectively. The TFSI-rich phase is mostly composed of components corresponding to mono- (contact ion pairs (CIP), 738 cm^{-1}) and bi-coordinated (aggregates (Agg), 743 cm^{-1}) $TFSI^-$ ions with a limited contribution from "free" $TFSI^-$ ions (725 cm^{-1}) (**Fig. IV-5d** and in **S-IV**: **Fig. IV-S2**). Moving from the TFSI-rich phase (**Fig. IV-5d**) to the TFSI-poor phase (**Fig. IV-5e**), the intensity of the bi-coordinated component gradually drops alongside that of the free $TFSI^-$ component, while the intensity of the mono-coordinated $TFSI^-$ component is still present but at a lower intensity (**Fig. IV-5e** and in **S-IV**: **Fig. IV-S2**).

Similarly, the OH band can be decomposed into several components[171–173,177–179]. Using the simplest model that fits our data (in **S-IV**: **Fig. IV-S3**), the water spectra were fitted with three components (**Fig. IV-5f and 5g**). Two components at 3270 cm^{-1} and at 3430 cm^{-1} corresponding to the $OH_{strong\text{-}HB}$ interactions from the water hydrogen bonding network (**Fig. IV-6d**), described in the literature as ice-like and ice-like liquid components[177,178] or as double and single H-bounded water molecules[179]. The last component at 3560 cm^{-1} is referred to in the literature as a liquid-like amorphous phase components[177,178] or water molecules without H-bound,[179] thus corresponding to $OH_{weak\text{-}HB}$ interactions (**Fig. IV-6e**) from a TFSI-rich environment. When crossing from the TFSI-rich (**Fig. IV-5f**) to the TFSI-poor phase (**Fig. IV-5g**), the intensity of the components associated with a strong hydrogen bonding between water molecules increases ($OH_{strong\text{-}HB}$, low wavenumber components), while the intensity of the component associated with weaker water interactions remains approximately constant ($OH_{weak\text{-}HB}$, high wavenumber component) (in **S-IV**: **Fig. IV-S2**). Together, the Raman peak deconvolutions reveal that the interface is composed of a continuum of solvation environments gradually switching from a solvation structure previously ascribed to water-in-salt electrolytes (TFSI-rich phase with weak hydrogen bonding between water molecules and with $TFSI^-$ aggregates) to that of a more classical salt-in-water electrolyte (TFSI-poor phase with a stronger hydrogen bonding network between water molecules and without $TFSI^-$ aggregates). We note that as the polarization of our pump and detected Raman light is poorly defined (owing to imaging with high numerical apertures) we refrain from more quantitative analysis.

By plotting the normalized integrated Raman intensity variation and peak decomposition parameters across the interface for TFSI$^-$ and OH vibrations, a sigmoidal curve is obtained (**Fig. IV-7b** and in **S-IV**: **Fig. IV-S2**). This observation suggests that both the solvent, *i.e.* water, and one of the solutes, *i.e.* TFSI$^-$ anions, have a negative adsorption at salt-salt ABSs interface (**eq. IV-2** and **Fig. IV-1b**). More importantly, the thickness of the ABS interface is deduced by measuring the length over which the negative adsorption takes place, which is estimated by the distance necessary to increase from 10% to 90% of the normalized integrated Raman intensity. For the 2.6m LiTFSI – 5.2m LiCl system, the thickness is estimated to be 9.1 µm and 11.3 µm from the OH and the TFSI$^-$ vibrations, respectively.

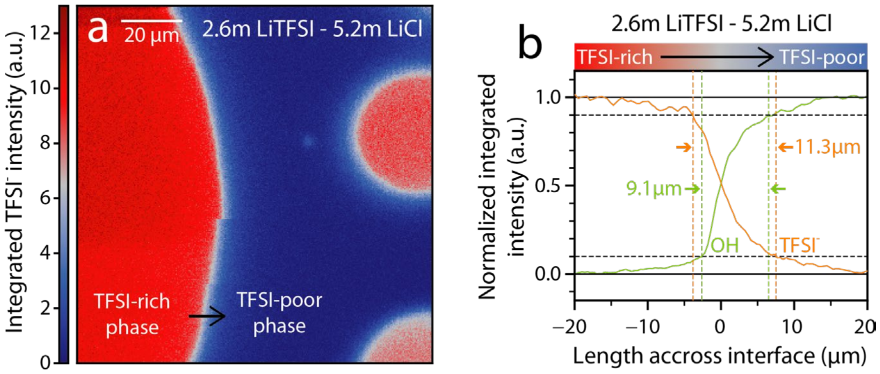

Fig. IV-7. Raman imaging across the interface of the 2.6m LiTFSI – 5.2m LiCl and 3m LiTFSI – 6m LiCl systems. a, Raman imaging of the 2.6m LiTFSI – 5.2m LiCl system generated by integration of the TFSI$^-$ vibrations. A slight movement of the liquid during imaging results in a partial shift in the image (≈50 µm from bottom); the top and bottom parts of the image are hence not compared (same as in **Fig. IV-5a**). **b**, The normalized intensity of OH (green) and TFSI$^-$ (orange) vibrations across the interface of the 2.6m LiTFSI – 5.2m LiCl system following the black arrow in (**a**).

The estimated thickness was found to be stable over hours and between multiple samples, reflecting a steady state (in **S-IV**: **Fig. IV-S4**). Such a large thickness cannot be explained by the existence of thermal capillary waves whose height we estimate to be of only several nanometers[66] (in **S-IV**: **Fig. IV-S5**). Nor can such a large thickness be a result of droplet curvature, refractive index mismatches[180] or limitations in our lateral resolution (≈800 nm). Indeed, we are able to measure molecularly sharp ITIES such as water-hexanone[181] (**Fig. IV-8**) or water-dichloroethane[60,68,70,164] (in **S-IV**: **Fig. IV-S6**) down to a size of ≈1 µm. Furthermore, the curvature of the interfaces is far larger (ten times) than the axial resolution of our laser system (≈800 nm) as shown in **S-IV**: **Fig. IV-S7** where a 3D reconstruction of the different phase regions is built.[182] Consequently, the interfaces can be approximated as a vertical slab with thickness effects ignored.

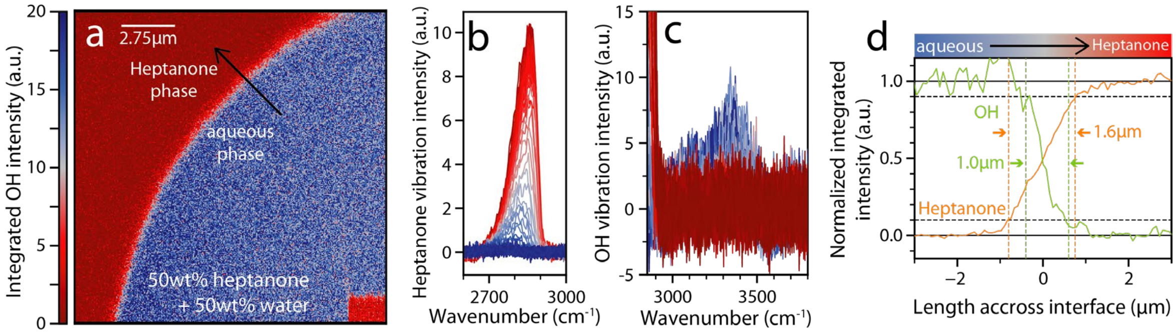

Fig. IV-8. Raman imaging across the heptanone-water interface. a, Raman imaging of a system composed by 50wt% of heptanone and 50wt% of Milli-Q water generated by integration of the OH vibrations. **b-c**, Raman spectra collected across the interface for the heptanone C-H stretching (**b**) and for OH vibrations (**c**). The color of plots matches that in (**a**). **d**, The normalized intensity of OH (green) and DCE (orange) vibrations across the interface. The size of the measured interface for the above mixtures is ≈1 µm. In light of our axial resolution (800 nm), lateral resolution (300 nm), the droplet curvature and small (< 1%) refractive index variations between the phases, we believe ≈1 µm represents the minimum extractable thickness from our approach.

Having postulated the negative adsorption of TFSI$^-$ anions and water molecules at the interface of a system close to the binodal curve, similar studies were carried out for systems with greater concentrations. For a 3m LiTFSI – 6m LiCl system (**Fig. IV-9**), a gradual change in solvation environment is observed when crossing the interface, similar to that of the 2.6m LiTFSI – 5.2m LiCl system. The sigmoidal curve observed for the integrated intensity (**Fig. IV-9d**) again suggests the negative adsorption of both TFSI$^-$ and water even at higher molalities. The thickness of the interface was estimated to be 2.7 µm and 4.3 µm from the OH and the TFSI$^-$ vibrations, respectively, smaller than previously measured for the 2.6m LiTFSI – 5.2m LiCl system (**Fig. IV-7b**). Systems with greater concentrations are reported in **S-IV**: **Fig. IV-S8**, showing an interface of about 3 µm and 2.5 µm for the 4m LiTFSI – 8m LiCl system and 5m LiTFSI – 10m LiCl system, respectively. Overall, we establish that for a system with a T_{LC}, by increasing salt molalities, *i.e.* moving away from the binodal curve, the interface gets thinner from about 10 µm down to the resolution of our measurement of a few microns.

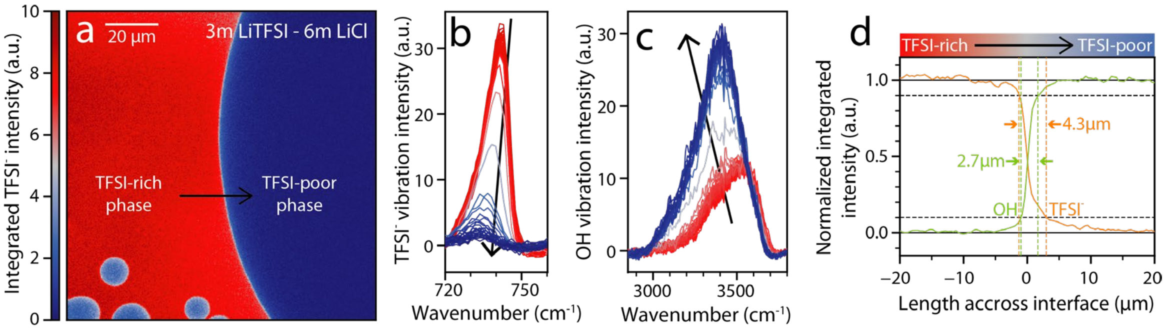

Fig. IV-9. Raman imaging across the interface of the 3m LiTFSI – 6m LiCl system. a, Raman imaging of the 3m LiTFSI – 6m LiCl system generated by integration of the TFSI$^-$ vibrations. **b-c**, Raman spectra collected across the interface for the TFSI$^-$ vibration (**b**) and for OH vibrations (**c**) of the 3m LiTFSI – 6m LiCl system. The color of plots matches that in (**a**). **d**, The normalized intensity of OH (green) and TFSI$^-$ (orange) vibrations across the interface of the 3m LiTFSI – 6m LiCl system.

IV.D. Interface for upper critical solution temperature: the LiTFSI-HCl-water system

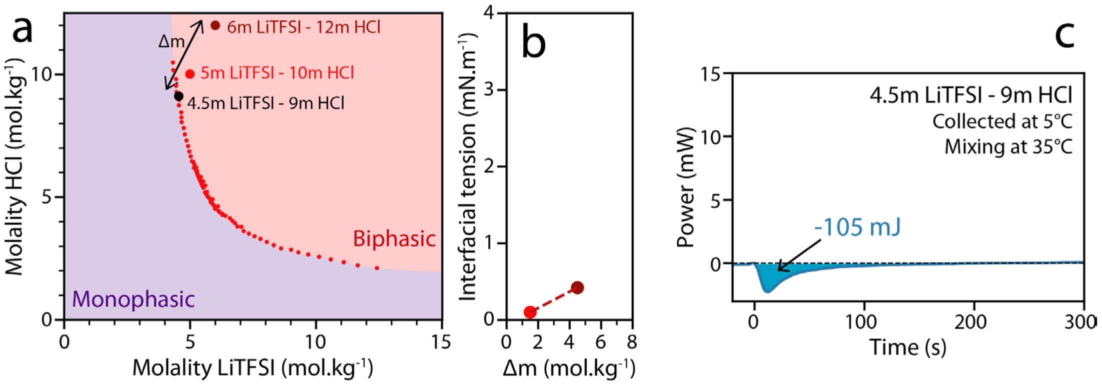

Fig. IV-10. LiTFSI-HCl-water system description. a, Phase diagram of the LiTFSI-HCl-water system with in purple the monophasic region and in red the biphasic region. Xm LiTFSI - Ym HCl systems are studied along the line 2X=Y, as indicated with black, red and dark red dots. Along this line, the binodal curve is crossed at 4.5m LiTFSI – 9m HCl. **b**, Interfacial tensions for the LiTFSI-HCl-water system as function of the salts total molality differential to the binodal curve in moles per kg (Δm) *i.e.* Δm=(X+Y)-(4.5+9). **c**, Calorimetry measurement and partial mixing enthalpy for the 4.5m LiTFSI – 9m HCl system with the TFSI-rich and TFSI-poor phases being collected at 5°C and titrated at 35°C at which both solutions are miscible.

The results from the LiTFSI-LiCl-water system were then compared with those for LiTFSI-HCl-water system (**Fig. IV-10a and 10b**) where VT-NMR (in **S-IV**: **Fig. IV-S9**) and reaction microcalorimetry (**Fig. IV-10c**) measurements reveal an upper critical temperature (T_{UC})[163,174], *i.e.* the system becomes miscible upon heating with the mixing being endothermic thus having a positive partial mixing enthalpy. Intermolecular interactions, and especially differences in hydrogen bounding network, are believed to explain the T_{LC} or T_{UC} behavior.[183] However, more precise understanding is lacking to directly relate T_{LC} or a T_{UC} behavior with the hydrogen bounding network. Thus, to date, it is not clear why switching from alkali cation (Li^+) to protons triggers a change from T_{LC} to T_{UC} in our systems while other systems keep a T_{LC} for both alkali cation (Na^+) and protons.[184]

As for the LiTFSI-LiCl-water systems, Raman imaging carried out on flat interfaces reveals that the solvation environment changes gradually over a few microns from one phase to the other (**Fig. IV-11**). Going from the TFSI-rich to the TFSI-poor phase, the spectral components at lower frequency, corresponding to strong hydrogen bonding, are found to increase for OH vibrations (**Fig. IV-11c** and in **S-IV**: **Fig. IV-S10**) along with an increase of the high frequency components corresponding to mono- and bi-coordinated TFSI$^-$ anions (**Fig. IV-11b** and in **S-IV**: **Fig. IV-S10**). The concentration-position profile for TFSI$^-$ anions and water across the interface are both found to be sigmoidal in shape (**Fig. IV-11d**). Hence, independent of whether a given system has a T_{LC} or a T_{UC}, a negative adsorption is suggested for the solute and the solvent. Repeating measurements at different concentrations, it is found that the interfacial thickness decreases with increasing molality from ≈5 µm for 5m LiTFSI – 10m HCl system (**Fig. IV-11d**) down to ≈2 µm for 6m LiTFSI – 12m HCl system (in **S-IV**: **Fig. IV-S11**) alike for the LiTFSI-LiCl-water system.

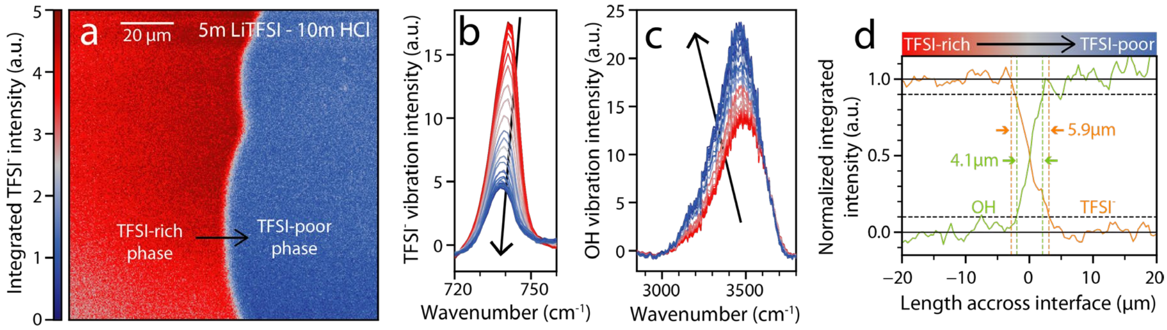

Fig. IV-11. Raman imaging across the interface of the 5m LiTFSI – 10m HCl system. a, Raman imaging of the 5m LiTFSI – 10m HCl system generated by integration of the TFSI$^-$ vibrations. **b-c**, Raman spectra collected across the interface for the TFSI$^-$ vibrations (**b**) and for OH vibrations (**c**) The color of plots matches that in (**a**). **d**, The normalized intensity of OH (green) and TFSI$^-$ (orange) vibrations across the interface.

Our results show that, unlike ITIES, salt-salt ABSs interfaces cannot be considered as molecularly sharp interface. Rather, they are microns-thick interphases forming a continuous gradient between both liquid phases. Given that the interfacial tension of salt-salt ABSs (about few mN.m^{-1}) lies between that of ITIES (tens of mN.m^{-1}) and polymer-polymer ABSs interfaces (hundreds of µN.m^{-1}) which both have interfaces on the sub-300 nm scale, our results show that salt-salt ABSs are outliers. Based on our findings, models that have been developed for ITIES using molecular isotherms, which link molecular interactions, surface tension and interfacial thickness hence do not appear appropriate for describing ABS. One way to qualitatively reconcile our observations is *via* the Gibbs adsorption equation (**eq. IV-1**) which does not take interfacial thickness or molecular interactions into account. Thus, when transitioning from a dilute regime to a concentrated regime, as it is the case for both the LiTFSI and LiCl solutions studied in **Chapter II** and in this chapter, the activity of water decreases unlike the activities of ions that are increasing, as previously shown for Li^+ activity in both LiTFSI and LiCl solutions[139] and for LiTFSI/LiBETI solutions,[27] as well as plotted for LiCl[144,185,186] in **Fig. IV-12**. Furthermore, the increase of the salt activity with concentration is much greater than the decrease of the activity of water. Hence, according to the Gibbs adsorption equation (**eq. IV-1**), and bearing in mind that our results suggest a negative adsorption of species at the interface ($\Gamma_S < 0$) and that the surface tension increases with the salt concentration, one can thus conclude that the change in surface tension is dominated by the increase of the activity of ions rather than by the decrease of the activity of water.

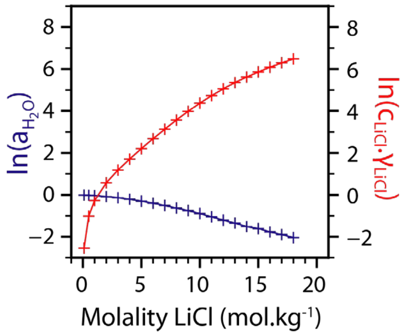

Fig. IV-12. Comparison of the activities in concentrated LiCl solutions. Activity changes of water from Robinson *et al.*[143] ; activity changes of (Li^+ ; Cl^-) salt dissolved with mean activity coefficient from Hamer *et al.*[184] ; densities from Abdulagatov *et al.*[185]. Similar trends are observed independently of the salt anion, and LiTFSI solutions show similar increase in salt activity concomitant with a decrease in water activity.

However, such conclusion should be used with care as information below the micrometer scale cannot be accessed with our Raman imaging (**Fig. IV-8** and in **S-IV**: **Fig. IV-S6**). More precisely, a very thin adsorption layer can still exist at the nanometer scale within the sigmoid observed by Raman imaging. In fact, such discrepancy was previously observed for the double layer formed between a conductive electrode and ionic liquids.[187,188] Further studies are thus necessary to understand the exact nature of the electrochemical double layer at the liquid/liquid interface formed in ABS.

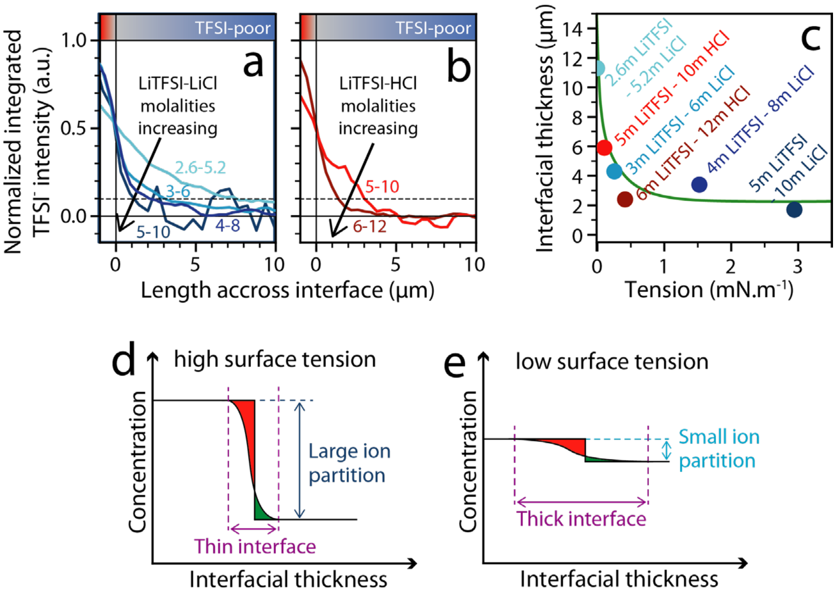

Fig. IV-13. Evolution of interfacial thickness as function of molality and surface tension. a-b, Comparison of the integrated intensity for $TFSI^-$ vibrations for different LiTFSI-LiCl-water systems (**a**) and LiTFSI-HCl-water systems (**b**). **c**, Interfacial thickness as function of the interfacial tension for the LiTFSI-LiCl-water and LiTFSI-HCl-water systems studied in this work. The green line is only a guide to the eye. **d-e**, Schematic depicting the concentration profile of solutes across an interface for high (**d**) and low (**e**) surface tension. Green and red represent, respectively, positive and negative integrals when compared to a step change of concentration.

Summarizing the different systems studied in this work, we find that the thickness of the interface is decreasing with both total molality (**Fig. IV-13a** and **13b**) and surface tension (**Fig. IV-13c**). For large molality, *i.e.* for high surface tension (**Fig. IV-13d**), we observe large ion partitioning while Raman imaging reveals thin interfaces. Decreasing the molality, *i.e.* for lower surface tension, the ion partitioning is smaller but the thickness of the interface increases (**Fig. IV-13e**). However, a more quantitative interpretation of the Gibbs adsorption equation, relating surface excess to surface tension, requires a simultaneous knowledge of the concentration profiles for all species, currently out of reach for ions such as Cl^- or Li^+ using Raman imaging.

IV.E. Chapter conclusions

In summary, with microscopic chemical resolution, we have directly imaged the interface formed for salt-salt ABSs as a function of concentration. Our study reveals, unlike for ITIES or polymer ABSs, very large interfacial thicknesses up to 10 µm. The thickness correlates inversely with the salts concentration and the interfacial tension. Using Raman spectroscopy, the molecular bonding environment across the interfaces was probed, demonstrating a gradual change in water structure from an environment in which the hydrogen bonding network is weak and anions aggregates exist (TFSI-rich phase) to an environment resembling more of a dilute aqueous solution (Cl-rich phase). This result highlights that both LiCl and LiTFSI are important to generate different environments resulting in the phase separation. In addition, using NMR and calorimetry methods, we dynamically probed the effect of temperature on the miscibility of salt-salt ABSs. Comparing LiTFSI-LiCl-water and LiTFSI-HCl-water systems, we find that changing the cation from Li^+ to H^+ inverts the temperature-dependence, with the former becoming miscible upon cooling below room temperature while the latter becomes immiscible. Nevertheless, such opposing behavior does not dramatically change the thickness of the interface, which remains in the 1-10 µm range. Considering a negative adsorption for both water and solutes at the interface, we find that ion partitioning increases with salt concentration. We postulate that the formation of the interface is dictated by the increased activity of solute ions with concentration. One important question nevertheless remaining relates to how the nature of the cations influences temperature dependence of the phase diagram for salt-salt ABSs. Hence, following the insights provided by our findings, better theoretical understanding of ABSs is still needed. Indeed, the surface tension of salt-salt ABSs lies between that of ITIES and of polymer-polymer systems, yet they show much larger interfaces, beyond access for classical molecular dynamics simulations. Understanding further how the properties and size of the interfaces can be tuned is not only of fundamental interest but crucial if ABSs systems are to be used for electrochemical devices[7,52,76,77,158], chemical separation/purification steps[189], carbon capture[190] or in multiphase catalytic applications[191].

Generally, probing liquid-liquid interfaces in systems—be they electrochemical, biological or otherwise—has remained challenging. Our results demonstrate the power of Raman imaging, particularly over other popular optical imaging methods such as reflection/scattering microscopy, for providing label-free microscopic chemical information especially in material science applications. Combining such techniques with super-resolution[192] or tip-enhanced[193] approaches will allow access to the sub-100 nm resolution limit and broaden the set of systems that can be examined, *e.g.* polymer ABSs and phase separations at electrified interfaces. Combining more advanced Raman schemes (triple grating spectrometers, heterodyne optical Kerr effect[194]) with other techniques such as neutron reflectometry (especially deep inelastic neutron scattering)[195,196] and sum frequency generation[197,198] will be useful to gain an improved understanding of critical low-energy interactions such as hydrogen-bonds.

In parallel and complementary to spectroscopic studies, ABS interface should be studied with electrochemical tools. Taking inspiration from the work done for ITIES, capacitance measurement will help to better understand the distribution of ions at the aqueous-aqueous interface while studies of the polarization window and the kinetics of ions transfer will clarify the presence of eventual overpotential linked to ion transfer. The combination of these characterization techniques with novel chemistries will help unravel the structure, selectivity and ion transport properties of ABS interfaces, leading to new discoveries in the design of complex liquid electrolytes for membrane-less electrochemical devices.

Chapter V – Electrochemistry at ABS liquid-liquid interface

V.A. Introduction

Fundamental electrochemistry at liquid-liquid interface has been an essential tool when investigating ITIES, both to understand the composition of the interface, *e.g.* by using capacitance measurements, or to study the ion transfer *via* kinetics measurement. Thus the study of ABS can greatly benefit from adopting such measurements, where key knowledge on the structure and ion transfer kinetics of aqueous-aqueous interfaces can potentially be reached. Furthermore, such fundamental study of ion transfer at ABS interfaces is crucially lacking for the design of more efficient immiscible aqueous-based electrolytes for electrochemical devices. Hence, this chapter is dedicated to the study of liquid-liquid interfaces by electrochemistry.

Electrochemistry at liquid-liquid interfaces has classically been carried out either at macroscopic (mm- to cm-sized, **Fig. V-1a**) ITIES in four electrodes measurements, or alternatively in two electrodes setups at micro- (or even nano-) sized ITIES (**Fig. V-1b**).[199]

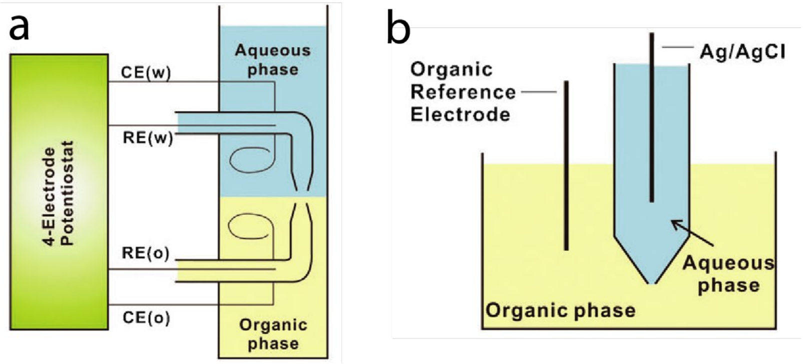

Fig. V-1. Schematics of the four electrodes and two electrodes cells commonly employed for electrochemical study at liquid-liquid interfaces. a, Schematic of the liquid-liquid electrochemistry at macroscopic interfaces using four electrodes, having in each phase, one reference electrode in a Luggin capillary and one counter electrode. **b**, Schematic of the liquid-liquid electrochemistry at microscopic interfaces using two electrodes, having in each phase, only one reference electrode also acting as counter electrode. Adapted from Liu *et al.*[199].

Macro-ITIES were used in pioneering works by Gavach *et al.*[61] and are still employed for electrosynthesis[168,200] at liquid-liquid interfaces. Besides the precision needed to design four electrode glass cells with precise positioning for reference electrodes, several groups also reported that two electrode measurements at micro-ITIES are more sensitive than four electrode measurements at macroscopic interfaces, thus being advantageous for analytical electrochemistry.[199,164,69,201] Indeed, the substantial resistance originating from the limited conductivity of the organic phases associated to the high current coming from the large surface of macroscopic interfaces lead to large ohmic drop, which is difficult to properly compensate.[199,201] Moreover, similarly to ultramicroelectrode (UME) at solid-liquid interfaces, micro-ITIES can have a spherical diffusion of species enabling to reach steady state currents which are easier to interpret compared to the peak of a linear diffusion such as that obtained with macro-ITIES.[164] Hence, following these previous reports and our goal to study the structure and ion transfer kinetics at liquid-liquid interface, our efforts were paid at studying microscopic interfaces in two electrodes setup.

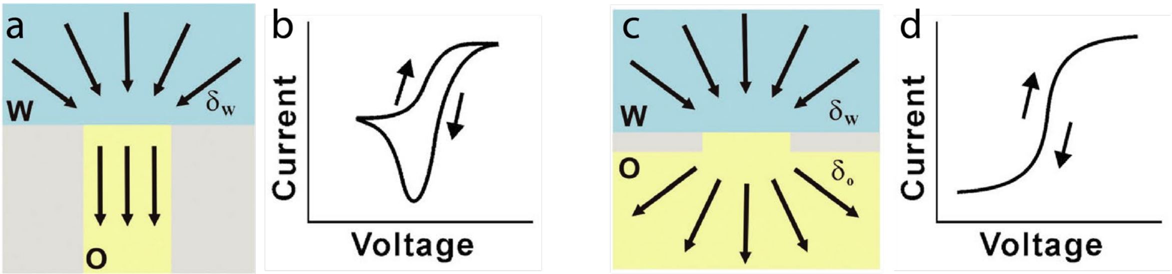

Fig. V-2. Schematics and illustration of the liquid-liquid electrochemistry in micro-pipettes and micro-holes. a-b, Schematic of the spherical diffusion outside of the micro-pipette and linear diffusion inside a micro-pipette (**a**) along with the corresponding cyclic voltammetry showing negative peak for the transfer of ion from the organic phase in the micro-pipette to the aqueous phase while a positive steady-state diffusion limited current is obtained for the transfer of ion from the aqueous phase outside of the micro-pipette to the organic phase (**b**). **c-d**, Schematic of the spherical diffusion on both sides of a micro-hole (**c**) along with the corresponding cyclic voltammetry showing both positive and negative steady-state diffusion limited currents for the transfer of ion from the organic phase to the aqueous phase, and *vice versa* (**d**). Adapted from Liu *et al.*[199].

To form micro-ITIES, two main strategies were developed, with either the use of micro-pipettes (**Fig. V-2a**) or of micro-holes formed in inert films (**Fig. V-2c**).[199,202] The use of micro-pipette was first proposed by Girault *et al.*[203] who highlighted the interest of having linear and spherical diffusion regimes, respectively from the inside or the outside of the micro-pipette. Indeed, the walls of the pipette dictate a linear regime for species diffusing from the inside to the outside, leading to a current peak (**Fig. V-2b** – negative peak) dependent on the scan rate of the cyclic voltammetry and described by the Randles-Ševčík equation, similarly to macroscopic solid-liquid interfaces:

$$i_p = 0.4463 \left(\frac{F^3}{RT}\right)^{1/2} z^{3/2} \, (vD_X)^{1/2} \, C_X \pi r^2 \qquad eq.V-1$$

with z the charge of ion X, D_X the diffusion coefficient of ion X and C_X the concentration of ion X, R the molar gas constant, T the temperature, F the faraday constant and r the inner radius of the micro-pipette.[39]

On the contrary, species diffusing from the outside to the inside of the micro-pipette have a spherical diffusion, leading to a steady-state diffusion limited current (**Fig. V-2b** – positive plateau) according to the following equation[202]:

$$i_d = 4zFD_XC_Xr \qquad eq.V-2$$

Thus, it is possible to distinguish by the shape of CVs if species are diffusing from the aqueous to the organic phase or, on the contrary, from the organic to the aqueous phase (**Fig. V-2b**). However, short shank micro-pipettes are necessary in order to minimize the length l of low radius (r) section of the pipette so that lower resistance (R) can be achieved following the equation:[39]

$$R = \frac{l}{\kappa \pi r^2} \qquad eq.V-3$$

Indeed, taking a section of 10 µm in radius and 1 mm in length with an electrolyte having a 100 mS.cm^{-1} conductivity, such as the aqueous electrolytes typically studied in this work, we estimate a resistance of ≈10^6 Ω, leading to ≈1 mV ohmic drop with currents as low as 1 nA. The fabrication of appropriate micro-pipettes can be realized by glass pipette pulling according to carefully adjusted pulling parameters[199] or by machining low diameter polyetheretherketone (PEEK) capillaries to enlarge the diameter of the capillary on most of its length leaving only a short end of the low diameter section (**Fig. V-3**). However, in both cases, it is challenging to achieve a low diameter section that is short enough to minimize the resistance while being repeatable. Owing to our lack of access to the proper tools to performed glass pipette pulling or machining PEEK capillaries, attempts at making such devices were not successful.

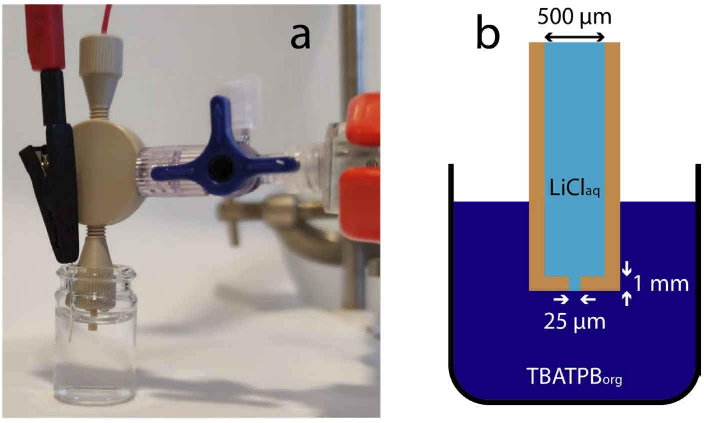

Fig. V-3. Description of the micro-pipette liquid-liquid electrochemical cell using a capillary. a, Picture of the assembled liquid-liquid cell from the side. **b**, Scheme of the 25 µm diameter capillary machined to enlarge to 500 µm most of its length leaving only a short length at 25 µm.

With this limitations in mind, our efforts were thus paid on developing a two electrodes cell using micro-holes made in Kapton polyimide films via laser ablation, as previously reported.[69] Doing so, the resistance is minimized by having a low radius (10 µm) section of only the Kapton film thickness, *e.g.* ≈10 µm in length, leading to a resistance of about ≈10^4 Ω according to **eq. V-3**. However, as the length of the hole has typically a similar or smaller size than the hole radius that is in the order of few dozens of microns (see next section), linear diffusion does not take place anymore and a spherical diffusion occurs on both sides of the micro-hole (**Fig. V-2c**). This leads to a steady-state current for both ions transferring from the aqueous to the organic phase, or *vice versa* (**Fig. V-2d**). Nevertheless, the micro-hole configuration turns out to be more convenient, as repeatable size of holes and thickness of Kapton film can be easily achieved (see below). Thus, the following part describes in details the cell developed in this work, as well as benchmark electrochemical measurements carried out at micro-hole supported liquid-liquid interfaces using well-known ITIES.

V.B. Description of the Liquid-Liquid electrochemical cell

Based on the cell reported by Girault and co-workers[69], and in collaboration with Romain Dugas, we designed a horizontal PEEK cell with two symmetrical compartments (**Fig. V-4a, 4b and 4c**) separated by a ring holding a Kapton film in which a micro-hole was made by laser ablation (**Fig. V-4d, 4e and 4f**). Each compartment contains one phase of the biphasic system and an AgCl/Ag wire electrode, which is placed close to the Kapton film (**Fig. V-4c**), forming a two electrodes configuration.

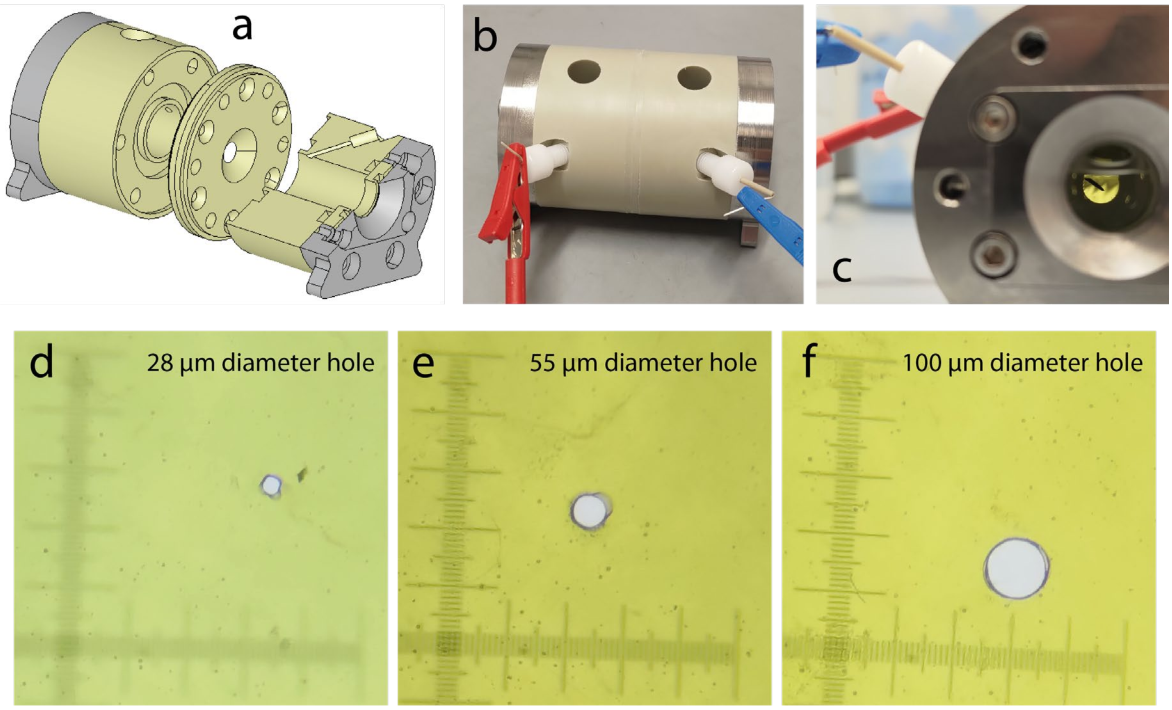

Fig. V-4. Description of the micro-hole liquid-liquid electrochemical cell and microscope images of holes made by laser ablation. a, Three-dimensional drawing of the liquid-liquid cell. A cut of the front compartment was made to show the path of the AgCl/Ag wire electrode. **b**, Picture of the assembled liquid-liquid cell from the top. **c**, Picture of the assembled liquid-liquid cell from the side showing the AgCl/Ag wire near the Kapton film through the cell window. **d-f**, Measurement of the 28 µm (**d**), 55 µm (**e**) and 100 µm (**f**) holes made by laser ablation in Kapton film.

To confirm the reliability of our setup, we carried out measurements using the well-known ITIES formed between LiCl in water and TBATPB in DCE already taken as an example in **Chapter I**, part **I.C.** By increasing the hole diameters from 28 µm to 55 µm and 100 µm (**Fig. V-4d, 4e and 4f**), we observe a proportional increase in the steady-state diffusion limited current of the TPB$^-$ transfer from the organic to the aqueous phase at $\Delta\phi^{aq\rightarrow org}$ ≈0.5 V, from 6.1 nA to 11.6 nA and 21.5 nA, respectively (**Fig. V-5a**). This confirms the proportional scaling of the limiting current with the radius with a slope of 0.21 nA.µm^{-1} (**Fig. V-5b**), in agreement with **eq. V-2** having a coefficient of $2zFD_{TBP^-}C_{TBP^-}$ = 0.135 nA.µm^{-1}, taking D_{TBP^-} = 0.7 10^{-9} m^2.s^{-1} and C_{TBP^-} = 1 mM.[204]

By increasing the scan rate from 10 mV.s^{-1} to 50 mV.s^{-1} (**Fig. V-5c**), the CVs for the 55 µm and 100 µm holes do not present a steady-state diffusion limited current (**eq. V-2**), but rather a current peak (**eq. V-1**). This means that at 50 mV.s^{-1}, the measurements carried with the 55 µm and 100 µm holes tend to have linear diffusion. To keep a spherical diffusion, the following condition on the scan rate needs to be met:

$$v \ll \frac{RTD_X}{zFr^2} \qquad eq.V-4$$

To match this condition, the scan rate needs to be kept lower than 24 mV.s^{-1} and 7 mV.s^{-1} for the 55 µm and 100 µm holes, respectively, thus explaining the current peaks observed at 50 mV.s^{-1}. For the 28 µm hole, the condition for steady-state diffusion limited current is met up to 92 mV.s^{-1}, thus explaining that even at 50 mV.s^{-1}, the CV for the 28 µm present a steady-state diffusion limited current (**Fig. V-5c**). Thus, to match the condition of **eq. V-4**, the following experiments were performed at 10 mV.s^{-1} with the 28 µm hole.

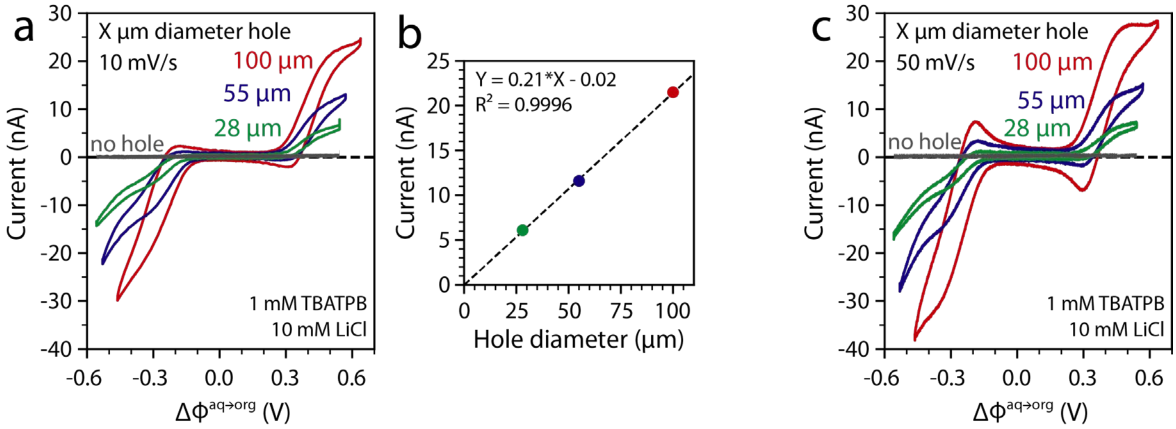

Fig. V-5. CVs for ITIES between LiCl in water and TBATPB in DCE. a, CVs at 10 mV.s^{-1} for ITIES supported by different hole sizes (28 µm in green, 55 µm in blue and 100 µm in red) between 10 mM LiCl in water and 1 mM TBATPB in DCE. **b**, Correlation curve between hole diameters and the steady-state diffusion limited current. **c**, CVs at 50 mV.s^{-1} for ITIES supported at different hole sizes between 10 mM LiCl in water and 1 mM TBATPB in DCE.

Next, we confirm the relationship existing between the limiting current and the TPB$^-$ concentration (**eq. V-2**) by varying the TPB$^-$ concentration from 1 mM to 10 mM (**Fig. V-6a**) and observing the current to increase from 6.1 nA to 43 nA. This increase does not exactly match the proportionality, but exhibits an increase of the right order of magnitude. Then, as expected, when changing the LiCl concertation from 10 mM to 1 mM (**Fig. V-6b**), the steady-state diffusion limited current of the TPB$^-$ transfer is not impacted and remains steady at about 6 nA. Similar results are obtained with the negative currents associated with the transfer of

TBA^+ from the organic to the aqueous phase at $\Delta\phi^{aq\rightarrow org}$ ≈ -0.3 V. However, the overlapping transfer of Cl^- from the aqueous to the organic phase at $\Delta\phi^{aq\rightarrow org}$ ≈ -0.5 V makes this phenomenon more difficult to quantify. Finally, in **Fig. V-6c** for tetramethylammonium chloride (TMACl) cation, we observe a positive current (in blue) with an onset at $\Delta\phi^{aq\rightarrow org}$ ≈0.1 V, *i.e.* at lower voltage than the transfer of TPB^- previously observed for LiCl at $\Delta\phi^{aq\rightarrow org}$ ≈0.3 V. This current can be attributed to the transfer of TMA^+ from the aqueous phase to the organic phase which matches both the standard ion-transfer potential of TMA^+ ($\Delta\phi^{\circ\,aq\rightarrow org}_{X}$ = 160 mV)[64] and the magnitude order of the steady-state diffusion limited current estimated from **eq. V-2** to be $4zFD_XC_Xr$ = 70 nA with D_{TMA^+} = 1.2 10^{-9} $m^2.s^{-1}$ and C_{TMA^+} = 10 mM.[16] Overall, these measurements confirm the reliability of our micro-hole supported liquid-liquid electrochemical cell which was a crucial step toward studying ABS interfaces.

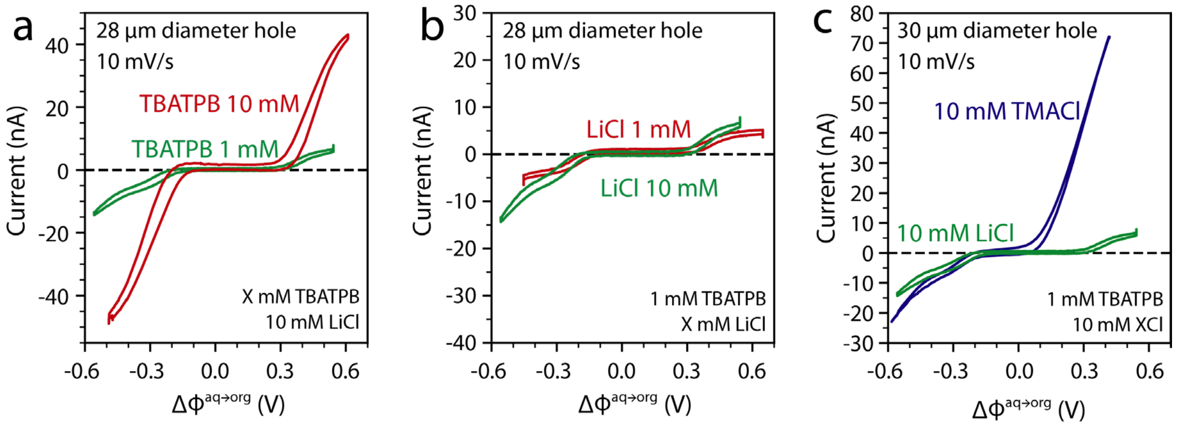

Fig. V-6. CVs at 10 mV.s^{-1} for ITIES supported by a 28 µm hole between LiCl in water and TBATPB in DCE. a, CVs for ITIES between 10 mM LiCl in water and either 1 mM (in green) or 10 mM (in red) TBATPB in DCE. **b**, CVs for ITIES between 1 mM TBATPB in DCE and either 10 mM (in green) or 1 mM (in red) LiCl in water. **c**, CVs for ITIES between 1 mM TBATPB in DCE and either 10 mM LiCl (in green) or 10 mM TEACl (in blue) in water.

V.C. Future directions for Liquid-Liquid electrochemistry at ABS interfaces

Having proved the reliability of our cell, the next step is to use the setup to study the ion transfer in ABS. Nevertheless, due to the lack of time, only very preliminary results were gathered thus far on ABS. Nevertheless, we aim at studying in the future the following. First, the study of the transfer of Li^+ across the liquid-liquid interface is necessary to understand the electrochemical behavior of ABS electrolytes when used in Li-based batteries. Indeed, Li^+ transfer from one liquid phase to the other is necessary during battery operation to ensure the electroneutrality of both phases of the ABS, as illustrated in **Fig. III-1**. Especially, with the aim of developing ABS membrane-less devices, one should clarify if the ion transfer at ABS interface is associated with an overpotential and an added resistance compared to a device using a membrane, *e.g.* Nafion. As Li^+ is common to both phases for LiTFSI-LiCl-water ABS, we can expect the interface of the ABS to be non-polarizable and thus having no overpotential for the transfer of Li^+. Preliminary results in **Fig. V-7** show the ABS interface does not present any polarization window and behaves as a resistance (R = 2.2 10^4 Ω) with similar value than expected from **eq. V-3** (R = 1 10^4 Ω). Thus, this current could correspond to the transfer of Li^+ from the Cl-rich phase to the TFSI-rich phase for positive current and *vice versa* for negative currents. The steady-state diffusion limited current can be estimated from **eq. V-2** to be $4zFD_{Li^+}C_{Li^+}r$ ≈ 10 µA for a 28 µm hole and with estimations of D_{Li^+} ≈ 5.10^{-10} $m^2.s^{-1}$ from Liu *et al.*[110] and C_{Li^+} ≈ 5 $mol.L^{-1}$. However, we could not see any limiting current in **Fig. V-7** up to 50 µA, highlighting the difficulties of studying ABS interface due to the incompatibility of a high resistance and a high concentration leading to high limiting currents.

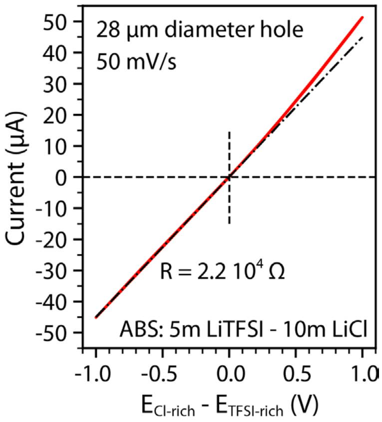

Fig. V-7. CVs at 50 $mV.s^{-1}$ for the 5m LiTFSI - 10m LiCl ABS interface supported by a 28 µm hole.

Concerning anions transfer, as the phase separation is driven by anions, we expect an overpotential for the transfer of halides from the halide-rich phase to the TFSI-rich phase, and similarly, for the transfer of $TFSI^-$ from the TFSI-rich phase to the halide-rich phase. Unfortunately, the anions transfer at the interface of ABS will probably be hidden by the current associated with Li^+ transfer, as previously mentioned. Moreover, the steady-state diffusion limited current for anions transfer as estimated from **eq. V-2** for a 28 µm hole and with estimations of D_{TFSI^-} ≈ 1.10^{-10} m^2.s^{-1} from Liu *et al.*[110] and C_{TFSI^-} ≈ 5 mol.L^{-1} is ≈1 µA. Hence for both anions and cations transfer, the high current driven due to the high salts concentrations combined with the resistance of the cell makes analytical studies of ion transfer at ABS interface challenging.

Thus, other means need to be found to study ion transfer. Coming back to ITIES, one way envisioned in the future is to study the transfer of TFSI$^-$ anions from an organic phase, such as TBATFSI in DCE, to an aqueous phase with increasing LiCl concentrations. Thanks to previous studies of the LiTFSI-LiCl-water ABS, an increased TFSI$^-$ transfer potential can be foreseen, linked to the difficulty of mixing TFSI$^-$ with Cl$^-$ when increasing the LiCl concentration. A symmetric study by having TBACl in DCE and transferring Cl$^-$ anions to an aqueous LiTFSI phase would be a good complementary study. However, it will not be possible in practice as ion exchange between TFSI$^-$ and Cl$^-$ will certainly take place, leading back to the speciation of TBATFSI in DCE and LiCl in water.

Expending our study beyond the LiTFSI-LiCl-water ABS, the next step will be to study the transfer of TFSI$^-$ from DCE to other lithium halides aqueous solutions such as LiBr or LiI, also known to form ABS with LiTFSI.[107] LiTFSI-LiX-water ABS with X = I, Br or Cl have similar phase diagrams, thus we expect the transfer of TFSI$^-$ from DCE to LiX aqueous solutions to be similar. More interestingly, on the one hand, TFSI$^-$ can be substituted by the larger anion Bis(pentafluoroethanesulfonyl)imide (BETI$^-$) for which the immiscible regime in the LiBETI-LiX-water phase diagram is formed at lower concentrations than with LiTFSI. Hence, transfer of BETI$^-$ from a TBABETI DCE phase to an aqueous LiX phase should in theory be more difficult than the transfer of TFSI$^-$. One the other hand, TFSI$^-$ can be replaced by the smaller anion bis(fluorosulfonyl)imide (FSI$^-$). In this case, no ABS is formed for the LiFSI-LiX-water system, thus one can expect an easier transfer of FSI$^-$ from a LiFSI DCE phase to an aqueous LiX phase compared to TFSI$^-$.

Pushing one step further, similar studies could be carried out to investigate the effect of cations, more specifically by changing lithium to other cations such as protons and studying the transfer of TFSI$^-$ from a TBATFSI in DCE phase to an aqueous HCl phase. Such study leans toward a better understanding of the cation effect responsible for both i) the difference of the phase diagram between the LiTFSI-HCl-water and the LiTFSI-LiCl-water and ii) the separation of cations within an ABS. Indeed, despite our attempts at understanding any effects related to differences in solvation structure by Raman spectroscopy, calorimetry and NMR (see **Chapter IV**), we could not explain the change from a T_{LC} to a T_{UC} when changing cations from a LiTFSI-LiCl-water to a LiTFSI-HCl-water system.

Overall, comparing anions transfer between DCE and aqueous phases could clarify the (in)compatibility of halides with FSI^-, $TFSI^-$ and $BETI^-$, and explain the formation of salt-salt ABS for which the phase separation is driven by anions but for which cations also influence the phase separation. Finally, liquid-liquid electrochemistry should not be limited to studying salt-salt ABS and should be extended to ionic liquid-salt ABS, polymer-salt ABS from which a global understanding of the compatibility of ions with salt, ionic liquid and polymer could help rationalizing the driving force for the formation of ABS.

General Conclusion and Perspectives

General Conclusion

Throughout this thesis, highly concentrated aqueous solutions were studied in order to expand the understanding of this new class of liquid electrolytes for which the (electro)chemistry is radically different when compared to diluted aqueous solutions. By increasing the concentration from diluted regimes to high concentrations, we highlighted large changes in redox potentials associated with reactions involving both cations (Li^+, H^+, Zn^{2+}) and anions (Cl^-, Br^-) as a results of changes in both ion activities and liquid junction potential. Unfortunately, liquid junction potential and individual ion activity coefficients are entangled when performing electrochemical measurements and they cannot be obtained independently, preventing the accurate calculation of ion-associated Nernst potentials. Most of the results in the literature swept this issue under the rug and the liquid junction potential is often, if not always, simply ignored. However, based on reasonable approximations, we unravel a non-negligible liquid junction potential. This result emphasizes how misleading can be the electrochemistry of highly concentrated solutions and thus extra care should be taken when performing and more importantly analyzing electrochemical measurements in highly concentrated solutions.

Being aware of the non-negligible liquid junction potential, we could nonetheless demonstrate that when moving from diluted regimes to highly concentrated electrolytes, the proton concentration increases by almost two orders of magnitude, thus making highly concentrated electrolytes slightly acidic. Such results regarding pH and activity of ions help to rationalize the competition between the hydrogen evolution reaction, dependent on the pH, and the intercalation of Li^+, dependent on the activity of Li^+, in aqueous battery based on highly concentrated electrolytes. We found that even for batteries using WiSE, water reduction is still thermodynamically favored compared to Li^+ intercalation in anode materials (e.g. graphite, lithium titanate oxide or Mo_6S_8 chevrel phase), explaining previous observations of hydrogen being evolved at the negative electrode during rest, inducing copious self-discharge.[31] Hence, the cyclability of batteries utilizing WiSE is not thermodynamically but rather kinetically allowed, as the high concentration of LiTFSI salts allows the formation of a SEI, which is however not stable on the long term, thus leading to self-discharge through the evolution of hydrogen.[30] Artificial SEI was proposed as providing more stability, nevertheless, the industrial relevance of this technology needs to be demonstrated, bearing in mind that we could never achieve artificial gel SEI with similar quality as previously reported in the literature[7,32]. Moreover, one of the major benefits of switching from organic to aqueous batteries is, in principle, to avoid the use of expensive dry rooms, which will not be avoided as the formation of the artificial SEI would probably need to be performed in dry rooms. Eventually, one can raise the question as to which extent this battery is still an aqueous one? Indeed, by having an artificial organic SEI and an electrolyte composed of 85 w% of an expensive organic salt and only 15 w% of water (for 20m LiTFSI), this battery can be considered as an organic battery with a hydrated ionic liquid electrolyte.[27] Thus, effort must still be paid at either developing diluted aqueous solutions or replacing LiTFSI by fluorine-free cheaper salts, or both. Overall, the right balance still needs to be found to have acceptable low voltage negative electrodes while still having the economic and safety advantages of truly aqueous batteries.

Turning to the positive electrode of aqueous batteries, we studied in this thesis the role of a LiTFSI-LiX-water ABS (with X = Br, Cl) toward the electrochemical intercalation of halogens into graphite. Building from the knowledge gathered from the activity of ions and liquid junction potential, we aimed at first understanding the competition between the different oxidation reactions of halogens, *i.e.* the halogens intercalation in graphite, the halogen gas evolution or also the formation of soluble species such as trihalides or halogen oxyanions. According to both thermodynamics and electrochemistry, the oxidation of halides at high concentration leads to the formation of trihalides in solution. However, we could prove that the intercalation of halogens into graphite takes place spontaneously in presence of trihalides, thus demonstrating a two-step intercalation of halogens into graphite through a trihalide intermediate in solution. More than just an intermediate, trihalides are very soluble in lithium halide solutions and thus participate to the total capacity of the battery by storing charges in the electrolyte, similarly to a redox flow battery. However, in a redox flow battery, expensive Nafion membranes are used to prevent self-discharge. We discovered that the ABS prevent self-discharge without the use of membranes, by forming two phases, one TFSI-rich phase in contact with the negative electrode, and one halide rich phase in contact with the positive electrode. Indeed, trihalides are found to be confined in the halide rich phase and immiscible in the TFSI-rich phase which, as a consequence, prevents the self-discharge via the crossing of trihalides to the negative electrode. Nevertheless, the ABS top phase being in contact with the positive electrode while the ABS bottom phase is in contact with the negative electrode, this system is easily disturbed by any movements, rendering this technology uniquely applicable to stationary application.

Hence, ABS are highly relevant to electrochemical devices such as redox flow batteries or even electrolysers. Indeed, these devices use expensive Nafion membranes to separate the electrolytes in contact with the positive and negative electrodes while, on the contrary ABS spontaneously forms two phases providing different chemical environments at the positive and negative electrodes. Having two environments provides ion partitioning, as illustrated with the tribromide being confined in the halide rich phase and immiscible in the TFSI-rich phase, which will limit the crossing of ions that often limits the efficiency of such devices. The use of LiTFSI-LiX-water ABS (with X = Cl, Br, I) is thus promising as highly concentrated LiX is not only the supporting salt forming the ABS but also the positive redox active species. However, designing a system using the LiTFSI-LiX-water ABS requires the use of Li^+-based redox reaction at the negative electrode, which as discussed above will be subject to competing hydrogen evolution reaction. Hence, by turning to LiTFSI-ZnX_2-water ABS, this issue could be solved by doing zinc plating at the negative electrode. Overall, the wide variety of ABS provides a plethora of opportunities to design new electrochemical devices for which knowledge concerning ion partitions of each phase can be drawn from separation and purification studies based on ABS.

The exciting new opportunities provided by the use of ABS in electrochemical devices ask for a better fundamental understanding of ABS, specifically of the liquid-liquid interface. Taking inspiration from fundamental studies at the water-oil interface between two immiscible electrolytes (ITIES), the first step is to better understand the structure of the interface. For this the LiTFSI-LiCl-water ABS was studied in details, providing the phase diagram, the surface tension and the temperature behavior. Raman imaging was then used to characterize the liquid-liquid interface, showing a continuous change of the $TFSI^-$ intensity and water hydrogen bounding network between the TFSI-rich and the Cl-rich phases. Surprisingly, the continuous change is measured along several micrometers, forming interfaces up to 10 µm thick, very large when compared to molecularly sharp, nanometer-thick ITIES. The thickness of the interface is found to be concentration dependent, observing smaller interfaces with higher concentration, until the limitation of the Raman imaging is reached, *i.e.* below 1 µm. Switching from LiCl to HCl, the temperature behavior is inversed from a lower critical temperature for the LiTFSI-LiCl-water ABS, to an upper critical temperature for the LiTFSI-HCl-water ABS. Nevertheless, the interfacial thickness of LiTFSI-HCl-water ABS follows the same trend, being micrometer-sized with similar concentration dependence. Unlike salt-salt ABS, similar Raman imaging technique showed sharp interfaces forming for salt-polymer ABS and for an ITIES (1mM TBATPB in DCE and 10mM LiCl in water). To further comprehend the micrometer thick salt-salt ABS interfaces, ellipsometry measurements were attempted. However, it was found challenging when performed at the liquid-liquid interface. Other techniques specific to interfaces such as neutron reflectometry or sum frequency generation can be used to gain deeper knowledge on the hydrogen bounding network. Indeed, as previously suggested but never demonstrated, the hydrogen bounding network which is highly sensitive to ions in solution is certainly responsible both for the formation of the ABS and for forming such large interfaces.

Toward the application of ABS in redox flow batteries or electrolysers, ABS need to be studied in greater details, more specifically their ion partition and the crossing of ions at the interface. Selectivity of ions crossing at the interface is cornerstone to ensure low self-discharge. Indeed, in redox flow batteries, if the redox active molecules from the positive and negative electrolyte are in contact, self-discharge will occur. Thus, redox active molecules from the positive electrolyte should not cross to the negative electrolyte and *vice versa*, the redox active molecules from the negative electrolyte should not cross to the positive electrolyte. Hence, redox active molecules should have the highest possible ion partition to obtain low self-discharge. At the same time, selectivity of ions crossing at the interface is also cornerstone to ensure good energy efficiencies. Indeed, ions responsible for maintaining the charge balance between the positive and negative electrolytes must efficiently cross the interface, *i.e.* without overpotential and while minimizing the resistance of ion transfer. Being aware of these key points regarding the ion transfer, we developed an electrochemical cell to study liquid-liquid interfaces which was successfully tested on ITIES. Preliminary results show

how this cell can be used to study ions crossing at ABS interfaces and now will be further used to bring an understanding of the effects of salt concentrations and the effect of solvation structure on ion transfer mechanism and kinetics.

Perspectives

To bring some perspectives on this work, highly concentrated aqueous solutions can be used to design high voltage aqueous Li-ion battery. However, aqueous batteries are still far behind their organic counterpart in terms of energy capacity and shelf-life, while being barely competitive with already commercialized Ni-MH batteries, leaving a long way before commercializing high voltage aqueous Li-ion battery. Nevertheless, highly concentrated aqueous solutions where found to form ABS when mixing salts with different solvation properties, which brings many new opportunities regarding membrane-less electrochemical devices. With these opportunities come challenges concerning both the physics of the interface, particularly in addressing how to circulate the electrolytes without disrupting the ABS interface, and the chemistry of the interface, *i.e.* tackling self-discharge issues. By developing the use of new tools such as Raman imaging or electrochemistry in the context of ABS liquid-liquid interfaces, this thesis contributes in laying the foundation toward electrochemical devices based on ABS but also toward a renewal of ABS studies using Raman imaging and electrochemistry not only for salt-salt ABS but also to polymer, salt and ionic liquid containing ABS.

More broadly, electrochemistry has been largely focused in the past decades on the solid-liquid interface, largely due to the advent of rechargeable Li-ion batteries and electrocatalytic reactions such as water splitting. More specifically, research efforts were dedicated to developing new electrode materials, either to reach larger capacity in batteries or to obtain lower overpotential and better selectivity in electrocatalysis. On the contrary, with the unusual chemistry of highly concentrated aqueous electrolytes, this thesis brings back the light on electrolytes, where novel design principles are now available to improve electrochemical devices. For example, highly concentrated organic electrolytes are envisioned to prevent detrimental dissolution of positive electrodes in batteries[138,205] while a fine tuning of hybrid organic-aqueous electrolytes is expected to bring selectivity to reactions such as the hydrogen evolution[206], CO_2 reduction[207–209] or next generation electro-synthesis[210,211]. Considering more complex multiphasic electrolytes such as ABS or immiscible liquids, new membrane-less redox flow batteries[52] can be expected along with the development of (photo)electrocatalysis at liquid-liquid interface.[52,212] Hence, we believe that the development of innovative electrolytes will open novel avenues to electrochemical devices, in particular benefiting to the energy field where a breakthrough is needed in order to shift from a society based on fossil fuels to a society relying on intermittent electricity stored at a large scale, both in batteries and via the reduction of small molecules (H_2O, CO_2, N_2) to form synthetic fuels.

Supplementary information and Methods

S-II. Supplementary information for Chapter II

Material and Methods for Chapter II

General procedures. The electrolytes were prepared by weighting anhydrous salts (LiCl anhydrous, Alfa Aesar, 99%; $ZnCl_2$ anhydrous, Alfa Aesar, 98%; LiTFSI extra dry, Solvionic, 99.9%) in an Argon filled glovebox (MBraun, $O_2 < 0.1$ ppm, $H_2O < 0.1$ ppm) and by adding the right weight of $HClO_4$ (Sigma-Aldrich, 99.999%) or $Zn(TFSI)_2$ (anhydrous, Solvionic, 99.5%) concentrated aqueous solutions and/or Milli-Q water to reach targeted final compositions. Densities were measured using density meter (Anton Paar, DMA 35). All chemicals were used as received without further purification.

Cleaning procedures. All experiments were carried out in electrochemical glass cells at room temperature (≈20 °C). Prior to any series of experiments, all glassware was cleaned overnight in 0.5 mol.L^{-1} H_2S0_4 (Sigma-Aldrich, 95-98%) and 1 g.L^{-1} $KMnO_4$ (Alfa Aesar, 98%), followed by rinsing with a dilute (≈0.01 mol.L^{-1}) solution of H_2SO_4 (Sigma-Aldrich, 95-98%) and H_2O_2 (Sigma-Aldrich, 30% w/w) to remove any traces of $KMnO_4$ and MnO_2. Finally, the glassware was rinsed three times and boiled using Milli-Q water. The rinsing-boiling procedure was repeated two times.

Electrodes preparation. The Li$^+$-ISE was prepared by pressing on a titanium mesh a mix of carbon coated $LiFePO_4$ (Umicore) and Polytetrafluoroethylene (PTFE, Sigma-Aldrich, 60 wt% dispersion in water) with a weight ratio of 9:1 which had been dried overnight at 80°C under vacuum. The as-prepared electrode was then half charged in a three-electrode cell in a 1 mol.L^{-1} Li_2SO_4 aqueous solution in order to reach a stable potential plateau. The Zn^{2+}-ISE consisted of a zinc foil (Alfa Aesar, 99.98%) polished with three polishing slurries (6 µm diamond on nylon polishing disk, followed by 0.3 µm and then 0.04 µm aluminium oxide on microcloth polishing disk) using a polishing machine (Presi, Le Cube). The H$^+$-ISE was a polycrystalline platinum disk of 5 mm diameter at 1600rpm (Pine Research, 0.196 cm^2 geometrical surface area) in solutions continuously bubbled with H_2 (Linde, purity 5.5). Prior to any series of measurement, the platinum disk was treated with concentrated nitric acid

(VWR, 69%), then extensively rinsed with Milli-Q water before to be electro-polished in three electrode configuration by scanning between -0.35 V vs SCE and 1.45 V vs SCE at 500 mV.s^{-1} for 30 scans at 1600 rpm (Pine Research, MSR Rotator) in 0.5 mol.L^{-1} H_2SO_4 (Sigma-Aldrich, 99.999%). The Cl^--ISE was purchased from Edaq (ET1602 Chloride ions electrode) and used as received. Alternatively, halide ISEs were prepared by oxidizing a silver wire (Ag, Alfa Aesar, 99.9%, 0.5mm diameter) at constant current (i = 100 µA) for 1 hour in 1 mol.L^{-1} hydrobromic acid (HBr, Sigma-Aldrich, 48%, ACS reagent) for the Br-ISE, or in 1 mol.L^{-1} hydrochloric acid (HCl, Sigma-Aldrich, 30%, Suprapur) for the Cl-ISE, using a three-electrode setup with a SCE as RE and a Pt gauze in a fritted isolation compartment as CE.

Data acquisition. Data were acquired on a Biologic VSP potentiostat in solutions with a volume of 10 mL and de-aerated with Ar (Linde, purity 5.0) during at least 15 min prior to any measures. The reference electrode was a saturated calomel electrode (OrigaLys, XR110) regularly calibrated and with a potential of 241 ± 0.5 mV vs RHE (Gaskatel, HydroFlex) in 1 mol.L^{-1} H_2SO_4 (Sigma-Aldrich, 99.999%). The concentration cell was composed of two compartment separated by a frit. No counter electrode was needed since only OCV were measured. OCV values were determined after waiting up to several hours in order to reach a stable plateau.

Supplementary Equations for Chapter II

The Nernstian potential shift associated to ion-selective electrodes (ISEs) is described in part **II.B.** with the following equation:

$$\Delta E_N = E_N(m) - E_N\left(m_{Ref}\right) \qquad eq.II-19$$

The Li^+-ISE is based on the reversible intercalation of Li^+ into $FePO_4$/$LiFePO_4$. Hence, the redox couple and the Nernstian potential shift for Li^+ can be expressed as:

$$x\mathrm{Li^+}_{(\mathrm{aq})} + x\mathrm{e}^- + (1-x)\mathrm{LiFePO}_{4(\mathrm{s})} + x\mathrm{FePO}_{4(\mathrm{s})} = \mathrm{LiFePO}_{4(\mathrm{s})} \qquad eq.II-\mathrm{S1}$$

$$\Delta E_N = \frac{RT}{F}\ln\left(\frac{a_{\mathrm{Li^+}}(m)}{a_{\mathrm{Li^+}}\left(m_{Ref}\right)}\right) + \frac{RT}{F}\ln\left(\frac{a_{\mathrm{FePO_4}}(m)}{a_{\mathrm{FePO_4}}\left(m_{Ref}\right)}\right) - \frac{RT}{F}\ln\left(\frac{a_{\mathrm{LiFePO_4}}(m)}{a_{\mathrm{LiFePO_4}}\left(m_{Ref}\right)}\right) \qquad eq.II-\mathrm{S2}$$

Considering that $\mathrm{LiFePO_{4}}_{(\mathrm{s})}$ and $\mathrm{FePO_{4}}_{(\mathrm{s})}$ form a two-phase system[128], according to Gibbs' phase rule their activities are constant[213,214], thus:

$$\Delta E_N = \Delta E_N^c + \Delta E_N^\gamma \qquad eq.II-\mathrm{S3}$$

$$\Delta E_N^c = \frac{RT}{F}\ln\left(\frac{c_{\mathrm{Li^+}}(m)}{c_{\mathrm{Li^+}}(m_{Ref})}\right) \qquad eq.II-\mathrm{S4}$$

$$\Delta E_N^\gamma = \frac{RT}{F}\ln\left(\frac{\gamma_{\mathrm{Li^+}}(m)}{\gamma_{\mathrm{Li^+}}(m_{Ref})}\right) \qquad eq.II-\mathrm{S5}$$

The Zn^{2+}-ISE is based on the $Zn^{2+}/Zn_{(s)}$ reversible couple. Hence, the redox couple and the Nernstian potential shift for Zn^{2+} can be expressed as:

$$\mathrm{Zn^{2+}}_{(\mathrm{aq})} + 2\mathrm{e^-} = \mathrm{Zn}_{(\mathrm{s})} \qquad eq.II-\mathrm{S6}$$

$$\Delta E_N = \frac{RT}{2F}\ln\left(\frac{a_{\mathrm{Zn^{2+}}}(m)}{a_{\mathrm{Zn^{2+}}}(m_{Ref})}\right) - \frac{RT}{2F}\ln\left(\frac{a_{\mathrm{Zn}}(m)}{a_{\mathrm{Zn}}(m_{Ref})}\right) \qquad eq.II-\mathrm{S7}$$

Considering that $\mathrm{Zn}_{(\mathrm{s})}$ is a pure solid, its activity is unity, thus:

$$\Delta E_N = \Delta E_N^c + \Delta E_N^\gamma \qquad eq.II-\mathrm{S8}$$

$$\Delta E_N^c = \frac{RT}{2F}\ln\left(\frac{c_{\mathrm{Zn^{2+}}}(m)}{c_{\mathrm{Zn^{2+}}}(m_{Ref})}\right) \qquad eq.II-\mathrm{S9}$$

$$\Delta E_N^\gamma = \frac{RT}{2F}\ln\left(\frac{\gamma_{\mathrm{Zn^{2+}}}(m)}{\gamma_{\mathrm{Zn^{2+}}}(m_{Ref})}\right) \qquad eq.II-\mathrm{S10}$$

The H^+-ISE is based on the RHE. Hence, the redox couple and the Nernstian potential shift for H^+ can be expressed as:

$$2\mathrm{H^+}_{(\mathrm{aq})} + 2\mathrm{e^-} = \mathrm{H_2}_{(\mathrm{g})} \qquad eq.II-\mathrm{S11}$$

$$\Delta E_N = \frac{RT}{F}\ln\left(\frac{a_{\mathrm{H^+}}(m)}{a_{\mathrm{H^+}}(m_{Ref})}\right) - \frac{RT}{F}\ln\left(\sqrt{\frac{a_{\mathrm{H_2}}(m)}{a_{\mathrm{H_2}}(m_{Ref})}}\right) \qquad eq.II-\mathrm{S12}$$

Considering that the electrolyte and the electrochemical cell are purged with dihydrogen, one can assume that for every molality: $a_{\mathrm{H_2}}(m) \approx a_{\mathrm{H_2}}(m_{Ref})$ thus:

$$\Delta E_N = \Delta E_N^c + \Delta E_N^\gamma \qquad eq.II - \mathrm{S}13$$

$$\Delta E_N^c = \frac{RT}{F}\ln\left(\frac{c_{\mathrm{H}^+}(m)}{c_{\mathrm{H}^+}(m_{Ref})}\right) \qquad eq.II - \mathrm{S}14$$

$$\Delta E_N^\gamma = \frac{RT}{F}\ln\left(\frac{\gamma_{\mathrm{H}^+}(m)}{\gamma_{\mathrm{H}^+}(m_{Ref})}\right) \qquad eq.II - \mathrm{S}15$$

The Cl^--ISE is based on the $\mathrm{AgCl}_{(s)}/\mathrm{Ag}_{(s)}$ reversible couple. Hence, the redox couple and the Nernstian potential shift for Cl^- can be expressed as:

$$\mathrm{AgCl}_{(s)} + \mathrm{e}^- = \mathrm{Cl^-}_{(aq)} + \mathrm{Ag}_{(s)} \qquad eq.II - \mathrm{S}16$$

$$\Delta E_N = -\frac{RT}{F}\ln\left(\frac{a_{\mathrm{Cl}^-}(m)}{a_{\mathrm{Cl}^-}(m_{Ref})}\right) + \frac{RT}{F}\ln\left(\frac{a_{\mathrm{AgCl}}(m)}{a_{\mathrm{AgCl}}(m_{Ref})}\right) - \frac{RT}{F}\ln\left(\frac{a_{\mathrm{Ag}}(m)}{a_{\mathrm{Ag}}(m_{Ref})}\right) \qquad eq.II - \mathrm{S}17$$

Considering that $\mathrm{AgCl}_{(s)}$ and $\mathrm{Ag}_{(s)}$ are pure solids, their activities are unity, thus:

$$\Delta E_N = \Delta E_N^c + \Delta E_N^\gamma \qquad eq.II - \mathrm{S}18$$

$$\Delta E_N^c = -\frac{RT}{F}\ln\left(\frac{c_{\mathrm{Cl}^-}(m)}{c_{\mathrm{Cl}^-}(m_{Ref})}\right) \qquad eq.II - \mathrm{S}19$$

$$\Delta E_N^\gamma = -\frac{RT}{F}\ln\left(\frac{\gamma_{\mathrm{Cl}^-}(m)}{\gamma_{\mathrm{Cl}^-}(m_{Ref})}\right) \qquad eq.II - \mathrm{S}20$$

The Br^--ISE is based on the $\mathrm{AgBr}_{(s)}/\mathrm{Ag}_{(s)}$ reversible couple. Hence, the redox couple and the Nernstian potential shift for Br^- can be expressed as:

$$\mathrm{AgBr}_{(s)} + \mathrm{e}^- = \mathrm{Br^-}_{(aq)} + \mathrm{Ag}_{(s)} \qquad eq.II - \mathrm{S}21$$

$$\Delta E_N = -\frac{RT}{F}\ln\left(\frac{a_{\mathrm{Br}^-}(m)}{a_{\mathrm{Br}^-}(m_{Ref})}\right) + \frac{RT}{F}\ln\left(\frac{a_{\mathrm{AgBr}}(m)}{a_{\mathrm{AgBr}}(m_{Ref})}\right) - \frac{RT}{F}\ln\left(\frac{a_{\mathrm{Ag}}(m)}{a_{\mathrm{Ag}}(m_{Ref})}\right) \qquad eq.II - \mathrm{S}22$$

Considering that $\mathrm{AgBr}_{(s)}$ and $\mathrm{Ag}_{(s)}$ are pure solids, their activities are unity, thus:

$$\Delta E_N = \Delta E_N^c + \Delta E_N^\gamma \qquad eq.II - \mathrm{S}23$$

$$\Delta E_N^c = -\frac{RT}{F}\ln\left(\frac{c_{Br^-}(m)}{c_{\mathrm{Br}^-}(m_{Ref})}\right) \qquad eq.II - \mathrm{S}24$$

$$\Delta E_N^\gamma = -\frac{RT}{F}\ln\left(\frac{\gamma_{\mathrm{Br}^-}(m)}{\gamma_{Br^-}(m_{Ref})}\right) \qquad eq.II - \mathrm{S}25$$

Supplementary Data for Chapter II

In order to convert molalities to concentrations, and *vice versa* the following equation was used:

$$c = \frac{m * \rho_{sol}}{\frac{m * M(\text{salt})}{1000} + 1} \qquad eq. II - \text{S25}$$

with c the concentration (mol.L^{-1}), m the molality (mol.kg^{-1}), ρ_{sol} the volumetric mass of the solution (kg.L^{-1}) and $M(\text{salt})$ is the molar mass of the salt (g.mol^{-1}). Molalities and corresponding densities and concentrations are reported in the following tables:

ρ_{sol} (kg.L^{-1})	1 mol.kg^{-1}	5 mol.kg^{-1}	10 mol.kg^{-1}	15 mol.kg^{-1}	18 mol.kg^{-1}	20 mol.kg^{-1}
LiCl	1.02	1.10	1.18	1.24	1.28	
LiTFSI	1.13	1.42	1.57	1.66		1.71
$ZnCl_2$	1.11	1.42	1.68	1.86		1.98

Table II-S1. Measured densities for LiCl, LiTFSI and $ZnCl_2$ electrolytes.

c (mol.L^{-1})	1 mol.kg^{-1}	5 mol.kg^{-1}	10 mol.kg^{-1}	15 mol.kg^{-1}	18 mol.kg^{-1}	20 mol.kg^{-1}
LiCl	0.98	4.53	8.25	11.4	13.0	
LiTFSI	0.87	2.91	4.06	4.69		5.07
$ZnCl_2$	0.97	4.22	7.10	9.16		10.6

Table II-S2. Conversion between concentration and molality for LiCl, LiTFSI and $ZnCl_2$ electrolytes.

S-III. Supplementary information for Chapter III

Materials and Methods for Chapter III

Materials. Lithium bis(trifluoromethanesulfonyl)imide salt (LiTFSI Extra dry, Solvionic, 99.9%), lithium chloride salt (LiCl anhydrous, Alfa Aesar, 99%), lithium bromide salt (LiBr anhydrous, Alfa Aesar, 99%), Bromine liquid (Br_2, Sigma-Aldrich, 99%) were weighted and Milli-Q water was added to reach the desired molalities. $LiBr_3$ solutions were obtained by adding equimolar quantities of Br_2 to LiBr solutions. Graphite (KS4, Imerys), activated carbon (YP-50F, Kuraray), Carbon black (Super P, Alfa Aesar) were used as received while Polytetrafluoroethylene (PTFE, Sigma-Aldrich, 60wt% dispersion in H_2O) was dried under vacuum overnight.

Batteries cycling. Self-standing electrodes were prepared in argon-filled glovebox (MBraun, $O_2 < 0.1$ ppm, $H_2O < 0.1$ ppm). Self-standing working electrodes (WE) were obtained by hand grinding LiBr/LiCl/KS4/SP with mass ratio of 2/1/6/3 before to be laminated with 10wt% of dried PTFE. Similarly, self-standing counter electrodes (CE) were obtained by laminating YP-50F with 10wt% of dried PTFE. Reference electrode (RE) was a leakless AgCl/Ag (ET069, eDAQ, 0.197 V vs SHE) regularly calibrated against RHE (HydroFlex, Gaskatel) in 1 mol.L^{-1} H_2SO_4. Swagelok-type three-electrode cells were assembled with the self-standing WE (6 mg) pressed on a titanium gauze (Ti, Alfa Aesar, 99.5%, 40 mesh, 0.127mm diameter wire) separated from the self-standing CE and the RE by glass fibers sheets (GF/D, Whatman) soaked in 20m LiTFSI before to be cycled on a potentiostat (VSP, Biologic) at 0.05 mV.s^{-1}.

Three-dimensional Pourbaix diagrams. The three-dimensional Pourbaix diagrams were obtained by plotting the lowest potential according to the following equations, applying the condition of concentration equality in element and assuming water activity to be unity (**S-III: Supplementary Discussion** and **Fig. III-S3**)[144]:

For bromide oxidation:

$$E = E°_{Br_2/Br^-} + \frac{RT}{2F} ln\left(\frac{c\left(Br_{2(aq)}\right)}{c\left(Br^-{}_{(aq)}\right)^2}\right) \text{ with } \frac{c\left(Br_{2(aq)}\right)}{c\left(Br^-{}_{(aq)}\right)} = \frac{1}{2} \text{ and } E°_{Br_2/Br^-} = 1.08 \text{ V vs SHE}$$

$$E = E°_{Br_3{}^-/Br^-} + \frac{RT}{2F} ln\left(\frac{c\left(Br_3{}^-{}_{(aq)}\right)}{c\left(Br^-{}_{(aq)}\right)^3}\right) \text{ with } \frac{c\left(Br_3{}^-{}_{(aq)}\right)}{c\left(Br^-{}_{(aq)}\right)} = \frac{1}{3} \text{ and } E°_{Br_3{}^-/Br^-} = 1.06 \text{ V vs SHE}$$

$E = E°_{BrO_3^-/Br^-} + \frac{RT}{6F} ln\left(\frac{c\left(BrO_3{}^-{}_{(aq)}\right).a\left(H^+{}_{(aq)}\right)^6}{c\left(Br^-{}_{(aq)}\right).\ a\left(H_2O_{(l)}\right)^3}\right)$ with $\frac{c\left(BrO_3{}^-{}_{(aq)}\right)}{c\left(Br^-{}_{(aq)}\right)} = 1$ and $E°_{BrO_3^-/Br^-}$ = 1.41 V vs SHE

For chloride oxidation:

$E = E°_{Cl_2/Cl^-} + \frac{RT}{2F} ln\left(\frac{c\left(Cl_{2(aq)}\right)}{c\left(Cl^-{}_{(aq)}\right)^2}\right)$ with $\frac{c\left(Cl_{2(aq)}\right)}{c\left(Cl^-{}_{(aq)}\right)} = \frac{1}{2}$ and $E°_{Cl_2/Cl^-}$ = 1.36 V vs SHE

$E = E°_{Cl_3^-/Cl^-} + \frac{RT}{2F} ln\left(\frac{c\left(Cl_3{}^-{}_{(aq)}\right)}{c\left(Cl^-{}_{(aq)}\right)^3}\right)$ with $\frac{c\left(Cl_3{}^-{}_{(aq)}\right)}{c\left(Cl^-{}_{(aq)}\right)} = \frac{1}{3}$ and $E°_{Cl_3^-/Cl^-}$ = 1.38 V vs SHE

$E = E°_{HClO/Cl^-} + \frac{RT}{2F} ln\left(\frac{c\left(HClO_{(aq)}\right).a\left(H^+{}_{(aq)}\right)}{c\left(Cl^-{}_{(aq)}\right).a\left(H_2O_{(l)}\right)}\right)$ with $\frac{c\left(HClO_{(aq)}\right)}{c\left(Cl^-{}_{(aq)}\right)} = 1$ and $E°_{HClO/Cl^-}$ = 1.49 V vs SHE

$E = E°_{ClO^-/Cl^-} + \frac{RT}{2F} ln\left(\frac{c\left(ClO^-{}_{(aq)}\right).a\left(H^+{}_{(aq)}\right)^2}{c\left(Cl^-{}_{(aq)}\right).a\left(H_2O_{(l)}\right)}\right)$ with $\frac{c\left(ClO^-{}_{(aq)}\right)}{c\left(Cl^-{}_{(aq)}\right)} = 1$ and $E°_{ClO^-/Cl^-}$ = 1.72 V vs SHE

For iodide oxidation:

$E = E°_{I_2/I^-} + \frac{RT}{2F} ln\left(\frac{c\left(I_{2(aq)}\right)}{c\left(I^-{}_{(aq)}\right)^2}\right)$ with $\frac{c\left(I_{2(aq)}\right)}{c\left(I^-{}_{(aq)}\right)} = \frac{1}{2}$ and $E°_{I_2/I^-}$ = 0.53 V vs SHE

$E = E°_{I_3^-/I^-} + \frac{RT}{2F} ln\left(\frac{a\left(I_3{}^-{}_{(aq)}\right)}{a\left(I^-{}_{(aq)}\right)^3}\right)$ with $\frac{c\left(I_3{}^-{}_{(aq)}\right)}{c\left(I^-{}_{(aq)}\right)^3} = \frac{1}{2}$ and $E°_{I_3^-/I^-}$ = 0.45 V vs SHE

$E = E°_{IO_3^-/I^-} + \frac{RT}{6F} ln\left(\frac{c\left(IO_3{}^-{}_{(aq)}\right).a\left(H^+{}_{(aq)}\right)^6}{c\left(I^-{}_{(aq)}\right).\ a\left(H_2O_{(l)}\right)^3}\right)$ with $\frac{c\left(IO_3{}^-{}_{(aq)}\right)}{c\left(I^-{}_{(aq)}\right)} = 1$ and $E°_{IO_3^-/I^-}$ = 1.08 V vs SHE

Halides oxidation on rotating disk electrode. Halides oxidation experiments were performed in three-electrode glass cell with about 10 mL of electrolyte degassed for 15 min with argon (Linde, HiQ 5.0). A saturated calomel electrode (SCE, OrigaLys, 0.242 V vs SHE) was used as RE, a flamed-annealed platinum gauze (Pt, Alfa Aesar, 99.9%, 100 mesh, 0.0762mm diameter wire) in a fritted isolation compartment was used as CE, and a glassy carbon (GC, Pine Research, 0.196 cm^2_{geom}) on a rotating disk electrode setup (RDE, Pine Research, 1600rpm) as WE. Prior to any measurement, the GC electrode was sequentially polished with three slurries (6 µm diamond, 0.3 and 0.04 µm aluminium oxide, Presi) using a polishing machine (Le Cube, Presi) before to remove any residual traces of slurries by sonicating the electrodes three times in water/ethanol 50/50 (5 min each). All measurements were performed using a potentiostat (VSP, Biologic) and ohmic drop was measured after the electrochemical measurements via electrochemical impedance spectroscopy (EIS) and corrected manually during data treatment. Typical resistance between 5-15 Ω were measured.

Estimation of the potential shift due to activity changes and the liquid junction potential (LJP). Open circuit voltage (OCV) at different molalities were measured with a potentiostat (VSP, Biologic) in a two-electrode configuration between a SCE as RE and an ion selective electrode (ISE) to chloride (Cl-ISE) or bromide (Br-ISE), similarly to previously reported.[139] Halides ISE were prepared by oxidizing a silver wire (Ag, Alfa Aesar, 99.9%, 0.5mm diameter) at constant current (i = 100 µA) for 1 hour in 1 mol.L^{-1} hydrobromic acid (HBr, Sigma-Aldrich, 48%, ACS reagent) for the Br-ISE, or in 1 mol.L^{-1} hydrochloric acid (HCl, Sigma-Aldrich, 30%, Suprapur) for the Cl-ISE using a three-electrode setup with a SCE as RE and a Pt gauze in a fritted isolation compartment as CE. Data analysis was performed according to the method previously describe (Degoulange *et al.*[139]) by calculating $\Delta E = \mathrm{OCV}(m) - \mathrm{OCV}(m_{Ref})$ and $\Delta E_N^c = \frac{RT}{2F}\ln\left(\frac{c_{halide}(m_{Ref})}{c_{\mathrm{halide}}(m)}\right)$ with m_{Ref} = 1m.

UV-Vis spectroscopy. UV-Vis spectra were recorded on a Mettler Toledo UV5bio spectrometer using an absorption quartz cell (Hellma analytics, Quartz Glass High Performance 200 nm – 2500 nm, 1mm optical path length). For UV-Vis spectra of Br_3^- and Br_2, Br_2 was added to a 15m LiBr or a 20m LiTFSI solution, respectively, making the background subtraction with respective solutions before addition of Br_2. From the spectra of the Br_2 saturated 20m LiTFSI solution, the solubility of Br_2 was estimated using Beer-Lambert law $A =$

$\varepsilon.l.C$ with a molar extinction coefficient $\varepsilon_{420}(Br_2)$ = 165 mol^{-1}.L.cm^{-1} (in **S-III: Table III-S2**). For UV-Vis spectra of Br_3^- in the Br-rich phase of the ABS, Br_2 was added to the ABS before to be vortexed for 1 min and then centrifuged at 6000rpm for 10 min, making the background subtraction from the centrifuged ABS before Br_2 addition. Centrifugation was key to properly separate the ABS and thus to limit Rayleigh scattering from emulsion of the ABS phases.

ABS phase diagram. Phase diagrams were measured at room temperature using the cloud point titration method previously described.[33,107,143] Briefly, starting from a known mass of a concentrated solution of one component ($LiBr_3$ or LiTFSI), a concentrated solution of the second component is weighed while being added dropwise and vortexed until the solution turns cloudy. Then, Milli-Q water is weighed while being added dropwise and vortexed until the solution turns clear again (even though still showing the red color). These steps are repeated for each point of the diagram.

XRD diffraction and Rietveld refinement. Powder X-ray diffraction (XRD) patterns were taken in Bragg–Brentano geometry (Bruker D8 Advance, Cu Kα X-ray source, λ_1 = 1.5406 Å, λ_2 = 1.5444 Å, LYNXEYE XE detector). Graphite was put in contact with 10m LiBr + 5m $LiBr_3$ in a sealed capillary (Capillary Tube Supplies Ltd, borosilicate glass, 0.6 mm outside diameter, 0.01 mm wall thickness) while pristine graphite was put alone in the sealed capillary. Both diffraction patterns were refined using the FullProf program.[152]

Quantitative electrolysis. Electrolysis measurements were performed in three-electrode glass cell with 10 mL of electrolyte degassed for 15 min with Ar. A SCE was used as RE, a flamed-annealed Pt gauze in a fritted isolation compartment was used as CE and self-standing obtained by laminating KS4 with 10wt% of dried PTFE before to be pressed on a Ti gauze used as WE. Electrolysis was performed (VSP, Biologic) at constant current of i = 1.2 mA (equivalent to 200 mA.g$^{-1}_{ks4}$ with 6mg KS4 and equivalent to 80 mA.g$^{-1}_{LBC\text{-}G}$ as reported by Yang *et al.*[7]) for t = 8 min leading to a charge $Q_{electrolysis} = i.\Delta t$ equivalent to a concentration through the faraday law of electrolysis $C_{Faraday} = \frac{Q_{electrolysis}}{n.F.V}$ with n = 2 and V = 10 mL. This concentration is compared to the concentration estimated using Beer-Lambert law with $\varepsilon_{272}(Br_3{}^-)$ = 46600 mol^{-1}.L.cm^{-1} for the electrolysis of 15m LiBr and $\varepsilon_{232}(BrCl_2{}^-)$ = 32700 mol^{-1}.L.cm^{-1} for the electrolysis of 15m LiCl (in **S-III: Table III-S2**).

Supplementary Discussion for Chapter III

For the sake of simplification, we have assumed water activity to be 1 when calculating the three-dimensional Pourbaix diagrams. Water activity does not deviate much from unity for concentration below 1 mol.L^{-1}, making our assumption correct for concentrations tested below that threshold. For concentrations above 1 mol.L^{-1}, water activity decreases with concentration[144] (**Fig. III-S3**). This drops leads to a potential shift according to $\frac{RT}{2F} ln\left(\frac{1}{a(H_2O_{(l)})}\right)$ for the redox couples $BrO_3{}^-/Br^-$, $HClO/Cl^-$, ClO^-/Cl^- and $IO_3{}^-/I^-$. In **Fig. III-S3**, for the greatest concentration tested in our work, *i.e.* 15m LiCl, $a\left(H_2O_{(l)}\right)$ = 0.2 and the potential shift is calculated to be ≈20 mV. Hence, our approximation is acceptable as the potential shift due to water activity is negligible compared to the change in potential of the three-dimensional Pourbaix diagrams (**Fig. III-2**, **Fig. III-4**, **Fig. III-6**).

Supplementary Tables for Chapter III

Species	Wavelength (nm)	Molar Extinction coefficient (mol^{-1}.L.cm^{-1})
I_2	460[146]	975[146]
	270[146]	17200[146]
Br_2	390[150] ; 420[148]	186[150] ; 165[148]
Cl_2	325[150] ; 330[148]	70[150] ; 67[148]
BrCl	343[150] ; 370[148]	70[150] ; 107[148]
ICl	240[148]	115[148]
	470[148]	111[148]
IBr	270[148]	60[148]
	500[148]	318[148]

Table III-S1. Table of the maximum absorption wavelengths and corresponding molar absorption coefficients for the halogen species. From refs[146–150]

Species	Wavelength (nm)	Molar Extinction coefficient (mol^{-1}.L.cm^{-1})
I_3^-	364[149] ; 360[147] ; 353[146]	25250[149] ; 25500[147] ; 26400[146]
	294[149] ; 291[147] ; 287[146]	43320[149] ; 38800[147] ; 40000[146]
	440[149]	3000[149]
	565[149]	250[149]
Br_3^-	272[149] ; 266[150] ; 269[147]	46600[149] ; 40900[150] ; 55000[147]
	405[149] ; 362[150]	1000[149] ; 850[150]
Cl_3^-	220[150]	10400[150]
	325[150]	180[150]
I_2Br^-	351[147]	11600[147]
	280[147]	40600[147]
I_2Cl^-	232[149]	51620[149]
	347[149]	290[149]
	455[149]	30[149]
IBr_2^-	260[149] ; 256[147]	50020[149] ; 54000[147]
	380[149] ; 370[147]	330[149] ; 606[147]
	485[149]	20[149]
Br_2Cl^-	381[150]	288[150]
	245[150]	24900[150]
ICl_2^-	336[147]	310[147]
	227[147]	54500[147]
$BrCl_2^-$	242[149] ; 232[150]	37300[149] ; 32700[150]
	346[149] ; 343[150]	310[149] ; 312[150]
$IBrCl^-$	356[147]	413[147]
	237[147]	38700[147]

Table III-S2. Table of the maximum absorption wavelengths and corresponding molar absorption coefficients for the trihalides species. From refs[146–150]

Supplementary Figures for Chapter III

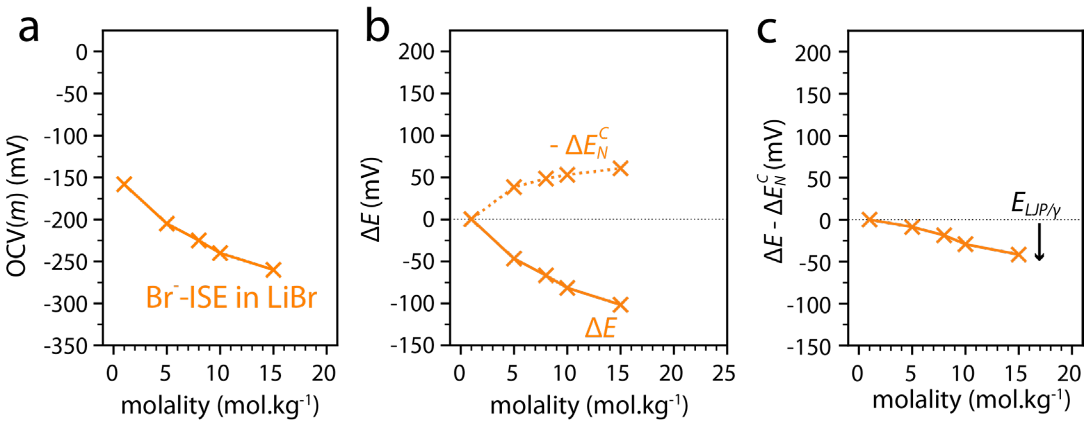

Fig. III-S1. Potential shift measured for a Br$^-$-ISE as function of LiBr molalities. a, OCV values of the Br$^-$-ISE in LiBr solutions against a SCE reference electrode. **b**, Extracted values of ΔE and calculated values of ΔE_N^C. **c**, $(\Delta E - \Delta E_N^C) = E_{LJP/\gamma}$ values of a Br$^-$-ISE in LiBr solutions.

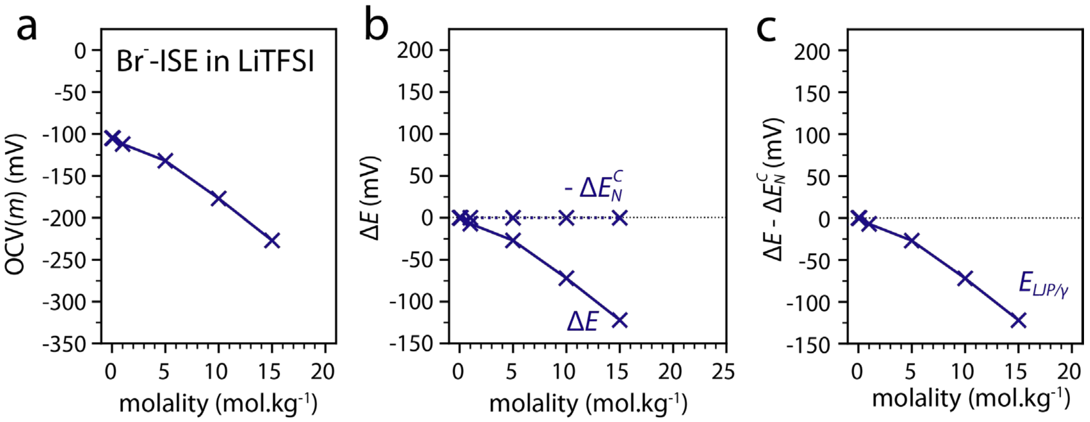

Fig. III-S2. Potential shift measured for a Br$^-$-ISE as function of LiTFSI molalities with 0.1 mol.L^{-1} LiBr. a, OCV values of the Br$^-$-ISE in LiTFSI solutions with 0.1 mol.L^{-1} added LiBr against a SCE reference electrode. **b**, Extracted values of ΔE and calculated values of ΔE_N^C. **c**, $(\Delta E - \Delta E_N^c) = E_{LJP/\gamma}$ values.

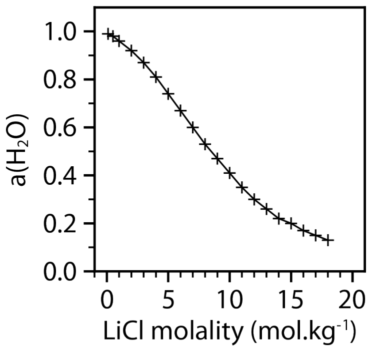

Fig. III-S3. Activity changes of water in concentrated LiCl. Adapted from Robinson *et al.*[143]

S-IV. Supplementary information for Chapter IV

Materials and Methods for Chapter IV

Materials. Lithium bis(trifluoromethanesulfonyl)imide (LiTFSI Extra dry, Solvionic, 99.9%), Lithium chloride (LiCl anhydrous, Alfa Aesar, 99%), Hydrochloric acid (HCl 30%, Sigma-Aldrich Suprapur) were weighted and Milli-Q water was added to reach the desired molalities. Tetrabutylammonium tetraphenylborate (TBATPB, 99% Sigma-Aldrich) was weighted to reach the desired concentration in Dichloroethane (DCE, 99%, Alfa Aesar). 2-Heptanone (99%, Alfa Aesar) was used as received.

Phase diagram construction. Phase diagrams were measured at room temperature using the cloud point titration method previously described[33,107]. Briefly, starting from a known mass of a concentrated solution of one component, an aqueous solution of the second component is weighted while being added dropwise and vortexed until the solution turns cloudy. Then water is weighted while being added dropwise and vortexed until the solution turns clear again. These steps are repeated for each point of the diagram. The diagrams were made starting from different initial LiCl, LiTFSI and HCl concentrations especially for the LiTFSI-HCl-water system in order to prevent imprecision due to HCl evaporation.

Interfacial tension. Interfacial tensions were measured at room temperature from the drop-weight method using Tate's law with Harkins and Brown correction[169]. Briefly, using a peristaltic pump (Watson-Marlow, 120U-DM2), drops of the highest density phase are slowly let fall into the lowest density phase. The average weighted of a drop is deduced and the surface tension is calculated according to Harkins and Brown correction. Densities were measured using an electronic density meter (Anton Paar, DMA 35 Basic).

Infra-Red Spectra. The IR spectra for LiTFSI-LiCl-water system were taken using a Nicolet iS5 FTIR spectrometer, mounted with a diamond Attenuated Total Reflectance accessory (iD1 ATR). The background correction was performed by measuring the ambient atmosphere and each spectra was acquired from 16 scans with a 4 cm^{-1} resolution from 4 000 to 500 cm^{-1}.

Variable temperature nuclear magnetic resonance. Pulse-field gradient stimulated echo (PFG-STE) diffusion measurements were realized on a Bruker 200 MHz wide bore spectrometer, equipped with a Diff50 gradient system and a ^{19}F-^{7}Li 8 mm insert inside a liquid-state Bruker probe. 1D profiles were recorded using the improf Bruker sequence (90°-gradient-180°-gradient-acquisition), with maximum field gradient strengths of 27, 29 and 30 G/cm respectively. The signals were acquired as full echoes (1-1.5 ms echo times) to avoid antiphase components and make the phasing easier. The maximum theoretical resolution was around 10-20 µm. Recycling delays of 7, 9 and 17 seconds were used, with 96, 16 and 16 transients acquired for ^{1}H, ^{19}F and ^{7}Li respectively.

Raman imaging. The microscope was a standard layout of an epi-detected Raman microscope. A pump laser beam (wavelength = 532 nm, Newport Millenia eV) was spectrally cleaned up by a bandpass filter (FLH05532-4, Thor Labs), and its beam width was expanded to 7.2 mm before entering a home built inverted microscope. Additional waveplates (half-waveplate and quarter-waveplate for 532 nm, Foctek Photonics) precompensated the ellipticity introduced by the dichroic filter (F38-532_T1, AHF) and also generated circularly polarized light to alleviate effects due to molecular orientation. We used high numerical aperture (NA) oil-immersion objectives (Nikon 60X/1.4NA oil) to ensure high-resolution imaging and increase collection efficiency. Pump power before the objective was 150 mW, a power level that ensured no degradation of domains within the scanned region. The samples were scanned/descanned with a set of galvanometric mirrors (Thor Labs). The Raman inelastic backscattered light was collected by the same objective and focused with the microscope tube lens on the entrance slit of the detector which acted as the effective pinhole for confocal detection. A notch filter blocked residual pump light (NF533-17, Thor Labs) before guiding the signal to the spectrometer (Andor, Shamrock 303i, grating 300 l/mm), equipped with a high-sensitivity charge-coupled camera (Andor, iXon 897). All images presented were taken with integration times/pixel in the 0.1 to 0.3 s settings range. Background subtraction of Raman spectra was performed using a modified iterative polynomial smoothing method. Peak decomposition was performed using a custom Python code and the lmfit toolbox.

Titration Microcalorimetry. The calorimetric titration measurements were completed isothermally using a power compensation microcalorimeter (Thermal Hazard Technology, µRC). Each injection was performed using an automated syringe pump tower attachment. The reference samples were 1 mL of the respective ABSs solutions, and samples were stirred to allow for uniform mixing. The partial enthalpy of mixing was found by integrating the resulting power spike upon injection of one phase into the second phase.

Supplementary Figures for Chapter IV

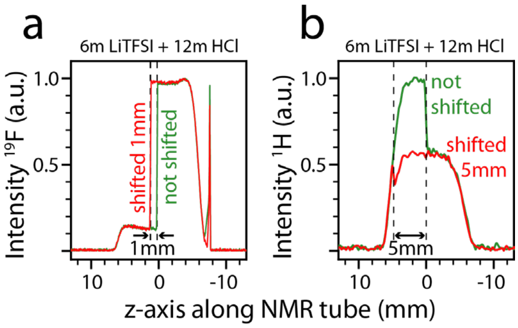

Fig. IV-S1. Calibration of the z-axis for the VT-NMR measurements. a, NMR for the 6m LiTFSI - 12m HCl biphasic system before (in green) and after (in red) shifting the NMR tube 1mm higher for z-axis calibration. **b**, Confirmation of the z-axis calibration doing NMR for the 6m LiTFSI - 12m HCl biphasic system before (in green) and after (in red) shifting the NMR tube 5mm higher.

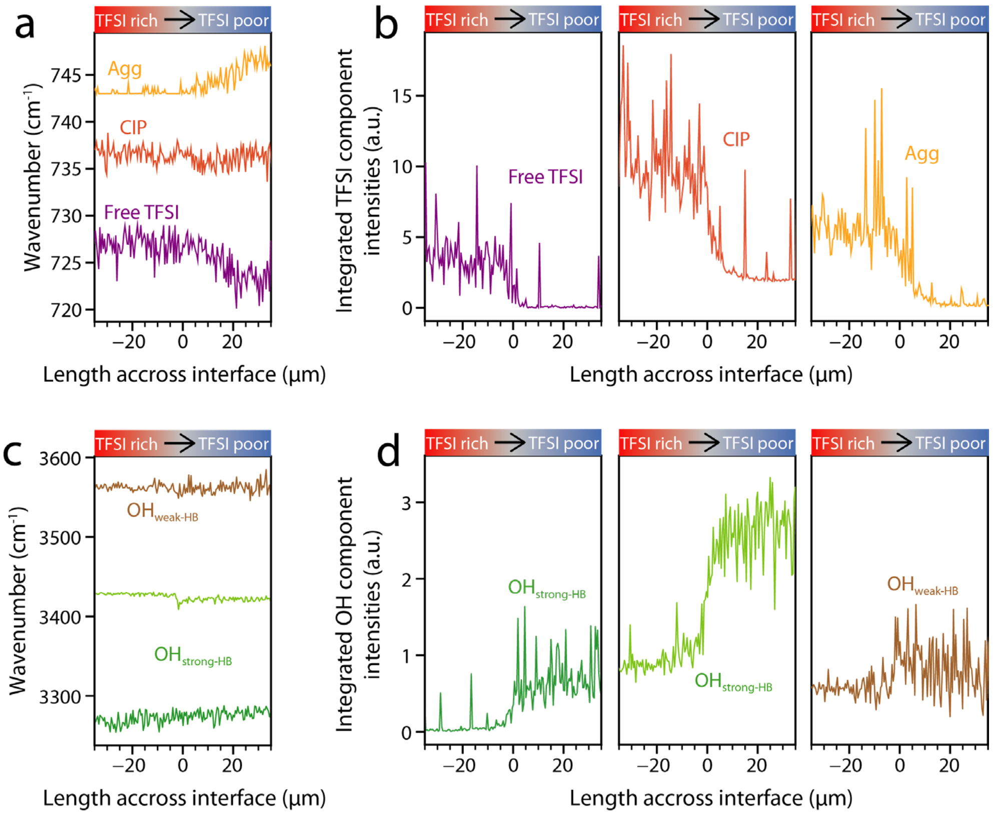

Fig. IV-S2. Peak decomposition for OH and TFSI$^-$ vibrations at 2.6m LiTFSI – 5.2m LiCl along the interface. a, TFSI$^-$ components wavenumbers along the interface for free TFSI$^-$ in purple, contact ion pair in orange and aggregate in yellow. **b,** TFSI$^-$ components integrated intensities along the interface. The colors matches that in (**a**). **c,** OH components wavenumbers along the interface for OH$_{strong\text{-}HB}$ in light and dark green and OH$_{weak\text{-}HB}$ in brown. **d,** OH components integrated intensities along the interface. The colors matches that in (**c**).

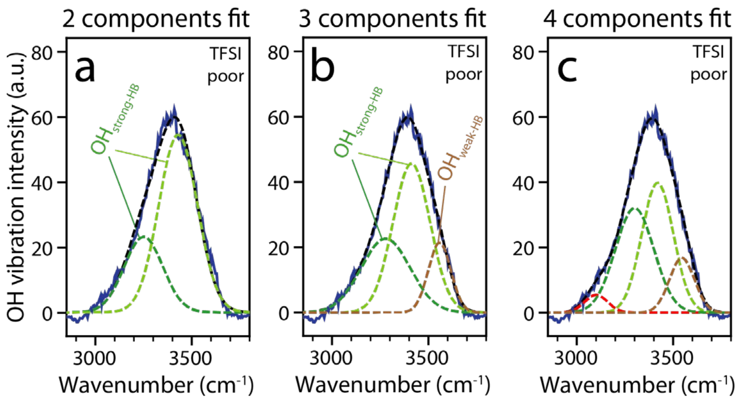

Fig. IV-S3. Fits with 2 to 4 components for the water spectrum of the TFSI-poor phase of the 2.6m LiTFSI – 5.2m LiCl system. For the 2 components the low-wavenumber shoulder is not well captured, whilst 3 and 4 components both fit.

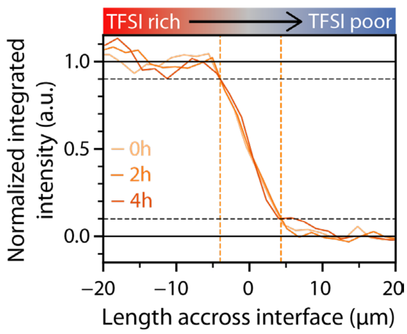

Fig. IV-S4. Evolution of the interfacial profile for TFSI$^-$ with time. Different spectra were recorded after 0, 2 and 4 hours for the 2.6m LiTFSI – 5.2m LiCl systems. Comparing them shows that the interface is stable over time, thus reflecting a stable system.

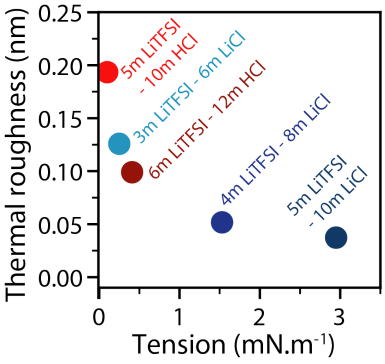

Fig. IV-S5. Estimation of the interface roughness $\sqrt{k_BT/\gamma}$ due to thermal capillary waves for the different ABSs studied. k_B is the Boltzmann constant, T the temperature taken to be 298 K and γ is the surface tension of the LiTFSI-LiCl-water and LiTFSI-HCl-water ABSs taken from **Fig. IV-2b** and **Fig. IV-10** respectively.

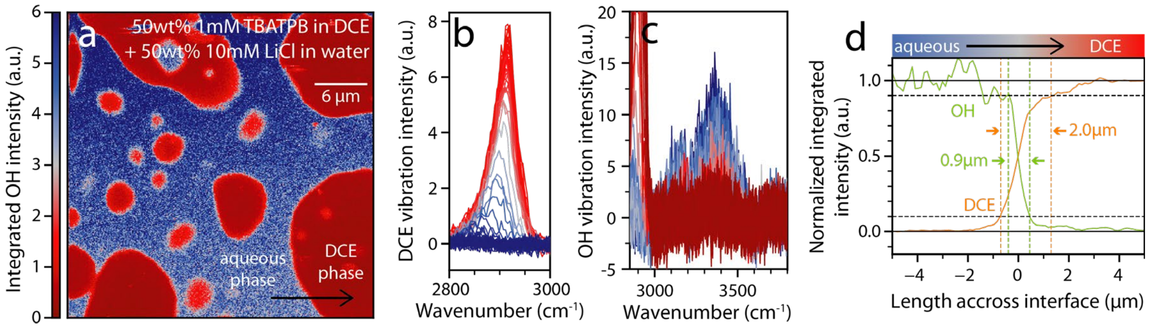

Fig. IV-S6. Raman imaging across the interface between DCE and water. **a**, Raman imaging of a system composed by 50wt% of 1mM TBATPB in DCE and 50wt% of 10mM LiCl in water generated by integration of the OH vibrations. **b-c**, Raman spectra collected across the interface for the DCE vibrations (**b**) and for OH vibrations (**c**). The color of plots matches that in (**a**). **d**, The normalized intensity of OH (green) and DCE (orange) vibrations across the interface.

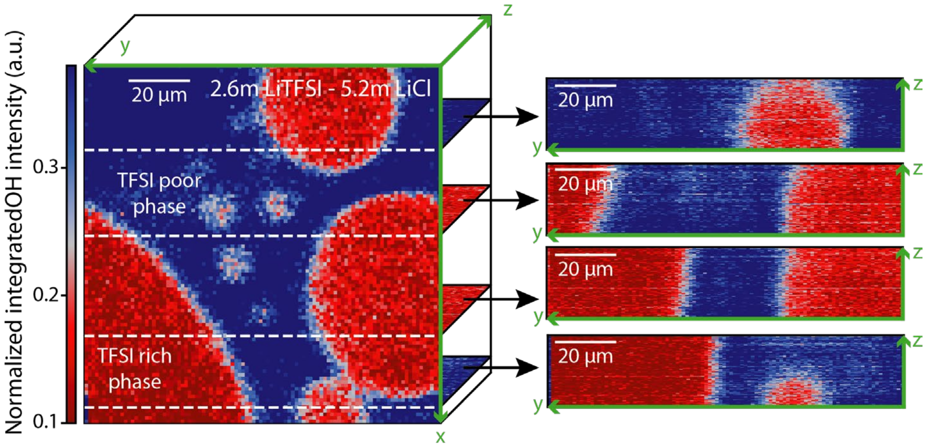

Fig. IV-S7. 3D reconstruction at 2.6m LiTFSI – 5.2m LiCl. Confocal Raman *z*-stack of approximately ≈20 µm through a region of sample showing phase separation. Taking cuts along the *yz* plane shows that over 20 µm the interface is approximately flat in the largest phase separated ‘droplets’. Consequently, the effects of curvature influencing our results can be ignored. Note that the apparent width in the z-direction is due to motion artifacts as each x-y plane takes is not perfectly commensurate with another (due to the translation stage position accuracy).

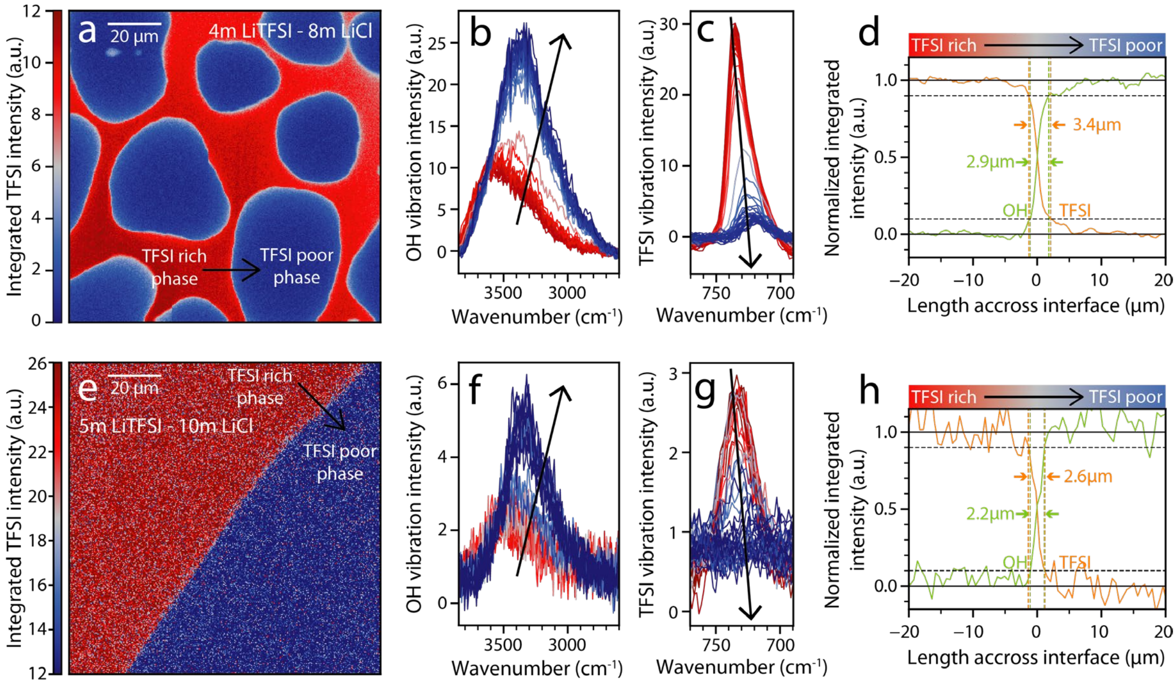

Fig. IV-S8. Raman imaging across the interface for different LiTFSI-LiCl-water systems. a, Raman imaging of the 4m LiTFSI – 8m LiCl system generated by integration of the TFSI$^-$ vibrations. **b-c**, Raman spectra collected across the interface for the TFSI$^-$ vibrations (**b**) and for OH vibrations (**c**) of the 4m LiTFSI – 8m LiCl system. The color of plots matches that in (**a**). **d**, The normalized intensity of OH (green) and TFSI$^-$ (orange) vibrations across the interface of the 4m LiTFSI – 8m LiCl system. **e**, Raman imaging of the 5m LiTFSI – 10m LiCl system generated by integration of the TFSI$^-$ vibrations. **f-g**, Raman spectra collected across the interface for the TFSI$^-$ vibrations (**f**) and for OH vibrations (**g**) of the 5m LiTFSI – 10m LiCl system. The color of plots matches that in (**e**). **h**, The normalized intensity of OH (green) and TFSI$^-$ (orange) vibrations across the interface of the 5m LiTFSI – 10m LiCl system.

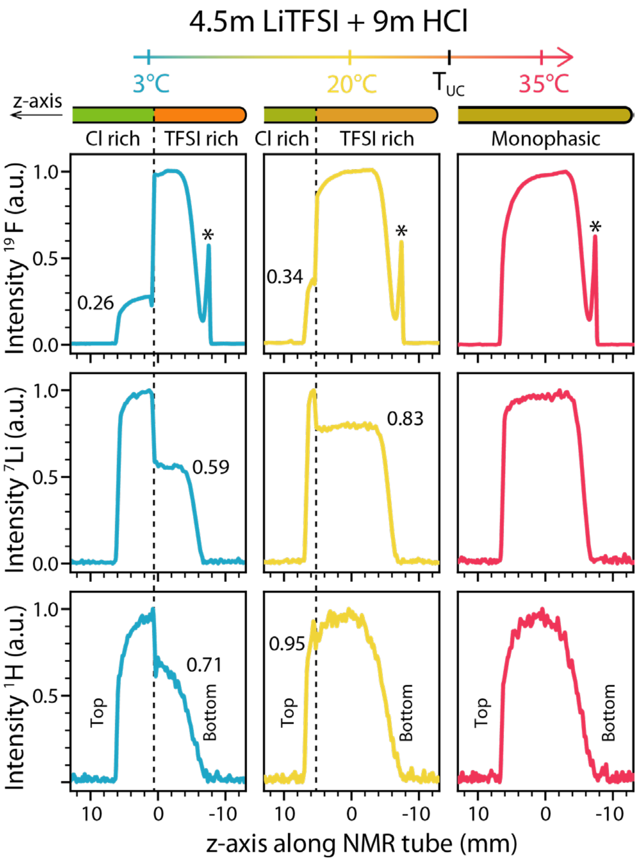

Fig. IV-S9. Variable temperature nuclear magnetic resonance analysis of the 4.5m LiTFSI - 9m HCl systems at 3°C (blue), 20°C (yellow) and 35°C (red) for the nucleus ^{19}F (top), ^{7}Li (middle) and ^{1}H (bottom) along the height of the NMR tube from left (top of the tube) to right (bottom of the tube).

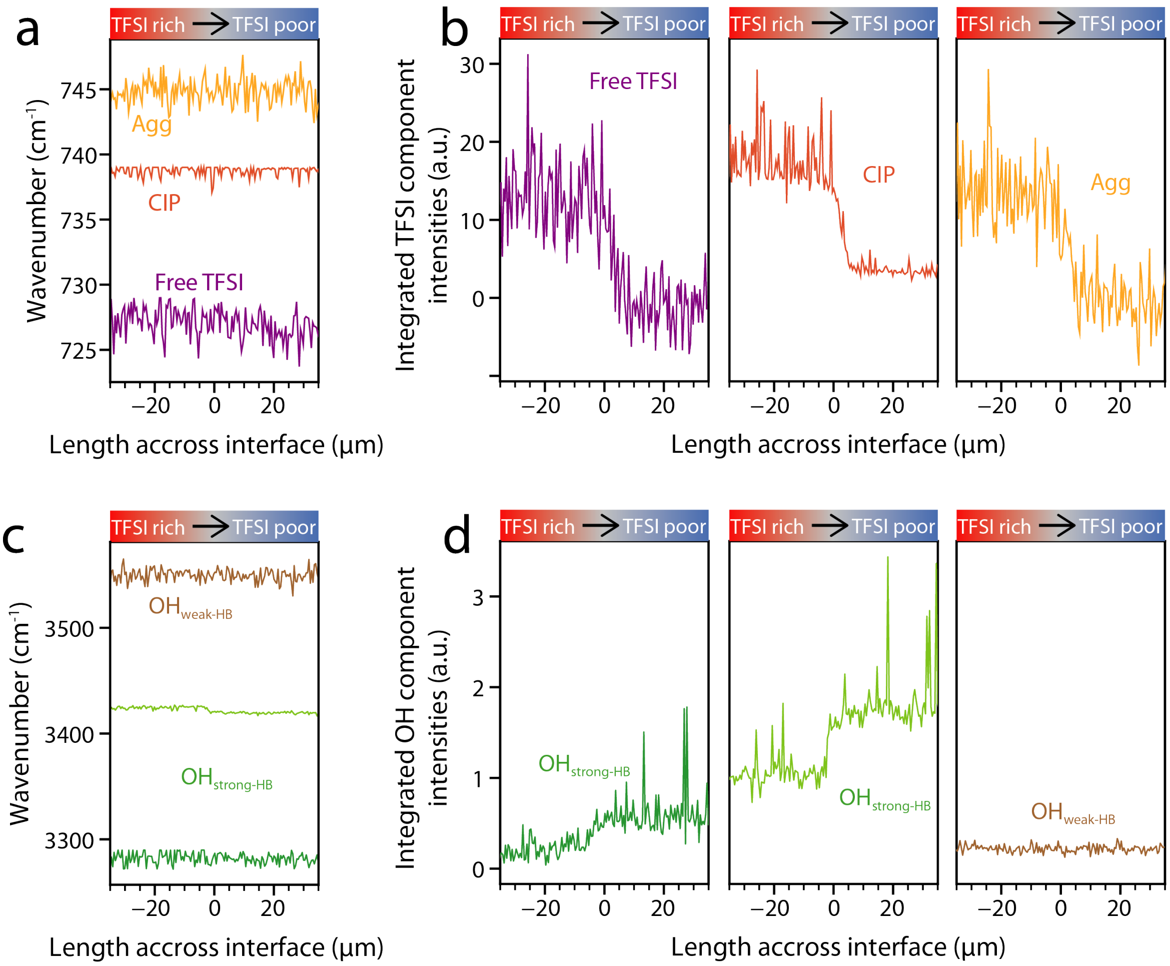

Fig. IV-S10. Peak decomposition for OH and TFSI$^-$ vibrations at 5m LiTFSI – 10m HCl along the interface. a, TFSI$^-$ components wavenumbers along the interface for free TFSI$^-$ in purple, contact ion pair in orange and aggregate in yellow. **b,** TFSI$^-$ components integrated intensities along the interface. The colors matches that in (**a**). **c,** OH components wavenumbers along the interface for OH$_{\text{strong-HB}}$ in light and dark green and OH$_{\text{weak-HB}}$ in brown. **d,** OH components integrated intensities along the interface. The colors matches that in (**c**).

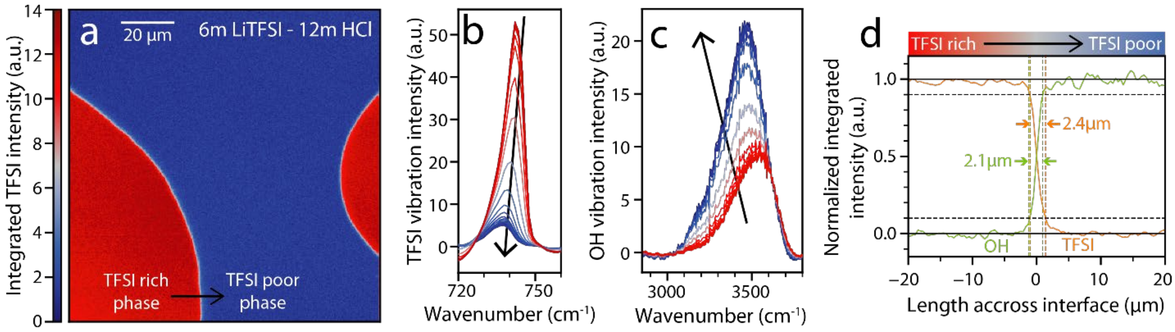

Fig. IV-S11. Raman imaging across the interface of the 6m LiTFSI – 12m HCl system. a, Raman imaging of the 6m LiTFSI – 12m HCl system generated by integration of the TFSI$^-$ vibrations. **b-c**, Raman spectra collected across the interface for the TFSI$^-$ vibrations (**b**) and for OH vibrations (**c**) The color of plots matches that in (**a**). **d**, The normalized intensity of OH (green) and TFSI$^-$ (orange) vibrations across the interface.

S-V. Supplementary information for Chapter V

Materials and Methods for Chapter V

Materials. Lithium bis(trifluoromethanesulfonyl)imide (LiTFSI Extra dry, Solvionic, 99.9%), Lithium chloride (LiCl anhydrous, Alfa Aesar, 99%), were weighted and Milli-Q water was added to reach the desired concentrations. Tetrabutylammonium tetraphenylborate (TBATPB, 99% Sigma-Aldrich) was weighted to reach the desired concentration in Dichloroethane (DCE, 99%, Alfa Aesar).

Design and machining of the liquid-liquid electrochemical cell. The design of the cell was inspired by the work of Girault et *al*.[69] and drawn with the Salome 9.9.0 software.[215] The cell was machined out of PEEK and Stainless-steel 316 at the machine shop of College de France and completed with fluorocarbon rubber (FKM) O-rings to ensure a leak-proof and chemical resistant device.

Kapton film laser ablation. Laser ablation micro-hole on polyimide film (Kapton, 8 µm) were made using a 193 nm excimer laser (Applied Spectra, Resolution-SE) with 50 laser pulses of 5 ns width at a fluence of 15 $J.cm^{-2}$ and a frequency of 15 Hz, selecting the aimed round shaped hole diameter. The holes where then controlled and measured with a microscope (Swift, SW380B, objective lenses 4X/0.10) and micrometer calibration slide (MUHWA, MH-SM05).

AgCl/Ag wire electrodes. AgCl/Ag wire electrodes were prepared by oxidizing a silver wire (Ag, Alfa Aesar, 99.9%, 0.5mm diameter) at constant current (i = 100 µA) for 1 hour in 1 $mol.L^{-1}$ hydrochloric acid (HCl, Sigma-Aldrich, 30%, Suprapur) using a three-electrode setup with a SCE as RE and a Pt gauze in a fritted isolation compartment as CE.

Cyclic voltammetry. Data were acquired on a Biologic VSP potentiostat at scan rates between 10 $mV.s^{-1}$ and 50 $mV.s^{-1}$ using a two electrode configuration with AgCl/Ag wire electrodes. The potential are corrected according to the TPAsTPB assumption as stated in **Chapter I**, part **I.C**, assuming an ion transfer from the aqueous phase to the organic phase of -230 mV and 365 mV for TBA^+ and TPB^- respectively.

References

1. Chapter 2 - Changing State of the Climate System. in *Climate Change 2021 – The Physical Science Basis: Working Group I Contribution to the Sixth Assessment Report of the Intergovernmental Panel on Climate Change* (Cambridge University Press, 2023).
2. Summary for Policymakers. in *Climate Change 2021 – The Physical Science Basis: Working Group I Contribution to the Sixth Assessment Report of the Intergovernmental Panel on Climate Change* (Cambridge University Press, 2023).
3. Summary for Policymakers. in *Climate Change 2022 – Impacts, Adaptation and Vulnerability: Working Group II Contribution to the Sixth Assessment Report of the Intergovernmental Panel on Climate Change* (Cambridge University Press, 2023).
4. International Energy Agency (IEA). World Energy Outlook 2022. (2022).
5. International Energy Agency (IEA). Global Hydrogen Review 2022. (2022).
6. 100MW Dalian Liquid Flow Battery Energy Storage and Peak shaving Power Station Connected to the Grid for Power Generation. *China Energy Storage Alliance* http://en.cnesa.org/new-blog/2022/12/22/100mw-dalian-liquid-flow-battery-energy-storage-and-peak-shaving-power-station-connected-to-the-grid-for-power-generation, Accessed July 18th 2023 (2022).
7. Yang, C. *et al.* Aqueous Li-ion battery enabled by halogen conversion–intercalation chemistry in graphite. *Nature* **569**, 245–250 (2019).
8. Goodenough, J. B. & Park, K.-S. The Li-Ion Rechargeable Battery: A Perspective. *J. Am. Chem. Soc.* **135**, 1167–1176 (2013).
9. Insinna, T. *et al.* Graphite Anodes for Li-Ion Batteries: An Electron Paramagnetic Resonance Investigation. *Chem. Mater.* **35**, 5497–5511 (2023).

10. Liu, Q. *et al.* Kinetically Determined Phase Transition from Stage II (LiC12) to Stage I (LiC6) in a Graphite Anode for Li-Ion Batteries. *J. Phys. Chem. Lett.* **9**, 5567–5573 (2018).

11. Peled, E. & Menkin, S. Review—SEI: Past, Present and Future. *J. Electrochem. Soc.* **164**, A1703–A1719 (2017).

12. Noh, H.-J., Youn, S., Yoon, C. S. & Sun, Y.-K. Comparison of the structural and electrochemical properties of layered Li[NixCoyMnz]O2 (x = 1/3, 0.5, 0.6, 0.7, 0.8 and 0.85) cathode material for lithium-ion batteries. *Journal of Power Sources* **233**, 121–130 (2013).

13. Li, W., Erickson, E. M. & Manthiram, A. High-nickel layered oxide cathodes for lithium-based automotive batteries. *Nat Energy* **5**, 26–34 (2020).

14. Yuan, L.-X. *et al.* Development and challenges of $LiFePO_4$ cathode material for lithium-ion batteries. *Energy Environ. Sci.* **4**, 269–284 (2011).

15. SDS, Lithium hexafluorophosphate solution in ethylene carbonate and dimethyl carbonate, 1.0 M LiPF6 in EC/DMC=50/50 (v/v), Product Number: 746711, Sigma-Aldrich, https://www.sigmaaldrich.com/US/en/sds/aldrich/746711, (accessed June 8th, 2023).

16. Lide, D. R. *et al.* CRC Handbook of Chemistry and Physics. (2005).

17. Koper, M. T. M. Theory of multiple proton–electron transfer reactions and its implications for electrocatalysis. *Chem. Sci.* **4**, 2710 (2013).

18. Kim, H. *et al.* Aqueous Rechargeable Li and Na Ion Batteries. *Chem. Rev.* **114**, 11788–11827 (2014).

19. Liang, Y. & Yao, Y. Designing modern aqueous batteries. *Nat Rev Mater* **8**, 109–122 (2023).

20. Koper, M. T. M. Thermodynamic theory of multi-electron transfer reactions: Implications for electrocatalysis. *Journal of Electroanalytical Chemistry* **660**, 254–260 (2011).

21. Cano, Z. P. *et al.* Batteries and fuel cells for emerging electric vehicle markets. *Nat Energy* **3**, 279–289 (2018).

22. May, G. J., Davidson, A. & Monahov, B. Lead batteries for utility energy storage: A review. *Journal of Energy Storage* **15**, 145–157 (2018).

23. Sui, Y. & Ji, X. Anticatalytic Strategies to Suppress Water Electrolysis in Aqueous Batteries. *Chem. Rev.* (2021) doi:10.1021/acs.chemrev.1c00191.

24. Li, W., Dahn, J. R. & Wainwright, D. S. Rechargeable Lithium Batteries with Aqueous Electrolytes. *Science* **264**, 1115–1118 (1994).

25. Suo, L. *et al.* “Water-in-salt” electrolyte enables high-voltage aqueous lithium-ion chemistries. *Science* **350**, 938–943 (2015).

26. Borodin, O., Self, J., Persson, K. A., Wang, C. & Xu, K. Uncharted Waters: Super-Concentrated Electrolytes. *Joule* **4**, 69–100 (2020).

27. Yamada, Y. *et al.* Hydrate-melt electrolytes for high-energy-density aqueous batteries. *Nature Energy* **1**, 1–9 (2016).

28. Suo, L. *et al.* Advanced High-Voltage Aqueous Lithium-Ion Battery Enabled by “Water-in-Bisalt” Electrolyte. *Angewandte Chemie* **128**, 7252–7257 (2016).

29. Xie, J., Liang, Z. & Lu, Y.-C. Molecular crowding electrolytes for high-voltage aqueous batteries. *Nature Materials* **19**, 1006–1011 (2020).

30. Droguet, L. *et al.* Can an Inorganic Coating Serve as Stable SEI for Aqueous Superconcentrated Electrolytes? *ACS Energy Lett.* **6**, 2575–2583 (2021).

31. Droguet, L., Grimaud, A., Fontaine, O. & Tarascon, J.-M. Water-in-Salt Electrolyte (WiSE) for Aqueous Batteries: A Long Way to Practicality. *Advanced Energy Materials* **10**, 2002440 (2020).

32. Yang, C. *et al.* 4.0 V Aqueous Li-Ion Batteries. *Joule* **1**, 122–132 (2017).

33. Dubouis, N. *et al.* Chasing Aqueous Biphasic Systems from Simple Salts by Exploring the LiTFSI/LiCl/H2O Phase Diagram. *ACS Cent. Sci.* **5**, 640–643 (2019).

34. Dahn, J. R. & Seel, J. A. Energy and Capacity Projections for Practical Dual-Graphite Cells. *J. Electrochem. Soc.* **147**, 899 (2000).

35. Liu, H. *et al.* A Zinc–Dual-Halogen Battery with a Molten Hydrate Electrolyte. *Advanced Materials* **32**, 2004553 (2020).

36. Ejigu, A., Le Fevre, L. W. & Dryfe, R. A. W. Reversible Electrochemical Energy Storage Based on Zinc-Halide Chemistry. *ACS Applied Materials and Interfaces* **13**, 14112–14121 (2021).

37. Cai, S. *et al.* Water–Salt Oligomers Enable Supersoluble Electrolytes for High-Performance Aqueous Batteries. *Advanced Materials* **33**, 2007470 (2021).

38. Guo, Q. *et al.* Reversible Insertion of I–Cl Interhalogen in a Graphite Cathode for Aqueous Dual-Ion Batteries. *ACS Energy Lett.* **6**, 459–467 (2021).

39. Bard, A. J. & Faulkner, L. R. *Electrochemical Methods: Fundamentals and Applications, 2nd Edition*. (2000).

40. Thiam, B. G. & Vaudreuil, S. Review—Recent Membranes for Vanadium Redox Flow Batteries. *J. Electrochem. Soc.* **168**, 070553 (2021).

41. Tang, L. *et al.* Capital cost evaluation of conventional and emerging redox flow batteries for grid storage applications. *Electrochimica Acta* **437**, 141460 (2023).

42. Zeng, L., Zhao, T. S., Wei, L., Jiang, H. R. & Wu, M. C. Anion exchange membranes for aqueous acid-based redox flow batteries: Current status and challenges. *Applied Energy* **233–234**, 622–643 (2019).

43. Jones, B. E. *Electric Primary Batteries: A Practical Guide to Their Construction and Use*. (Cassell and Company, 1911).

44. Ferrigno, R., Stroock, A. D., Clark, T. D., Mayer, M. & Whitesides, G. M. Membraneless Vanadium Redox Fuel Cell Using Laminar Flow. *J. Am. Chem. Soc.* **124**, 12930–12931 (2002).

45. Choban, E. R., Markoski, L. J., Wieckowski, A. & Kenis, P. J. A. Microfluidic fuel cell based on laminar flow. *Journal of Power Sources* **128**, 54–60 (2004).

46. Kjeang, E., Michel, R., Harrington, D. A., Djilali, N. & Sinton, D. A Microfluidic Fuel Cell with Flow-Through Porous Electrodes. *J. Am. Chem. Soc.* **130**, 4000–4006 (2008).

47. Lee, J. W., Goulet, M.-A. & Kjeang, E. Microfluidic redox battery. *Lab Chip* **13**, 2504–2507 (2013).

48. Braff, W. A., Bazant, M. Z. & Buie, C. R. Membrane-less hydrogen bromine flow battery. *Nat Commun* **4**, 2346 (2013).

49. Bamgbopa, M. O., Almheiri, S. & Sun, H. Prospects of recently developed membraneless cell designs for redox flow batteries. *Renewable and Sustainable Energy Reviews* **70**, 506–518 (2017).

50. Kim, H. *et al.* Liquid Metal Batteries: Past, Present, and Future. *Chem. Rev.* **113**, 2075–2099 (2013).

51. Gong, K. *et al.* Exploiting Immiscible Aqueous-Nonaqueous Electrolyte Interface toward a Membraneless Redox-Flow Battery Concept. *J. Electrochem. Soc.* **164**, A2590 (2017).

52. Molina-Osorio, A. F., Gamero-Quijano, A., Peljo, P. & Scanlon, M. D. Membraneless energy conversion and storage using immiscible electrolyte solutions. *Current Opinion in Electrochemistry* **21**, 100–108 (2020).

53. Gong, K., Fang, Q., Gu, S., Yau Li, S. F. & Yan, Y. Nonaqueous redox-flow batteries: organic solvents, supporting electrolytes, and redox pairs. *Energy & Environmental Science* **8**, 3515–3530 (2015).

54. Meng, J. *et al.* A Stirred Self-Stratified Battery for Large-Scale Energy Storage. *Joule* **4**, 953–966 (2020).

55. Bamgbopa, M. O., Shao-Horn, Y., Hashaikeh, R. & Almheiri, S. Cyclable membraneless redox flow batteries based on immiscible liquid electrolytes: Demonstration with all-iron redox chemistry. *Electrochimica Acta* **267**, 41–50 (2018).

56. Navalpotro, P., Palma, J., Anderson, M. & Marcilla, R. A Membrane-Free Redox Flow Battery with Two Immiscible Redox Electrolytes. *Angewandte Chemie International Edition* **56**, 12460–12465 (2017).

57. Navalpotro, P. *et al.* Exploring the Versatility of Membrane-Free Battery Concept Using Different Combinations of Immiscible Redox Electrolytes. *ACS Appl. Mater. Interfaces* **10**, 41246–41256 (2018).

58. Chai, J. *et al.* Biphasic, Membrane-Free Zn/Phenothiazine Battery: Effects of Hydrophobicity of Redox Materials on Cyclability. *ACS Materials Lett.* **3**, 337–343 (2021).

59. Wang, Z. *et al.* Exploiting nonaqueous self-stratified electrolyte systems toward large-scale energy storage. *Nat Commun* **14**, 2267 (2023).

60. Gschwend, G. C., Olaya, A., Peljo, P. & Girault, H. H. Structure and reactivity of the polarised liquid–liquid interface: what we know and what we do not. *Current Opinion in Electrochemistry* **19**, 137–143 (2020).

61. Gavach, C., Mlodnicka, T. & Guastalla, J. Sur la possibilité de phénomènes de surtension à l'interface entre solutions organiques et solutions aqueuses. *Comptes Rendus de l'Académie des sciences* **266, Serie C**, 1196–1999 (1968).

62. Samec, Z., Mareček, V. & Weber, J. Detection of an electron transfer across the interface between two immiscible electrolyte solutions by cyclic voltammetry with four-electrode system. *Journal of Electroanalytical Chemistry and Interfacial Electrochemistry* **96**, 245–247 (1979).

63. Samec, Z. Electrochemistry at the interface between two immiscible electrolyte solutions (IUPAC Technical Report). *Pure and Applied Chemistry* **76**, 2147–2180 (2004).

64. Shao, Y. 17.3 - Electrochemistry at Liquid/Liquid interfaces. in *Handbook of Electrochemistry* 785–809 (Elsevier, 2007).

65. Vanýsek, P. *Electrochemistry on Liquid/Liquid Interfaces*. vol. 39 (Springer, 1985).

66. Aarts, D. G. A. L., Schmidt, M. & Lekkerkerker, H. N. W. Direct Visual Observation of Thermal Capillary Waves. *Science* **304**, 847–850 (2004).

67. Luo, G. *et al.* Ion Distributions near a Liquid-Liquid Interface. *Science* **311**, 216–218 (2006).

68. Gschwend, G. C. & Girault, H. H. Discrete Helmholtz charge distribution at liquid-liquid interfaces: Electrocapillarity, capacitance and non-linear spectroscopy studies. *Journal of Electroanalytical Chemistry* **872**, 114240 (2020).

69. Gschwend, G. C. & Girault, H. H. Discrete Helmholtz model: a single layer of correlated counter-ions. Metal oxides and silica interfaces, ion-exchange and biological membranes. *Chem. Sci.* **11**, 10304–10312 (2020).

70. Gschwend, G. C., Olaya, A. & Girault, H. H. How to polarise an interface with ions: the discrete Helmholtz model. *Chem. Sci.* **11**, 10807–10813 (2020).

71. Mareček, V. & Samec, Z. Ion transfer kinetics at the interface between two immiscible electrolyte solutions supported on a thick-wall micro-capillary. A mini review. *Current Opinion in Electrochemistry* **1**, 133–139 (2017).

72. Kikkawa, N., Wang, L. & Morita, A. Microscopic Barrier Mechanism of Ion Transport through Liquid–Liquid Interface. *J. Am. Chem. Soc.* **137**, 8022–8025 (2015).

73. Laforge, F. O., Sun, P. & Mirkin, M. V. Shuttling Mechanism of Ion Transfer at the Interface between Two Immiscible Liquids. *J. Am. Chem. Soc.* **128**, 15019–15025 (2006).

74. Wei, X. *et al.* Materials and Systems for Organic Redox Flow Batteries: Status and Challenges. *ACS Energy Lett.* **2**, 2187–2204 (2017).

75. Li, X., Qin, Z., Deng, Y., Wu, Z. & Hu, W. Development and Challenges of Biphasic Membrane-Less Redox Batteries. *Advanced Science* **9**, 2105468 (2022).

76. Yang, C. *et al.* Unique aqueous Li-ion/sulfur chemistry with high energy density and reversibility. *PNAS* **114**, 6197–6202 (2017).

77. Navalpotro, P. *et al.* Pioneering Use of Ionic Liquid-Based Aqueous Biphasic Systems as Membrane-Free Batteries. *Advanced Science* **5**, 1800576 (2018).

78. Navalpotro, P., Ibañez, S. E., Pedraza, E. & Marcilla, R. A neutral pH aqueous biphasic system applied to both static and flow membrane-free battery. *Energy Storage Materials* **56**, 403–411 (2023).

79. Albertsson, P.-Å. Partition of Cell Particles and Macromolecules in Polymer Two-Phase Systems. in *Advances in Protein Chemistry* vol. 24 309–341 (Academic Press, 1970).

80. Grinberg, V. Ya. & Tolstoguzov, V. B. Thermodynamic compatibility of gelatin with some D-glucans in aqueous media. *Carbohydrate Research* **25**, 313–321 (1972).

81. van Oss, C. J., Chaudhury, M. K. & Good, R. J. Monopolar surfaces. *Advances in Colloid and Interface Science* **28**, 35–64 (1987).

82. Dobry, A. & Boyer-Kawenoki, F. Phase separation in polymer solution. *Journal of Polymer Science* **2**, 90–100 (1947).

83. Diamond, A. D. & Hsu, J. T. Phase diagrams for dextran-PEG aqueous two-phase systems at 22°C. *Biotechnol Tech* **3**, 119–124 (1989).

84. Johansson, H.-O., Karlström, G., Tjerneld, F. & Haynes, C. A. Driving forces for phase separation and partitioning in aqueous two-phase systems. *Journal of Chromatography B: Biomedical Sciences and Applications* **711**, 3–17 (1998).

85. Zaslavsky, B. Yu. *et al.* Structure of water as a key factor of phase separation in aqueous mixtures of two nonionic polymers. *Polymer* **30**, 2104–2111 (1989).

86. Pereira, J. F. B. & Coutinho, J. A. P. Aqueous Two-Phase Systems. in *Liquid-Phase Extraction* 157–182 (Elsevier, 2020).

87. Albertsson, P.-Å. Partition of Proteins in Liquid Polymer–Polymer Two-Phase Systems. *Nature* **182**, 709–711 (1958).

88. Mace, C. R. *et al.* Aqueous Multiphase Systems of Polymers and Surfactants Provide Self-Assembling Step-Gradients in Density. *J. Am. Chem. Soc.* **134**, 9094–9097 (2012).

89. Albertsson, P.-Å. Chromatography and Partition of Cells and Cell Fragments. *Nature* **177**, 771–774 (1956).

90. Huddleston, J. G., Willauer, H. D. & Rogers, R. D. Phase Diagram Data for Several PEG + Salt Aqueous Biphasic Systems at 25 °C. *J. Chem. Eng. Data* **48**, 1230–1236 (2003).

91. Ananthapadmanabhan, K. P. & Goddard, E. D. Aqueous biphase formation in polyethylene oxide-inorganic salt systems. *Langmuir* **3**, 25–31 (1987).

92. Kang, B., Tang, H., Zhao, Z. & Song, S. Hofmeister Series: Insights of Ion Specificity from Amphiphilic Assembly and Interface Property. *ACS Omega* **5**, 6229–6239 (2020).

93. Collins, K. D. Charge density-dependent strength of hydration and biological structure. *Biophysical Journal* **72**, 65–76 (1997).

94. Collins, K. D. Why continuum electrostatics theories cannot explain biological structure, polyelectrolytes or ionic strength effects in ion–protein interactions. *Biophysical Chemistry* **167**, 43–59 (2012).

95. Jenkins, H. D. B. & Marcus, Y. Viscosity B-Coefficients of Ions in Solution. *Chem. Rev.* **95**, 2695–2724 (1995).

96. da Silva, L. H. M. & Loh, W. Calorimetric Investigation of the Formation of Aqueous Two-Phase Systems in Ternary Mixtures of Water, Poly(ethylene oxide) and Electrolytes (Or Dextran). *J. Phys. Chem. B* **104**, 10069–10073 (2000).

97. Zafarani-Moattar, M. T. & Hosseinpour-Hashemi, V. Effect of Temperature on the Aqueous Two-Phase System Containing Poly(ethylene glycol) Dimethyl Ether 2000 and Dipotassium Oxalate. *J. Chem. Eng. Data* **57**, 532–540 (2012).

98. Marcus, Y. Thermodynamics of solvation of ions. Part 5.—Gibbs free energy of hydration at 298.15 K. *Journal of the Chemical Society, Faraday Transactions* **87**, 2995–2999 (1991).

99. Gutowski, K. E. *et al.* Controlling the Aqueous Miscibility of Ionic Liquids: Aqueous Biphasic Systems of Water-Miscible Ionic Liquids and Water-Structuring Salts for Recycle, Metathesis, and Separations. *J. Am. Chem. Soc.* **125**, 6632–6633 (2003).

100. Bridges, N. J., Gutowski, K. E. & Rogers, R. D. Investigation of aqueous biphasic systems formed from solutions of chaotropic salts with kosmotropic salts (salt–salt ABS). *Green Chem.* **9**, 177–183 (2007).

101. Shahriari, S., Neves, C. M. S. S., Freire, M. G. & Coutinho, J. A. P. Role of the Hofmeister Series in the Formation of Ionic-Liquid-Based Aqueous Biphasic Systems. *J. Phys. Chem. B* **116**, 7252–7258 (2012).

102. Freire, M. G. *et al.* Aqueous biphasic systems: a boost brought about by using ionic liquids. *Chem. Soc. Rev.* **41**, 4966–4995 (2012).

103. Passos, H., V. Dinis, T. B., M. Cláudio, A. F., G. Freire, M. & P. Coutinho, J. A. Hydrogen bond basicity of ionic liquids and molar entropy of hydration of salts as major descriptors in the formation of aqueous biphasic systems. *Physical Chemistry Chemical Physics* **20**, 14234–14241 (2018).

104. Cláudio, A. F. M., Ferreira, A. M., Shahriari, S., Freire, M. G. & Coutinho, J. A. P. Critical Assessment of the Formation of Ionic-Liquid-Based Aqueous Two-Phase Systems in Acidic Media. *J. Phys. Chem. B* **115**, 11145–11153 (2011).

105. Ventura, S. P. M. *et al.* Evaluation of Anion Influence on the Formation and Extraction Capacity of Ionic-Liquid-Based Aqueous Biphasic Systems. *J. Phys. Chem. B* **113**, 9304–9310 (2009).

106. Mourão, T., Cláudio, A. F. M., Boal-Palheiros, I., Freire, M. G. & Coutinho, J. A. P. Evaluation of the impact of phosphate salts on the formation of ionic-liquid-based aqueous biphasic systems. *The Journal of Chemical Thermodynamics* **54**, 398–405 (2012).

107. Dubouis, N., France-Lanord, A., Brige, A., Salanne, M. & Grimaud, A. Anion Specific Effects Drive the Formation of Li-Salt Based Aqueous Biphasic Systems. *J. Phys. Chem. B* **125**, 5365–5372 (2021).

108. Marcus, Y. & Loewenschuss, A. Chapter 4. Standard entropies of hydration of ions. *Annu. Rep. Prog. Chem., Sect. C: Phys. Chem.* **81**, 81–135 (1984).

109. Pike, S. J., Hutchinson, J. J. & Hunter, C. A. H-Bond Acceptor Parameters for Anions. *J. Am. Chem. Soc.* **139**, 6700–6706 (2017).

110. Li, Z. *et al.* Transport Properties of Li-TFSI Water-in-Salt Electrolytes. *J. Phys. Chem. B* **123**, 10514–10521 (2019).

111. Wu, X. *et al.* Electrical Conductivity of Lithium Chloride, Lithium Bromide, and Lithium Iodide Electrolytes in Methanol, Water, and Their Binary Mixtures. *J. Chem. Eng. Data* **64**, 4319–4329 (2019).

112. Ellis, R. J. & Minton, A. P. Join the crowd. *Nature* **425**, 27–28 (2003).

113. Rösgen, J., Pettitt, B. M. & Bolen, D. W. Protein Folding, Stability, and Solvation Structure in Osmolyte Solutions. *Biophysical Journal* **89**, 2988–2997 (2005).

114. Ball, P. Water as an Active Constituent in Cell Biology. *Chem. Rev.* **108**, 74–108 (2008).

115. Zheng, J. *et al.* Understanding Thermodynamic and Kinetic Contributions in Expanding the Stability Window of Aqueous Electrolytes. *Chem* **4**, 2872–2882 (2018).

116. McEldrew, M., Goodwin, Z. A. H., Kornyshev, A. A. & Bazant, M. Z. Theory of the Double Layer in Water-in-Salt Electrolytes. *J. Phys. Chem. Lett.* **9**, 5840–5846 (2018).

117. Han, K. S. *et al.* Origin of Unusual Acidity and Li+ Diffusivity in a Series of Water-in-Salt Electrolytes. *J. Phys. Chem. B* **124**, 5284–5291 (2020).

118. Hubert, H. G. *Analytical and Physical Electrochemistry*. (2004).

119. Hasted, J. B., Ritson, D. M. & Collie, C. H. Dielectric Properties of Aqueous Ionic Solutions. Parts I and II. *J. Chem. Phys.* **16**, 1–21 (1948).

120. Levy, A., Bazant, M. & Kornyshev, A. Ionic activity in concentrated electrolytes: Solvent structure effect revisited. *Chemical Physics Letters* **738**, 136915 (2020).

121. Marcus, Y. & Hefter, G. Ion Pairing. *Chem. Rev.* **106**, 4585–4621 (2006).

122. Borodin, O. *et al.* Liquid Structure with Nano-Heterogeneity Promotes Cationic Transport in Concentrated Electrolytes. *ACS Nano* **11**, 10462–10471 (2017).

123. Pitzer, K. S. Thermodynamics of electrolytes. I. Theoretical basis and general equations. *J. Phys. Chem.* **77**, 268–277 (1973).

124. Pitzer, K. S. & Mayorga, G. Thermodynamics of electrolytes. II. Activity and osmotic coefficients for strong electrolytes with one or both ions univalent. *J. Phys. Chem.* **77**, 2300–2308 (1973).

125. Pitzer, K. S. & Mayorga, G. Thermodynamics of electrolytes. III. Activity and osmotic coefficients for 2–2 electrolytes. *J Solution Chem* **3**, 539–546 (1974).

126. McEldrew, M., Goodwin, Z. A. H., Bi, S., Bazant, M. Z. & Kornyshev, A. A. Theory of ion aggregation and gelation in super-concentrated electrolytes. *J. Chem. Phys.* **152**, 234506 (2020).

127. Hamer, W. J. & Wu, Y. Osmotic Coefficients and Mean Activity Coefficients of Uni-univalent Electrolytes in Water at 25°C. *Journal of Physical and Chemical Reference Data* **1**, 1047–1100 (1972).

128. Wandt, J., Lee, J., Arrigan, D. W. M. & Silvester, D. S. A lithium iron phosphate reference electrode for ionic liquid electrolytes. *Electrochemistry Communications* **93**, 148–151 (2018).

129. Kühnel, R.-S., Reber, D. & Battaglia, C. Perspective—Electrochemical Stability of Water-in-Salt Electrolytes. *J. Electrochem. Soc.* **167**, 070544 (2020).

130. Wang, F. *et al.* Highly reversible zinc metal anode for aqueous batteries. *Nature Mater* **17**, 543–549 (2018).

131. Tanaka, K. & Nomura, M. Measurements of tracer diffusion coefficients of lithium ions, chloride ions and water in aqueous lithium chloride solutions. *J. Chem. Soc., Faraday Trans. 1* **83**, 1779–1782 (1987).

132. Chapman, T. W. & Newman, J. A Compilation of Selected Thermodynamic and Transport Properties of Binary Electrolytes in Aqueous Solution. (1968).

133. Lide, D. R. *et al.* CRC Handbook of Chemistry and Physics. 2661.

134. Torriero, A. A. J. & Howlett, P. C. Ionic liquid effects on the redox potential of ferrocene. *Electrochemistry Communications* **16**, 84–87 (2012).

135. Wu, J.-S., Toda, K., Tanaka, A. & Sanemasa, I. Association Constants of Ferrocene with Cyclodextrins in Aqueous Medium Determined by Solubility Measurements of Ferrocene. *BCSJ* **71**, 1615–1618 (1998).

136. Reber, D., Figi, R., Kühnel, R.-S. & Battaglia, C. Stability of aqueous electrolytes based on LiFSI and NaFSI. *Electrochimica Acta* **321**, 134644 (2019).

137. Dubouis, N. *et al.* The role of the hydrogen evolution reaction in the solid–electrolyte interphase formation mechanism for " Water-in-Salt " electrolytes. *Energy & Environmental Science* **11**, 3491–3499 (2018).

138. Dubouis, N. *et al.* Extending insertion electrochemistry to soluble layered halides with superconcentrated electrolytes. *Nat. Mater.* **20**, 1545–1550 (2021).

139. Degoulange, D., Dubouis, N. & Grimaud, A. Toward the understanding of water-in-salt electrolytes: Individual ion activities and liquid junction potentials in highly concentrated aqueous solutions. *J. Chem. Phys.* **155**, 064701 (2021).

140. Chen, H., Kaliyaraj Selva Kumar, A., Le, H. & Compton, R. G. Non-unity stoichiometric reversible electrode reactions. The effect of coupled kinetics and the oxidation of bromide. *Journal of Electroanalytical Chemistry* **876**, 114730 (2020).

141. Vos, J. G., Venugopal, A., Smith, W. A. & Koper, M. T. M. Competition and Interhalogen Formation During Parallel Electrocatalytic Oxidation of Bromide and Chloride on Pt. *J. Electrochem. Soc.* **167**, 046505 (2020).

142. Vos, J. G., Venugopal, A., Smith, W. A. & Koper, M. T. M. Competition and selectivity during parallel evolution of bromine, chlorine and oxygen on IrOx electrodes. *Journal of Catalysis* **389**, 99–110 (2020).

143. Degoulange, D. *et al.* Direct imaging of micrometer-thick interfaces in salt–salt aqueous biphasic systems. *Proceedings of the National Academy of Sciences* **120**, e2220662120 (2023).

144. Robinson, R. A. The water activities of lithium chloride solutions up to high concentrations at 25°. *Trans. Faraday Soc.* **41**, 756–758 (1945).

145. Thermodynamics of Cl-H2O, Br-H2O, I-H2O, Au-Cl-H2O, Au-Br-H2O and Au-I-H2O systems at 298 K. *Journal of Electroanalytical Chemistry* **361**, 13–24 (1993).

146. Awtrey, A. D. & Connick, R. E. The Absorption Spectra of I_2, I_3^-, I^-, IO_3^-, $S_4O_6^=$ and $S_2O_3^=$. Heat of the Reaction $I_3^- = I_2 + I^-$. *J. Am. Chem. Soc.* **73**, 1842–1843 (1951).

147. Popov, A. I. & Swensen, R. F. Studies on the Chemistry of Halogens and of Polyhalides. V. Spectrophotometric Study of Polyhalogen Complexes in Acetonitrile and in Ethylene Dichloride. *J. Am. Chem. Soc.* **77**, 3724–3726 (1955).

148. Seery, D. J. & Britton, D. The Continuous Absorption Spectra of Chlorine, Bromine, Bromine Chloride, Iodine Chloride, and Iodine Bromide. *J. Phys. Chem.* **68**, 2263–2266 (1964).

149. Gabes, W. & Stufkens, D. J. Electronic absorption spectra of symmetrical and asymmetrical trihalide ions. *Spectrochimica Acta Part A: Molecular Spectroscopy* **30**, 1835–1841 (1974).

150. Wang, T. X., Kelley, M. D., Cooper, J. N., Beckwith, R. C. & Margerum, D. W. Equilibrium, Kinetic, and UV-Spectral Characteristics of Aqueous Bromine Chloride, Bromine, and Chlorine Species. *Inorg. Chem.* **33**, 5872–5878 (1994).

151. Cotton. *ADVANCED INORGANIC CHEMISTRY, 6TH ED.* (Wiley India Pvt. Limited, 2007).

152. Rodríguez-Carvajal, J. Recent advances in magnetic structure determination by neutron powder diffraction. *Physica B: Condensed Matter* **192**, 55–69 (1993).

153. Sasa, T., Takahashi, Y. & Mukaibo, T. Crystal structure of graphite bromine lamellar compounds. *Carbon* **9**, 407–416 (1971).

154. Xu, J. *et al.* Lithium halide cathodes for Li metal batteries. *Joule* **7**, 83–94 (2023).

155. Dresselhaus, M. S. & Dresselhaus, G. Intercalation compounds of graphite. *Advances in Physics* **51**, 1–186 (2002).

156. Gaier, J. R., Ditmars, N. F. & Dillon, A. R. Aqueous electrochemical intercalation of bromine into graphite fibers. *Carbon* **43**, 189–193 (2005).

157. Yin, Y., Yuan, Z. & Li, X. Rechargeable aqueous zinc–bromine batteries: an overview and future perspectives. *Physical Chemistry Chemical Physics* **23**, 26070–26084 (2021).

158. Navalpotro, P. *et al.* Critical aspects of membrane-free aqueous battery based on two immiscible neutral electrolytes. *Energy Storage Materials* **26**, 400–407 (2020).

159. Ding, P. *et al.* Interfacial Tension in Phase-Separated Gelatin/Dextran Aqueous Mixtures. *Journal of Colloid and Interface Science* **253**, 367–376 (2002).

160. Tromp, R. H., Vis, M., Erné, B. H. & Blokhuis, E. M. Composition, concentration and charge profiles of water–water interfaces. *J. Phys.: Condens. Matter* **26**, 464101 (2014).

161. Vis, M., Erné, B. H. & Tromp, R. H. Chemical physics of water–water interfaces. *Biointerphases* **11**, 018904 (2016).

162. Phakoukaki, Y.-V., O'Shaughnessy, P. & Angeli, P. Flow patterns of ionic liquid based aqueous biphasic systems in small channels. *Chemical Engineering Science* **265**, 118197 (2023).

163. Atkins, P. W. & De Paula, J. *Physical chemistry*. (W.H. Freeman, 2006).

164. Girault, H. H. Charge Transfer across Liquid—Liquid Interfaces. in *Modern Aspects of Electrochemistry: Volume 25* 1–62 (Springer US, 1993).

165. Solomon, T. & Bard, A. J. Reverse (Uphill) Electron Transfer at the Liquid/Liquid Interface. *J. Phys. Chem.* **99**, 17487–17489 (1995).

166. Peljo, P., Smirnov, E. & Girault, Hubert. H. Heterogeneous versus homogeneous electron transfer reactions at liquid–liquid interfaces: The wrong question? *Journal of Electroanalytical Chemistry* **779**, 187–198 (2016).

167. Kong, Y.-T., Imabayashi, S. & Kakiuchi, T. Two-Phase Azo-Coupling Reactions Driven by Phase-Boundary Potential Across the Liquid|Liquid Interface. *J. Am. Chem. Soc.* **122**, 8215–8219 (2000).

168. Lehane, R. A. *et al.* Electrosynthesis of Biocompatible Free-Standing PEDOT Thin Films at a Polarized Liquid|Liquid Interface. *J. Am. Chem. Soc.* **144**, 4853–4862 (2022).

169. Harkins, W. D. & Brown, F. E. The determination of surface tension (free surface energy), and the weight of falling drops: the surface tension of water and benzene by capillary height method. *J. Am. Chem. Soc.* **41**, 499–524 (1919).

170. Vis, M. *et al.* Decreased Interfacial Tension of Demixed Aqueous Polymer Solutions due to Charge. *Phys. Rev. Lett.* **115**, 078303 (2015).

171. Carey, D. M. & Korenowski, G. M. Measurement of the Raman spectrum of liquid water. *J. Chem. Phys.* **108**, 2669–2675 (1998).

172. Xiao, D. *et al.* Optimization of Organic/Water Hybrid Electrolytes for High-Rate Carbon-Based Supercapacitor. *Advanced Functional Materials* **29**, 1904136 (2019).

173. Tsurumura, T., Hashimoto, Y., Morita, M., Umebayashi, Y. & Fujii, K. Anion Coordination Characteristics of Ion-pair Complexes in Highly Concentrated Aqueous Lithium Bis(trifluoromethanesulfonyl)amide Electrolytes. *Analytical Sciences* **35**, 289–294 (2019).

174. Sandler, S. I. *Models for Thermodynamic and Phase Equilibria Calculations*. (Taylor & Francis, 1993).

175. Henderson, W. A. *et al.* Electrolyte Solvation and Ionic Association: VIII. Reassessing Raman Spectroscopic Studies of Ion Coordination for LiTFSI. *J. Electrochem. Soc.* **169**, 060515 (2022).

176. Watkins, T. & Buttry, D. A. Determination of Mg2+ Speciation in a TFSI–-Based Ionic Liquid With and Without Chelating Ethers Using Raman Spectroscopy. *J. Phys. Chem. B* **119**, 7003–7014 (2015).

177. Zhang, Y.-H. & Chan, C. K. Observations of Water Monomers in Supersaturated NaClO4, LiClO4, and Mg(ClO4)2 Droplets Using Raman Spectroscopy. *J. Phys. Chem. A* **107**, 5956–5962 (2003).

178. Yin, J., Zheng, C., Qi, L. & Wang, H. Concentrated NaClO4 aqueous solutions as promising electrolytes for electric double-layer capacitors. *Journal of Power Sources* **196**, 4080–4087 (2011).

179. Li, C.-Y. *et al.* Unconventional interfacial water structure of highly concentrated aqueous electrolytes at negative electrode polarizations. *Nat Commun* **13**, 5330 (2022).

180. García-Garabal, S., Domínguez-Pérez, M., Portela, D., Varela, L. M. & Cabeza, O. Preliminary study of new electrolytes based on [MPPyr][TFSI] for lithium ion batteries. *Journal of Molecular Liquids* **363**, 119758 (2022).

181. Luo, G. *et al.* The width of the water/2-heptanone liquid–liquid interface. *Electrochemistry Communications* **7**, 627–630 (2005).

182. Diel, E. E., Lichtman, J. W. & Richardson, D. S. Tutorial: avoiding and correcting sample-induced spherical aberration artifacts in 3D fluorescence microscopy. *Nat Protoc* **15**, 2773–2784 (2020).

183. Kang, H. *et al.* Molecular insight into the lower critical solution temperature transition of aqueous alkyl phosphonium benzene sulfonates. *Commun Chem* **2**, 1–11 (2019).

184. Meyer, G. *et al.* How Temperature Rise Can Induce Phase Separation in Aqueous Biphasic Solutions. *J. Phys. Chem. Lett.* **13**, 2731–2736 (2022).

185. Hamer, W. J. & Wu, Y. Osmotic Coefficients and Mean Activity Coefficients of Uni-univalent Electrolytes in Water at 25°C. *Journal of Physical and Chemical Reference Data* **1**, 1047–1100 (1972).

186. Abdulagatov, I. M. & Azizov, N. D. Densities and apparent molar volumes of concentrated aqueous LiCl solutions at high temperatures and high pressures. *Chemical Geology* **230**, 22–41 (2006).

187. Gebbie, M. A. *et al.* Ionic liquids behave as dilute electrolyte solutions. *Proceedings of the National Academy of Sciences* **110**, 9674–9679 (2013).

188. Gebbie, M. A., Dobbs, H. A., Valtiner, M. & Israelachvili, J. N. Long-range electrostatic screening in ionic liquids. *Proceedings of the National Academy of Sciences* **112**, 7432–7437 (2015).

189. Gras, M. *et al.* Ionic-Liquid-Based Acidic Aqueous Biphasic Systems for Simultaneous Leaching and Extraction of Metallic Ions. *Angewandte Chemie International Edition* **57**, 1563–1566 (2018).

190. Xiong, D., Wang, H., Li, Z. & Wang, J. Recovery of Ionic Liquids with Aqueous Two-Phase Systems Induced by Carbon Dioxide. *ChemSusChem* **5**, 2255–2261 (2012).

191. Scott, M., Blas Molinos, B., Westhues, C., Franciò, G. & Leitner, W. Aqueous Biphasic Systems for the Synthesis of Formates by Catalytic CO2 Hydrogenation: Integrated Reaction and Catalyst Separation for CO2-Scrubbing Solutions. *ChemSusChem* **10**, 1085–1093 (2017).

192. Guilbert, J. *et al.* Label-free super-resolution chemical imaging of biomedical specimens. 2021.05.14.444185 Preprint at https://doi.org/10.1101/2021.05.14.444185 (2021).

193. Shi, X., Coca-López, N., Janik, J. & Hartschuh, A. Advances in Tip-Enhanced Near-Field Raman Microscopy Using Nanoantennas. *Chem. Rev.* **117**, 4945–4960 (2017).

194. Heisler, I. A. & Meech, S. R. Low-Frequency Modes of Aqueous Alkali Halide Solutions: Glimpsing the Hydrogen Bonding Vibration. *Science* **327**, 857–860 (2010).

195. Bowers, J., Zarbakhsh, A., Webster, J. R. P., Hutchings, L. R. & Richards, R. W. Neutron Reflectivity Studies at Liquid−Liquid Interfaces: Methodology and Analysis. *Langmuir* **17**, 140–145 (2001).

196. Kolesnikov, A. I. *et al.* Inelastic and deep inelastic neutron spectroscopy of water molecules under ultra-confinement. *J. Phys.: Conf. Ser.* **1055**, 012002 (2018).

197. Nihonyanagi, S. *et al.* Unified Molecular View of the Air/Water Interface Based on Experimental and Theoretical $\chi(2)$ Spectra of an Isotopically Diluted Water Surface. *J. Am. Chem. Soc.* **133**, 16875–16880 (2011).

198. Yu, C.-C., Seki, T., Wang, Y., Bonn, M. & Nagata, Y. Polarization-Dependent Sum-Frequency Generation Spectroscopy for Angstrom-Scale Depth Profiling of Molecules at Interfaces. *Phys. Rev. Lett.* **128**, 226001 (2022).

199. Liu, S., Li, Q. & Shao, Y. Electrochemistry at micro- and nanoscopic liquid/liquid interfaces. *Chem. Soc. Rev.* **40**, 2236–2253 (2011).

200. Suárez-Herrera, M. F., Gamero-Quijano, A. & Scanlon, M. D. Electrosynthesis of poly(2,5-dimercapto-1,3,4-thiadiazole) films and their composites with gold nanoparticles at a polarised liquid|liquid interface. *Electrochimica Acta* **424**, 140677 (2022).

201. Moshrefi, R., P.   Connors, E., Merschrod, E. & Stockmann, T. J. Simultaneous electropolymerization/Au nanoparticle generation at an electrified liquid/liquid micro-interface. *Electrochimica Acta* **426**, 140749 (2022).

202. Liu, B. & Mirkin, M. V. Electrochemistry at Microscopic Liquid–Liquid Interfaces. *Electroanalysis* **12**, 1433–1446 (2000).

203. Taylor, G. & Girault, H. H. J. Ion transfer reactions across a liquid—liquid interface supported on a micropipette tip. *Journal of Electroanalytical Chemistry and Interfacial Electrochemistry* **208**, 179–183 (1986).

204. Bresme, F., Robotham, O., Chio, W.-I. K., Gonzalez, M. A. & Kornyshev, A. Debye screening, overscreening and specific adsorption in solutions of organic ions. *Phys. Chem. Chem. Phys.* **20**, 27684–27693 (2018).

205. Wang, J. *et al.* Superconcentrated electrolytes for a high-voltage lithium-ion battery. *Nat Commun* **7**, 12032 (2016).

206. Dubouis, N. *et al.* Tuning water reduction through controlled nanoconfinement within an organic liquid matrix. *Nature Catalysis* **3**, 656–663 (2020).

207. Díaz-Duque, Á., Sandoval-Rojas, A. P., Molina-Osorio, A. F., Feliu, J. M. & Suárez-Herrera, M. F. Electrochemical reduction of CO2 in water-acetonitrile mixtures on nanostructured Cu electrode. *Electrochemistry Communications* **61**, 74–77 (2015).

208. Figueiredo, M. C., Ledezma-Yanez, I. & Koper, M. T. M. In Situ Spectroscopic Study of CO2 Electroreduction at Copper Electrodes in Acetonitrile. *ACS Catal.* **6**, 2382–2392 (2016).

209. Chu, A. T., Jung, O., Toh, W. L. & Surendranath, Y. Organic Non-Nucleophilic Electrolyte Resists Carbonation during Selective CO2 Electroreduction. *J. Am. Chem. Soc.* **145**, 9617–9623 (2023).

210. Dorchies, F. *et al.* Controlling the Hydrophilicity of the Electrochemical Interface to Modulate the Oxygen-Atom Transfer in Electrocatalytic Epoxidation Reactions. *J. Am. Chem. Soc.* **144**, 22734–22746 (2022).

211. Dorchies, F. & Grimaud, A. Fine tuning of electrosynthesis pathways by modulation of the electrolyte solvation structure. *Chemical Science* **14**, 7103–7113 (2023).

212. Gamero-Quijano, A., Herzog, G., Peljo, P. & Scanlon, M. D. Electrocatalysis at the polarised interface between two immiscible electrolyte solutions. *Current Opinion in Electrochemistry* **38**, 101212 (2023).

213. Weppner, W., Li-chuan, C. & Piekarczyk, W. Electrochemical Determination of Phase Diagrams and Thermodynamic Data of Multi-Component Systems. *Zeitschrift für Naturforschung A* **35**, 381–388 (1980).

214. Huggins, R. A. The relation between the Gibbs phase rule and reference electrodes. *Ionics* **4**, 129–140 (1998).

215. Plateforme Salomé, Version 9.9.0, June 2022 (https://www.salome-platform.org/).

Résumé

Étude de l'électrochimie des solutions aqueuses fortement concentrées formant des systèmes biphasiques

L'un des principaux objectifs du XXIème siècle est de s'éloigner des combustibles fossiles pour favoriser les énergies renouvelables. Dans ce contexte, les batteries sont et seront clé pour le stockage de l'électricité renouvelable, à condition que la technologie soit sûre et qu'un faible coût soit atteint, encourageant ainsi les batteries aqueuses. Dans cette thèse, l'électrochimie de solutions aqueuses fortement concentrées est étudiée, en mettant l'accent sur les systèmes biphasiques aqueux (SBA) sel-sel. Ces systèmes se caractérisent par deux phases immiscibles composées d'un seul solvant (l'eau) pour lesquelles la séparation de phase est induite par la présence de deux sels fortement concentrés, tels que LiTFSI et LiCl. L'intérêt de ces systèmes réside dans leur capacité à permettre différentes réactions électrochimiques dans chaque phase liquide, offrant de nouvelles opportunités pour les batteries d'intercalation double-ion ou flux redox sans membrane. Dans ce contexte, nous avons étudié le système LiTFSI-LiCl-eau et mis en avant un mécanisme d'intercalation en oxydation des halogénures dans le graphite via deux étapes successives, impliquant un équilibre avec les trihalogénures en solution. De plus, il a été constaté que le SBA empêche l'auto-décharge en inhibant la traversée des ions trihalogénures jusqu'à l'électrode négative, ce qui se traduit par de meilleures efficacités. Nous avons ensuite étudié les SBA d'un point de vue fondamental. Ainsi, l'imagerie Raman a révélé que l'interface liquide-liquide des SBA a une épaisseur de plusieurs micromètres, ce qui diffère considérablement des interfaces eau-huile connues pour être nanométriques. Enfin, une cellule pour effectuer des expériences d'électrochimie à l'interface liquide-liquide a été conçue et utilisée pour obtenir des résultats préliminaires sur le transfert d'ions à l'interface SBA. Ce travail ouvre donc la voie à l'étude de différents types de SBA en utilisant l'imagerie Raman et l'électrochimie, ainsi qu'à une utilisation plus étendue des SBA dans les dispositifs électrochimiques.

Mots clés: Electrochimie, Systèmes Biphasiques Aqueux, Interfaces Liquide-Liquide, électrolytes aqueux

Abstract

Understanding the electrochemistry of highly concentrated aqueous solutions forming biphasic systems

One of the biggest objectives of the 21st century is to move away from fossil fuels and favor renewable resources. In this context, batteries are envisioned to be central for the storage of renewable electricity if intrinsic safety and low cost can be achieved, thus encouraging the development of aqueous batteries. In this thesis, the electrochemistry of highly concentrated aqueous solutions is studied with a focus on salt-salt aqueous biphasic systems (ABS), *i.e.* systems consisting of two coexisting immiscible phases composed of only one solvent (water) with the phase separation driven by two salts at high concentration such as LiTFSI and LiCl. The interest of these systems lies in their capacity to allow different electrochemical reactions in their top and bottom phases, giving new opportunities for dual-ion intercalation batteries and membrane-less redox flow batteries. In this context, using a LiTFSI-LiCl-water ABS as electrolyte, the oxidative intercalation of halides into graphite was shown to follow a two-step mechanism, involving an equilibrium with trihalides in solutions. Importantly, the ABS was found to prevent self-discharge by inhibiting the crossover of trihalides to the negative electrode, thus leading to improved efficiencies. We then investigated the physical/chemical properties of ABS using Raman imaging to reveal that the liquid-liquid interface of ABS is several micrometers thick, drastically different from nanometer-thick water-oil interfaces between two immiscible electrolytes (ITIES). Finally, a dedicated electrochemical cell was designed for performing electrochemistry at liquid-liquid interfaces and use to obtain preliminary results on ion transfer at ABS interfaces. This work paves the way for the studies of ABS using Raman imaging and electrochemistry as well as a wider use of ABS in electrochemical devices.

Keywords: Electrochemistry, Aqueous biphasic systems, Liquid-Liquid interfaces, aqueous electrolytes